

The case for spin-fluctuation induced pairing in $\text{Ba}_{1-x}\text{K}_x\text{Fe}_2\text{As}_2$

Dissertation

Thomas U. Böhm

February 2017

Fakultät für Physik
TECHNISCHE UNIVERSITÄT MÜNCHEN

TECHNISCHE UNIVERSITÄT MÜNCHEN

Fakultät für Physik

Lehrstuhl E23 für Technische Physik

Walther-Meißner-Institut für Tieftemperaturforschung
der Bayerischen Akademie der Wissenschaften

The case for spin-fluctuation induced pairing in $\text{Ba}_{1-x}\text{K}_x\text{Fe}_2\text{As}_2$

Thomas U. Böhm

Vollständiger Abdruck der von der Fakultät für Physik der Technischen
Universität München zur Erlangung des akademischen Grades eines

Doktors der Naturwissenschaften

genehmigten Dissertation.

Vorsitzender: Prof. Dr. Wilhelm Zwerger

Prüfer der Dissertation: 1. Priv. Doz. Dr. Rudolf Hackl
2. Prof. Dr. Alexander Holleitner
3. Prof. Dr. Lara Benfatto

Die Dissertation wurde am 15.02.2017 bei der
Technischen Universität München eingereicht und durch
die Fakultät für Physik am 7.3.2017 angenommen.

Abstract

The microscopic mechanism and the experimental identification of unconventional superconductivity is one of the most vexing problems of contemporary condensed matter physics. Raman spectroscopy provides a new avenue for this quest by accessing the hierarchy of superconducting pairing propensities. The doping-dependent study of competing pairing channels in $\text{Ba}_{1-x}\text{K}_x\text{Fe}_2\text{As}_2$ for $0.22 \leq x \leq 0.70$ is one of the main aspects of this thesis. The observations demonstrate the importance of spin fluctuations for Cooper pairing.

Kurzzusammenfassung

Die experimentelle Identifizierung des mikroskopischen Mechanismus, der zu unkonventioneller Supraleitung führt, ist aktuell eines der irritierendsten Probleme im Bereich der Physik der kondensierten Materie. Die Raman-Spektroskopie offenbart eine Hierarchie von Paarungstendenzen im supraleitenden Zustand und ermöglicht so einen neuen Zugang zu diesem Problem. Die Studie der Dotierungsabhängigkeit von konkurrierenden Paarungskanälen in $\text{Ba}_{1-x}\text{K}_x\text{Fe}_2\text{As}_2$ für $0.22 \leq x \leq 0.70$ ist eines der zentralen Themen dieser Arbeit. Die Beobachtungen zeigen die Bedeutung von Spinfluktuationen für die Cooper-Paarung.

Contents

1	Introduction	1
2	The iron-based superconductors	5
2.1	Basic properties	5
2.1.1	Crystal structure	6
2.1.2	Phase diagram - Electron- and hole-doped BaFe_2As_2	7
2.2	Electronic system	8
2.2.1	Multi-orbital structure in the FeAs layer	8
2.2.2	Fermi surface	10
2.2.3	Interactions	13
2.3	Instabilities and their precursors	15
2.3.1	Spin-density-wave phase	15
2.3.2	Nematic phase	17
2.3.3	Fluctuations in the normal state	18
2.3.4	Superconducting state	19
3	Experiment	23
3.1	Samples	23
3.1.1	$\text{Ba}_{1-x}\text{K}_x\text{Fe}_2\text{As}_2$	24
3.1.2	$\text{Ba}(\text{Fe}_{1-y}\text{Co}_y)_2\text{As}_2$	27
3.2	Raman spectroscopy	28
3.3	Experimental setup	29
4	Theory	31
4.1	Basic principles of electronic Raman scattering	31
4.1.1	Fermi's golden rule	32
4.1.2	Raman susceptibility	33
4.1.3	Selection rules	34
4.2	Raman response in the presence of interactions	35
4.2.1	Coupling between electrons and fluctuations in the normal state	35
4.2.2	Interactions in a multi-band superconductor	37
4.3	Bardasis-Schrieffer mode	40

4.4	Competing interactions embedded in a 5-band model	42
4.4.1	Rigid band model	43
4.4.2	Gap structure and subdominant interactions	45
5	Results and Discussion	47
5.1	Experimental evidence for competing pairing interactions in optimally doped $\text{Ba}_{0.6}\text{K}_{0.4}\text{Fe}_2\text{As}_2$	48
5.1.1	Symmetry analysis	48
5.1.2	Temperature dependence	51
5.1.3	Phenomenological model	53
5.1.4	Discussion	61
5.2	Doping dependence of competing interactions in $\text{Ba}_{1-x}\text{K}_x\text{Fe}_2\text{As}_2$ ($0.22 \leq x \leq 0.70$)	64
5.2.1	Doping dependence of the superconducting features	64
5.2.2	Effects of Fermi surface reconstruction in the SDW phase	68
5.2.3	Evolution of competing pairing interactions close to optimal doping	73
5.2.4	Development of the gap structure at high doping levels	84
5.3	Fluctuations in $\text{Ba}(\text{Fe}_{1-y}\text{Co}_y)_2\text{As}_2$ and $\text{Ba}_{0.78}\text{K}_{0.22}\text{Fe}_2\text{As}_2$	89
5.3.1	Experimental results and analysis	90
5.3.2	Evidence for spin fluctuations	97
5.3.3	Discussion	100
5.4	Phonon anomaly in the vicinity of a quantum critical point	107
6	Summary	111
7	Appendix	113
7.1	Selection rules in the case of spin fluctuations	113
7.2	Resonances in $\text{Ba}_{0.6}\text{K}_{0.4}\text{Fe}_2\text{As}_2$	114
7.3	Symmetry analysis in $\text{Ba}_{1-x}\text{K}_x\text{Fe}_2\text{As}_2$ ($0.35 \leq x \leq 0.70$)	115
7.4	Relative strength of competing interactions	117
7.5	Determination of T_{SDW} in $\text{Ba}(\text{Fe}_{0.949}\text{Co}_{0.051})_2\text{As}_2$	118
7.6	Relaxation rates	120
7.7	Analysis of the phonon anomaly	122
	Bibliography	123
	List of Publications	143
	Acknowledgement	145

Chapter 1

Introduction

“The only reason why we cannot do this problem of superconductivity is that we haven’t got enough imagination.”

R. P. Feynman, 1957 [1]

Superconductivity is known for more than a century, since 1911, when Heike Kamerlingh Onnes discovered the disappearance of resistivity in Hg below a critical temperature $T_c = 4.2$ K [2]. Since then central fundamental questions have been solved [3–15].

A major step towards a microscopic understanding of superconductivity was the development of the BCS theory, as advanced by John Bardeen, Leon N. Cooper and John R. Schrieffer in 1957 [4]. The BCS theory is based on an effective attractive potential between electrons, which is responsible for the formation of pairs of electrons, the Cooper pairs [16]. The Cooper pairs constitute a coherent ground state, which breaks gauge symmetry and is described by the macroscopic wave function $\Psi(\mathbf{r}, t) = \Psi_0(\mathbf{r}, t)e^{i\varphi(\mathbf{r}, t)}$ with both the amplitude Ψ_0 and the phase φ depending on space \mathbf{r} and time t . In the superconducting state an energy gap Δ opens up which also quantifies the energy that is required to break a Cooper pair by 2Δ .

Yet the nature of the underlying attractive interaction is not specified by the BCS theory. Earlier proposals already assumed that lattice vibrations (phonons) may mediate the attraction between electrons [17]. And indeed, the discovery of the isotope effect [18, 19] verified this assumption for the materials hitherto known. Phonon-driven superconductivity is present in many metals [20] like Pb ($T_c = 7.2$ K) [21] or compounds like MgB₂ ($T_c = 39$ K) [22]. There are even indications for a phonon-based mechanism in H₃S with a record T_c of 203 K at 155 GPa [23].

In 1986 however, a revolutionary discovery reinitiated the search for the pairing mechanism. Johannes G. Bednorz and Karl A. Müller found superconductivity in CuO-based compounds, the cuprates [12]. With a maximum T_c of 135 K the cuprates still hold the record at ambient pressure [24]. The undoped parent compounds are magnetically ordered [25–27] Mott insulators and turn into a superconductor upon doping [28]. Another peculiarity of the cuprates is the sign change of the order parameter, exhibiting a $d_{x^2-y^2}$ symmetry in momentum space on a tetragonal lattice thus breaking a second symmetry beyond gauge symmetry [29, 30]. This discovery triggered a renaissance of the research into superconductivity beyond the limits of phonon-driven pairing mechanisms. However, the pairing mechanism is still not pinned down experimentally.

A more recent discovery opened up a new perspective of this problem. One decade ago, Kamihara and coworkers discovered superconductivity in LaOFeP below a transition temperature $T_c \approx 4$ K [31, 32] thus heralding the “iron-age” of superconductivity. Since then a plethora of new iron-based superconductors (IBSs) was discovered with transition temperatures reaching up to 55 K [33–36] for bulk materials and even exceeding 100 K for FeSe monolayers on a SrTiO₃ substrate [37–40]. The IBSs opened also new vistas on the pairing mechanism after 30 years of research into the cuprates. Inspired by this possibility, one of the main questions of this thesis addresses the pairing mechanism in IBSs.

One way to investigate the interactions relevant for superconductivity is based on the study of the symmetry of the superconducting ground state. For instance in the cuprates the interaction is believed to have repulsive components entailing a sign change of the gap. In turn, if the gap is strongly momentum dependent and of lower symmetry than the underlying lattice the usual electron-phonon interaction can be excluded as a pairing mechanism [41]. The anisotropic pairing interaction $V_{\mathbf{k},\mathbf{k}'}$ opens another entrance to the pairing mechanism through collective excitations of the phase φ of the order parameter [42]. For an entirely isotropic potential phase fluctuations require no energy. As soon as the potential becomes anisotropic both phase and amplitude fluctuations require energy. The signature of phase fluctuations are modes inside the gap having an energy below the gap edge similarly as excitons in semiconductors. In a superconductor the energy difference between the gap edge and the collective in-gap mode encodes the residual pairing strength in channels orthogonal to the ground state, $V_{\mathbf{k},\mathbf{k}'} = \Phi_0 V_0 + \Phi_1 V_1 + \dots$ with orthonormal functions Φ_μ and coefficients V_μ . Phase fluctuations with finite energy in superconductors were predicted by Bardasis and Schrieffer (BS) as early as in 1961 [43] and

consecutively applied to rotons in ^4He [44], the A15 compounds [45], and the IBSs [46]. Evidence for the existence of BS modes in IBSs was reported recently [47]. The strength of the residual interaction was found to be as strong as 50% of the ground state interaction. This is supported by theoretical work [48–51] proposing the existence of several competing interactions of similar strength, as caused by the extraordinary Fermi surface of the IBSs.

In the presence of competing pairing interactions in a singlet superconductor, electronic Raman scattering is an exceptional tool [45, 46]. Raman scattering probes not only the energy of a certain excitation with high precision but also its symmetry. Yet a caveat of several scattering experiments is that only the magnitude of the gap $|\Delta|$ can be accessed whereas sign changes remain elusive [30, 52–54]. This is the case for Raman scattering as well [55]. However, in the special case of subleading pairing interactions, electronic Raman scattering is sign/phase sensitive [46]. This means, that the symmetry of collective modes can be unambiguously determined which facilitates conclusions about the symmetry and nature of the corresponding pairing interactions. Obviously Raman scattering probes the magnitude of the energy gap of the superconducting ground state together with symmetry-resolved collective modes reflecting the hierarchy of competing pairing interactions.

Once the hierarchy of pairing states is pinned down the fundamental question arises as to the origin of the pairing interaction [56, 57]. Given the proximity of superconductivity and magnetic ordering in the IBSs the related fluctuations indicate a high susceptibility to perturbations and possible avenues towards pairing [41]. Particularly in the spin channel this possibility was considered from the beginning [58]. The existence of a superconducting dome displaying a maximal T_c close to the end of the phase boundary of the spin-density-wave (SDW) phase is an indication of intertwined superconductivity and magnetic ordering and a nearby quantum critical point (QCP) [59]. This context calls for an experiment which is sensitive to interactions beyond the leading one.

Electronic Raman scattering is utilized in this thesis for the investigation of the superconducting state beyond the leading interaction, and critical fluctuations above the SDW phase. The thesis is structured in the following way: The phase diagram of the studied compounds is introduced in Chapter 2. The electronic structure, basic interactions and instabilities are discussed. In Chapter 3 the studied samples are characterized and the experimental Raman scattering setup is presented. This is followed by a theoretical introduction to Raman scattering in Chapter 4 concentrating on the effects that appear in the combined theoretical and experimental

Chapter 5. Section 5.1 covers the analysis of collective modes. Previous work on collective modes [47] is extended by further experimental and theoretical analysis. This analysis is extended to various doping levels in Section 5.2. A comparison to theoretical calculations was utilized to find the relevant pairing interactions in the present system. In Section 5.3 the fluctuations above the SDW state are discussed and Section 5.4 refers to a phonon anomaly at optimal doping.

Chapter 2

The iron-based superconductors

Since 2006, various superconducting compounds based on the transition metal Fe were discovered [31, 32]. Similar to the cuprates, the IBSs are layered structures. These layers are formed by Fe and an element of either the pnictogen or chalcogen group. Hence two classes of IBSs are defined, the iron pnictides and iron chalcogenides. Like the cuprates the family of the IBSs has common properties which are discussed in the following part.

2.1 Basic properties

The undoped compounds of the IBSs are metallic. Their resistivity in the range of $\rho \approx 10^{-5}$ Ohm m [60] is similar to that of graphite and exhibits a metal-like increase with temperature [61]. The plasma frequency of 1.6 eV [62] of BaFe₂As₂ (BFA) is comparable to that of many metals, e.g. 4.1 eV for Fe or 7.4 eV for Cu [63]. In contrast, undoped cuprates are Mott insulators and need to be doped to turn into a metal.

As for the cuprates, the most extensively studied property of the pnictides and chalcogenides is their superconductivity. The highest superconducting transition temperatures in IBSs exceed 50 K, for instance in SmO_{0.9}F_{0.1}FeAs with $T_c = 55$ K [35]. Experiments with monolayer FeSe on a SrTiO₃ substrate revealed even higher critical temperatures ($T_c = 109$ K) beyond the boiling point of liquid nitrogen [39]. In contrast, conventional superconductors at ambient pressure such as MgB₂ reach a maximum $T_c = 39$ K [22]. According to many conventional superconductors, the Cooper pairing in the pnictides and the resulting formation of the superconducting ground state could be driven by lattice vibrations (phonons). However, the higher transition temperatures in IBSs and qualitative similarities to the phase diagram of

the cuprates led to the assumption that more exotic pairing mechanisms may play a role [56] which will be elucidated in the course of this thesis.

The main focus of this thesis is placed on the pnictide BaFe_2As_2 which exhibits various phases as a function of doping. Hence, we first introduce the crystal structure of BaFe_2As_2 and then explore the doping-dependent phase diagram, as shown in Fig. 2.1(a) and (b), respectively.

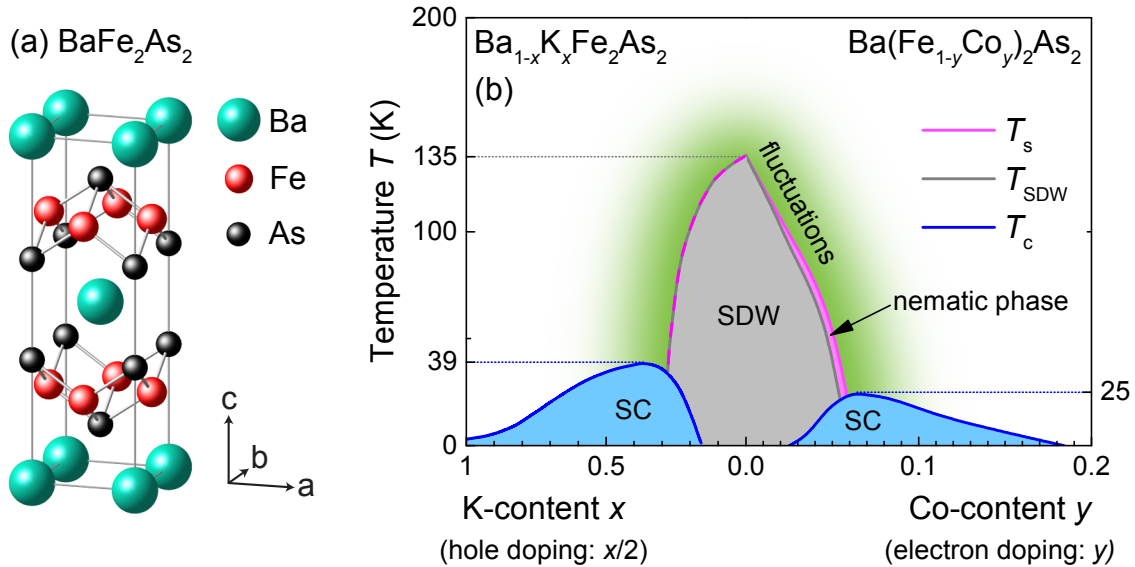


Figure 2.1: Crystal structure and phase diagram. (a) Crystal structure of BaFe_2As_2 [34]. Thin grey lines indicate the edges of the unit cell. Grey connecting lines between Fe and As illustrate covalent Fe-As bonds [64]. (b) The phase diagram shows the doping-dependent phase transitions as adopted from Refs. [60] (for Co-doping) and [65] (for K-doping). The dashed pink and grey line indicates a simultaneous structural transition at T_s and SDW transition at T_{SDW} [66]. The green shaded area indicates the existence of fluctuations next to the SDW transition. Note that the scaling in x (hole doping) and y (electron doping) direction differ.

2.1.1 Crystal structure

Fig. 2.1 shows a tetragonal crystal with lattice constants $a = b = 3.96 \text{ \AA}$ and $c = 13.02 \text{ \AA}$ at room temperature, above any of the indicated phase transitions [34]. The symmetry of the crystal is described by the space group $I4/mmm$.

A covalent bond is formed between Fe and As, causing the tetrahedral structure in the FeAs layers to develop. Among each other the Fe atoms exhibit metallic bonds. The Ba atoms ($[\text{Xe}]6s^2$) acquire the positive charge of Ba^{2+} and thus the bonds to the FeAs^- planes [64] are ionic.

In summary, the electronic properties are by and large determined by the FeAs planes [64]. The metallic Fe-Fe bonds supply free electrons according to the electron configuration of Fe = [Ar]3d⁶4s². Six electrons in the 3d orbitals are available per Fe atom.

Though the mother compound is already metallic it does not exhibit superconductivity. The superconducting phase can be obtained by both hole and electron doping [60, 65]. Hole doping is achieved by substituting Ba²⁺ by K⁺ in Ba_{1-x}K_xFe₂As₂ (BKFA), resulting in one hole per two Fe atoms and a doping of $x/2$. The number of 3d electrons per Fe is then reduced to $6 - x/2$. Electron doping is realized by replacing Fe by Co in Ba(Fe_{1-y}Co_y)₂As₂ (BFCA). Here the number of 3d electrons is increased to $6 + y$. For Co-doping however, a theoretical study claims that the extra electrons stay localized at the Co-sites. Hence they do not supply electrons to the FeAs-layers and act just as random scatterers, which is considered the main reason for the dependence of the phases on Co substitution [67]. In the following, the doping picture is used yielding the doping concentration z to be $-x/2$ for hole and y for electron doping, respectively.

2.1.2 Phase diagram - Electron- and hole-doped BaFe₂As₂

Doping BFA with K or Co yields the phase diagram of Fig. 2.1(b). The mother compound BaFe₂As₂ is undoped with $z = 0$. Here a SDW phase is formed below $T_{\text{SDW}}(z = 0) = 135$ K [68]. At the same temperature a structural distortion takes place, indicated by T_s . Below T_s the two perpendicular Fe-Fe distances develop a difference of 0.7% [69], i.e. the Fe structure changes from tetragonal to orthorhombic. Consequently, any cut of the unit cell in the ab -plane changes from a square into a rhombus.

With increasing hole doping T_{SDW} continuously decreases until it vanishes at $x \approx 0.28$ [70]. Both transitions coincide for the entire hole-doped range [66]. In contrast, on the electron-doped side the transitions split, with T_s exceeding T_{SDW} by a few Kelvin. The difference $T_s - T_{\text{SDW}}$ continuously increases with higher electron doping up to approximately 15 K at $y \approx 0.06$ [60]. In the temperature range confined by $T_{\text{SDW}} < T < T_s$ the so called nematic phase is present.

Close to the SDW and nematic phase a region (green) is indicated where fluctuations are present [71–74]. The characterization of this region will be one of the main questions to be addressed in this thesis.

Another central aspect of this work is the investigation of the superconducting state in the hole-doped compound. Superconductivity emerges above $x \approx 0.16$, reaches

its maximum at optimal doping ($x \approx 0.4$) with $T_c = 39$ K and survives up to $x = 1$ in the compound KFe_2As_2 with $T_c = 3$ K.

All of the phases are closely related to the electronic band structure. Hence, to investigate the phases presented here on a physical basis, the electronic structure will be described in the following parts.

2.2 Electronic system

As mentioned above, the electronic system is predominantly determined by the Fe $3d$ orbitals. Various experimental and theoretical studies have been performed to obtain the band structure of the IBSs. Though the basic electronic structure is well established, there is still no consensus about some parts of the Fermi surface [75, 76]. Hence the analysis is based on the most widely used electronic structure found in the current literature.

2.2.1 Multi-orbital structure in the FeAs layer

To illustrate the multi-orbital structure, the FeAs layer is shown in Fig. 2.2 along with five Fe $3d$ orbitals as located at each Fe atom. In the undoped compound, six electrons populate these orbitals. The mobility of the electrons is formally described

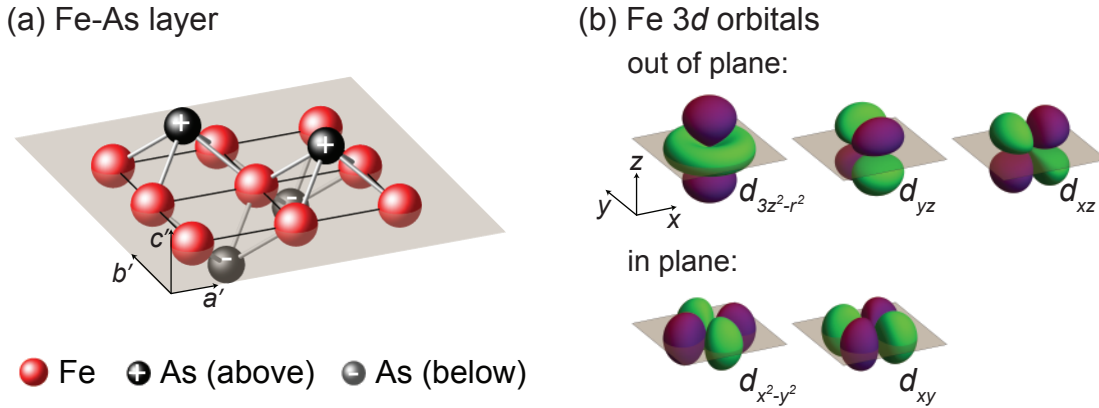


Figure 2.2: Fe $3d$ orbitals embedded in the FeAs layer. (a) The FeAs layer is shown with As atoms located alternately above and below the Fe plane (grey plane). (b) The Fe $3d$ orbitals oriented according to the FeAs plane of (a) are depicted.

by finite hopping amplitudes between orbitals of neighboring Fe sites [48, 77]. In the simplest case, the electrons hop inside the Fe plane, unaffected by the As atoms.

Hence the 1 Fe unit cell as shown in Fig. 2.3(a) sufficiently describes the electronic system. The corresponding Brillouin zone (BZ) is the 1 Fe BZ as displayed in Fig.

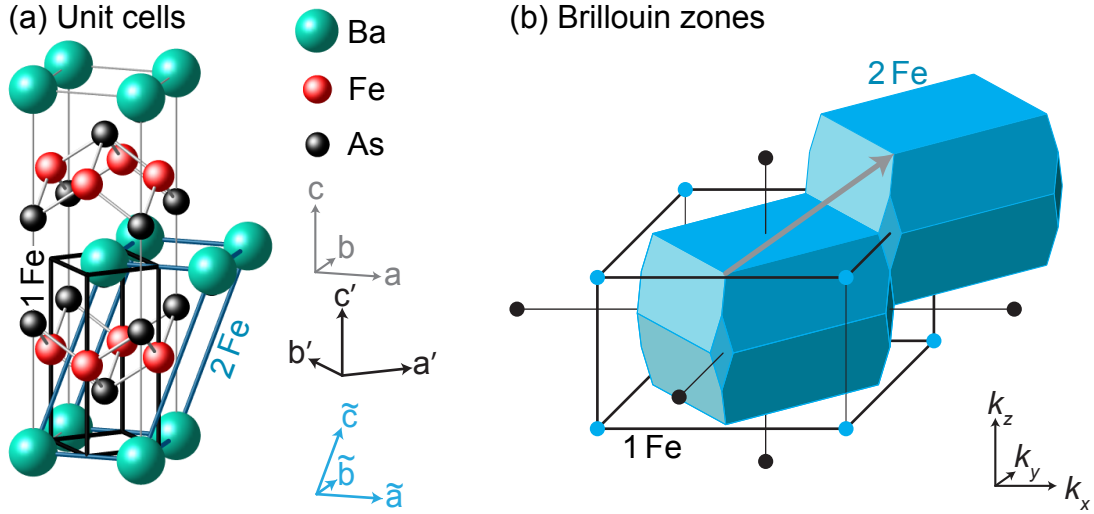


Figure 2.3: Unit cells and corresponding Brillouin zones. (a) The crystal structure of Fig. 2.1(a) is repeated. The grey axes indicate the large tetragonal unit cell introduced in this figure with the axes a , b , and c . The 1 Fe unit cell (black) is described by the axes a' , b' and c' . (b) The Brillouin zone corresponding to the 1 Fe unit cell is shown as a black frame. Black dots indicate the reciprocal lattice points. The momenta in k_x , k_y and k_z direction are parallel to a' , b' and c' , respectively. However, for illustrative purpose the coordinate system in momentum space is manually rotated by 45° around k_z with respect to the (a', b', c') system in real space. The 2 Fe unit cell (blue) is described by the coordinate system defined by $\tilde{a} = a$, $\tilde{b} = b$, and \tilde{c} . The transform into reciprocal space adds the blue reciprocal lattice points at the corners of the 1 Fe BZ. The solid blue 2 Fe BZ is constructed out of these vectors. An adjacent 2 Fe BZ is displayed, illustrating the additional translational symmetry by the grey vector.

2.3(b). The tetragonal 1 Fe cell transforms into a tetragonal BZ. The corresponding spanning vectors are a' , b' and c' for the unit cell and k_x , k_y , and k_z for the BZ, defined by the Wigner-Seitz cell of the reciprocal lattice.

The 1 Fe cell accounts for the major features of the electronic system. However, if hopping via the As atoms plays a role, the As superstructure must be taken into account, i.e. the adequate unit cell must be chosen. In this case a monoclinic cell, namely the 2 Fe unit cell describes not only the As superstructure but is the smallest unit cell adequate to describe the entire crystal. With respect to the 1 Fe unit cell, this cell transforms to a BZ as indicated, reduced in volume to $1/2$. The zones are staggered in a way that an additional translational symmetry is introduced along the vector $(\pi/a', \pi/b', \pi/c')$. Note that the normalization with the lattice constants is sometimes omitted and the vector is simply written as (π, π, π) .

2.2.2 Fermi surface

To construct the Fermi surface (FS) we start on the basis of the 1 Fe unit cell and BZ. From a theoretical point of view, a tight binding model describes the electronic system adequately, with the corresponding Hamiltonian [48]

$$\mathcal{H}_0 = \sum_{\mathbf{k}} \sum_{m,n=1}^5 (\xi_{mn}(\mathbf{k}) + \epsilon_m(\mathbf{k})\delta_{m,n})d_m^\dagger(\mathbf{k})d_n(\mathbf{k}) \quad (2.1)$$

in orbital basis, where $d_m^\dagger(\mathbf{k})$ and $d_m(\mathbf{k})$ generate and, respectively annihilate an electron of momentum \mathbf{k} in orbital $m \in \{d_{3z^2-r^2}, d_{xy}, d_{xz}, d_{yz}, d_{x^2-y^2}\}$. ξ_{mn} is the kinetic energy term describing the hopping parameters from orbital m to n and ϵ_m is the onsite energy of orbital m . Solving the eigenvalue problem yields the band structure in momentum space. The eigenvalues define the energy $E_i(\mathbf{k})$ of band i . The resulting band structure is schematically drawn in Fig. 2.4(a). As the band structure is invariant under rotation by 90° around k_z , the equality $E(k_x) = E(k_y)$ holds. Two bands (red), opened downwards, are centered at the Γ point. These bands are unoccupied as long as $E_i(\mathbf{k}) > E_F$, i.e. in a region close to the Γ point and filled with electrons outside of that region. This region can equally be considered as occupied by holes. Hence the bands opened downwards are called hole bands (red). The bands which are opened upwards, like those centered at the X and Y points, are accordingly called electron bands (blue).

The intersections of the bands with E_F yield the FS structure in the $k_x - k_y$ -plane (1 Fe BZ) as shown in Fig. 2.4(b). The bands form nearly circular hole pockets around Γ and elliptical electron pockets encircling the X and Y points. The pockets around M emerge (cross the Fermi energy) at small hole doping [78].

The transformation of the Hamiltonian not only yields the band structure but also defines the orbital composition at each \mathbf{k} point for each band, as encoded in the eigenvectors. The components of these eigenvectors $a_{m,i}(\mathbf{k})$ are called orbital characters with $|a_{m,i}(\mathbf{k})|^2$ giving the probability of an electron of band i at \mathbf{k} to be in orbital m . Fig. 2.4(c) shows the dominant orbital characters at the FS [78]. The hole pockets centered at Γ predominantly originate from d_{xz} and d_{yz} orbitals, the electron pockets from d_{xz} , d_{yz} , and d_{xy} , and the hole pockets at M from d_{xy} orbitals. The theoretical approach was used to give an introduction to the band structure based on a physical model. In the following the experimental results are discussed. In the experiment the 2 Fe BZ is useful to capture also the influence of the As superstructure. This means, that the electron pockets of Fig. 2.4(b) at X and Y

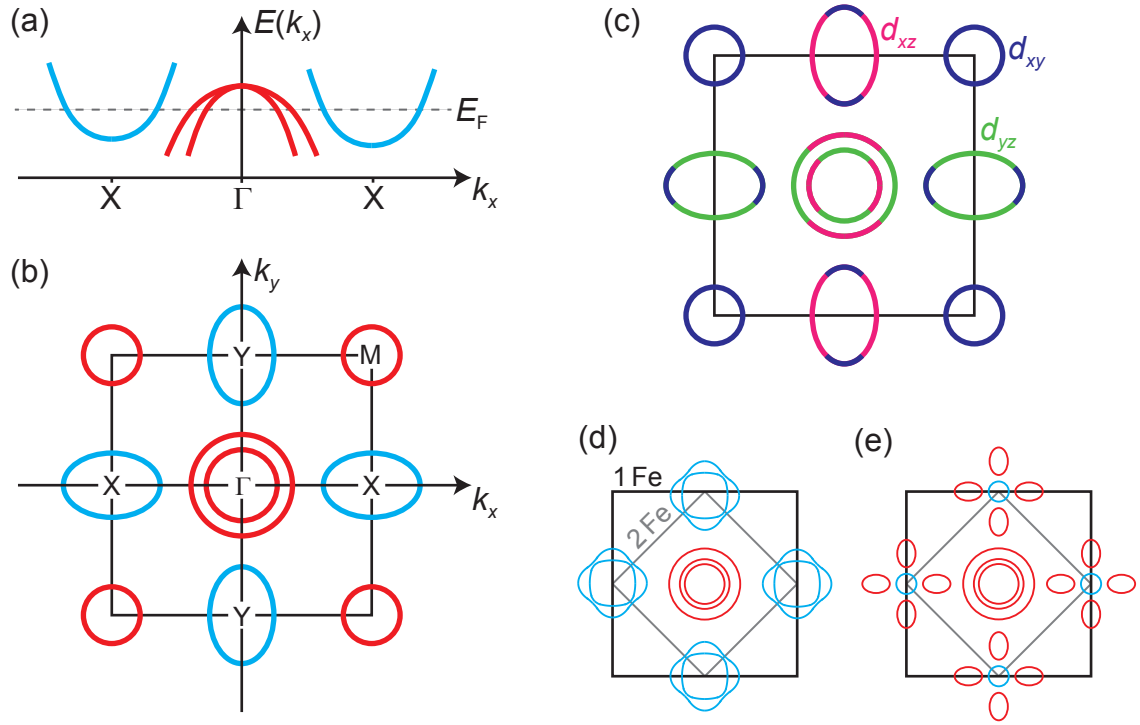


Figure 2.4: Band structure and resulting FS. (a) shows the generic band structure, i.e. the band energy with respect to the momentum k_x . Depending on the sign of the curvature, red and blue bands illustrate hole and electron bands, respectively. (b) presents the Fermi surface as obtained from a cut at the Fermi energy E_F . The band structure along k_x is identical to the structure along k_y due to 90° rotational symmetry. For hole doping, additional pockets at M emerge. (c) shows the dominant orbital character [78]. (d) and (e) display schematically drawn FSs according to ARPES experiments of Refs. [75] and [76], respectively. Here the 2 Fe BZ is relevant. The hole pockets at the M -point are omitted for clarity. They are identical to those at Γ .

are shifted on top of each other due to the additional translational symmetry introduced in Fig. 2.3(b). With the same translation the pocket at M is shifted into the center. The qualitative Fermi surface obtained by angle-resolved photo-emission spectroscopy (ARPES) experiments on optimally hole-doped BKFA was measured by two groups [75, 76, 81, 85], who found different results as shown in Fig. 2.4(d) and (e). Both measurements agree on the nature of the pockets in the center being hole-like and on the existence of electron pockets at X and Y . However, Fig. 2.4(d) shows two elliptical electron pockets on top of each other, whereas (e) exhibits a “propeller”-like structure composed of a small electron pocket and four hole-like lobes around.

A clear discrepancy is observed, which is still not resolved. Most of the related publications however, are based on the structure in Fig. 2.4(d). Hence this structure is

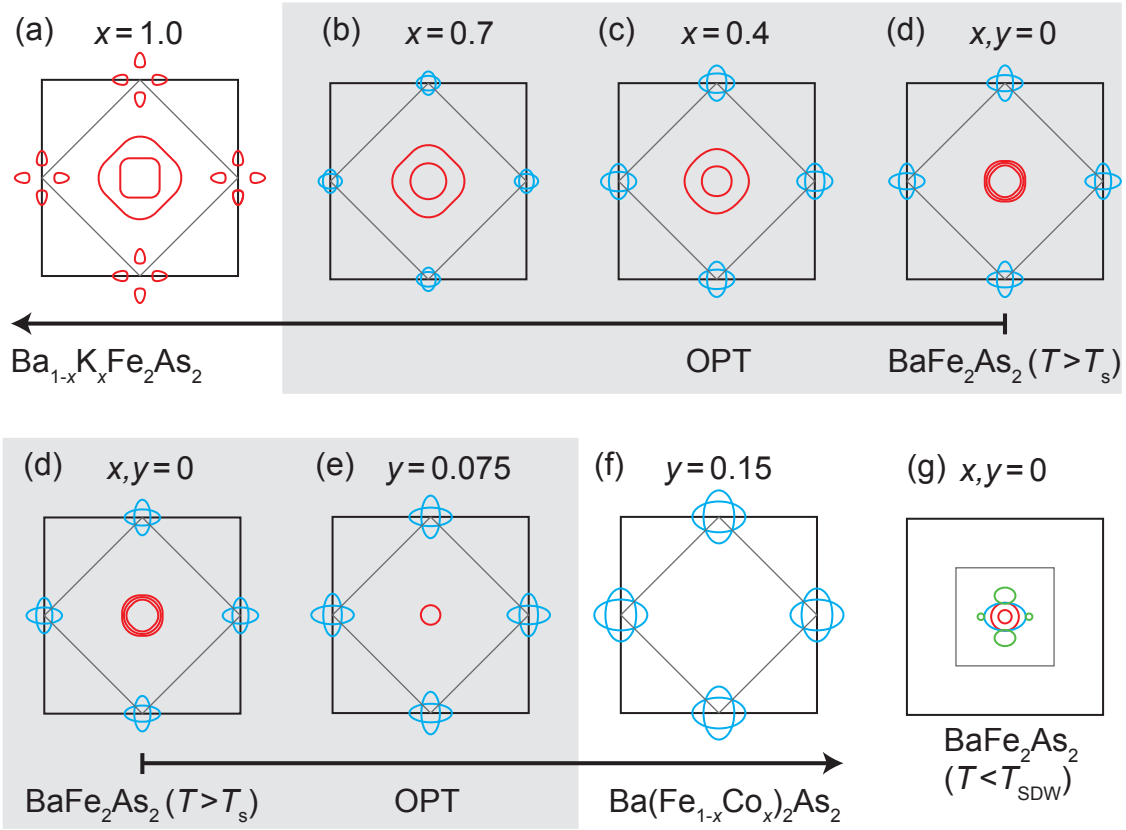


Figure 2.5: Doping dependence of the Fermi surface. (a-f) display the doping dependence of the Fermi surface as obtained from Refs. [79], [80], [81],[82],[83], and [84], respectively. The FS is shown with respect to the 2 Fe BZ. Hole pockets at M are omitted as they repeat the pockets at Γ in the 2 Fe zone. (g) shows the FS in the SDW state with a smaller BZ. The green FS sheets emerge from a folding involving electron and hole pockets.

referred to throughout this thesis.

Accordingly, Fig. 2.5 compiles quantitative ARPES results for various doping levels. Some important properties shall be highlighted: (i) With increasing hole doping, the electron pockets shrink and the hole pockets increase, and vice versa for increasing electron doping. (ii) The FSs from $x = 0.4$ up to $x = 0.7$ are qualitatively similar, i.e. they evolve smoothly with doping. (iii) A qualitatively different FS is obtained in the SDW phase. The reason is another folding into a smaller BZ as imposed by the SDW superstructure [82]. Doping levels from $x = 0$ to $x = 0.7$ and $y = 0$ to $y = 0.085$ are investigated in this thesis, as highlighted by the grey shaded area. Outside of this doping range, qualitative changes are observed. At $x = 1.0$, the electron pockets disappear completely, whereas at $y = 0.15$ the hole pockets have vanished.

2.2.3 Interactions

With the knowledge of the FS, various basic interactions of the system can be discussed. In the weak coupling limit these interactions are responsible for the phase transitions, e.g. causing the SDW state to emerge or providing a pairing interaction for superconductivity. An introduction to three different classes of interactions will be presented: Phonon-driven interactions [17], antiferromagnetic (AFM) exchange

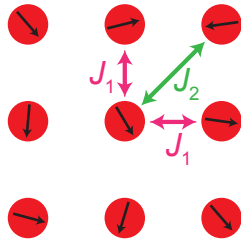


Figure 2.6: Interactions in the $J_1 - J_2$ model. The AFM exchange acts between the spins of neighboring Fe sites (red circles) via the nearest-neighbor interaction J_1 (pink) and the next-nearest-neighbor interaction J_2 (green).

$J_1 - J_2$ model, where J_1 is the nearest neighbor interaction and J_2 the next-nearest neighbor interaction as illustrated in Fig. 2.6. The exchange mechanism can be responsible for superconductivity and for generating a magnetic ground state, in the simplest case ($J_2 = 0$) an AFM state.

The mechanism of exchanging fluctuations between electrons is more complicated as there are several kinds of fluctuations. In any case, a typical set of starting parameters used for this problem is based on Coulomb interaction and contains intra- (U_{intra}) and inter-orbital (U_{inter}) interaction, Hund's rule coupling (J_{Hund}), which favors parallel spin alignment, and the pair-hopping energy (J_{pair}). These parameters enter the interaction Hamiltonian [77, 92–95]

$$\begin{aligned} \mathcal{H}_{\text{int}} = & \sum_i \left[U_{\text{intra}} \sum_a n_{ia\uparrow} n_{ia\downarrow} + U_{\text{inter}} \sum_{a<b,ss'} n_{ias} n_{ibs'} \right. \\ & \left. + J_{\text{Hund}} \sum_{a<b,ss'} c_{ias}^\dagger c_{ibs'}^\dagger c_{ias'} c_{ibs} + J_{\text{pair}} \sum_{a<b} c_{ia\uparrow}^\dagger c_{ia\downarrow}^\dagger c_{ib\downarrow} c_{ib\uparrow} \right] \end{aligned} \quad (2.2)$$

coupling between spins of neighboring Fe atoms [86–89] and the fluctuation-exchange interaction [90].

Phonons can act as exchange bosons mediating an electron-electron interaction. Within the BCS approximation, this interaction is isotropic and attractive, the interaction range is not limited. Hence the interaction can act within a single pocket (intra-band) or in between of two different pockets (inter-band).

The AFM exchange interaction is described by $\mathcal{H}_{\text{AFM}} = J_1 \sum_{l,k} \vec{S}_l \vec{S}_k$ [86], in the simplest case where J_1 acts between spins \vec{S}_l and \vec{S}_k at nearest neighbor Fe sites l and k , i.e. along a' or b' . The interaction J_1 reaches up to about 100 meV as found by neutron scattering experiments [91]. An extension is the

with fermionic creation c_{ias}^\dagger , annihilation c_{ias} , and number $n_{ias} = c_{ias}^\dagger c_{ias}$ operators at site i , in orbital a and with the spin s . Various theoretical techniques use this set and renormalize the parameters in the many-particle system in order to calculate a realistic interaction potential $V_{\mathbf{k},\mathbf{k}'}$ responsible for Cooper pairing. Rather than describing the renormalization process, an introduction to the results is presented here using the “nesting” picture. Nesting is a term that describes how well parts of the FS are mapped onto one another by a specific vector \mathbf{Q} , the nesting vector. This concept is based on the Lindhard susceptibility

$$\chi_L(\mathbf{q}, \omega_m) = \sum_{\mathbf{k}} \frac{f(E(\mathbf{k} + \mathbf{Q})) - f(E(\mathbf{k}))}{i\omega_m + E(\mathbf{k} + \mathbf{Q}) - E(\mathbf{k})} \quad (2.3)$$

with the Fermi distribution $f(E)$ and the bosonic Matsubara frequency ω_m . A good nesting is reflected by a large Lindhard susceptibility, i.e. in the case of $\omega_m = 0$, the denominator diverges for $E(\mathbf{k} + \mathbf{Q}) \rightarrow E(\mathbf{k})$ on an extended part of the FS. With good nesting, a huge enhancement of the fluctuation-exchange coupling can be achieved which will finally cause an ordered state to appear such as a spin- or charge-density wave [48]. In addition, a possible pairing interaction for superconductivity is provided. In the special case of a multi-band superconductor, however, nesting

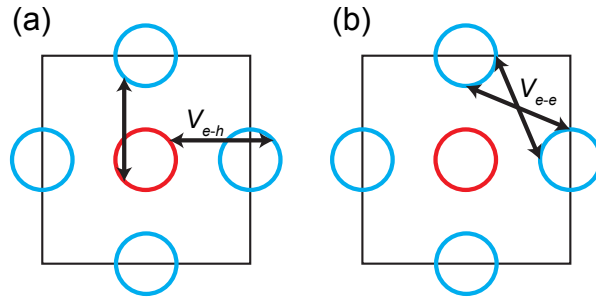


Figure 2.7: Nesting vectors for circular pockets of similar sizes. (a) shows an interaction V_{e-h} between hole and electron pockets. With the nesting vectors $(\pm\pi, 0)$ and $(0, \pm\pi)$, the hole pocket can be perfectly mapped onto the electron pockets. (b) displays crossed nesting vectors between electron pockets with the interaction V_{e-e} .

is not only determined by the shape of the FS but also by the orbital contents. A strong interaction related to nesting can only appear between the same orbitals, i.e. identical orbital characters at \mathbf{k} and \mathbf{k}' must be large [49].

For spin-fluctuation exchange, Fig. 2.7 shows two sets of nesting vectors. One set (a) displays the vectors between hole and electron pockets, the other one (b) those between two neighboring electron pockets. Regarding the FS of this simple model,

a perfect nesting between the electron and hole pockets is achieved for the first set with the nesting vectors $Q \in \{(\pm\pi, 0), (0, \pm\pi)\}$. As spin fluctuations mediate a repulsive interaction, a sign change between the electron and hole bands of the order parameter of the superconducting ground state [58] can be expected according to the BCS gap equation [4]

$$\Delta(\mathbf{k}) = -\frac{1}{2} \sum_{\mathbf{k}'} \frac{V_{\mathbf{k},\mathbf{k}'} \Delta(\mathbf{k}')}{\sqrt{E(\mathbf{k}')^2 + |\Delta(\mathbf{k}')|^2}} \quad (2.4)$$

with the momentum-dependent gap energy $\Delta(\mathbf{k})$. For the case of interactions between electron pockets, an intuitive guess would lead to nesting vectors $\mathbf{Q} \in \{(\pm\pi, \pm\pi), (\pm\pi, \mp\pi)\}$ yielding a perfect mapping of two neighboring electron pockets. However, due to the need of matching orbital characters, the nesting vectors as depicted in Fig. 2.7(b) are preferred [49]. Here a sign-changing ground state between two neighboring electron pockets is expected.

2.3 Instabilities and their precursors

BFA exhibits three notable phase transitions, all depicted in the phase diagram of Fig. 2.1: A SDW phase, a nematic phase, and superconductivity. Special attention is paid to the superconducting state and the fluctuations appearing above the SDW state. The origin of these phases will be discussed on the basis of the interactions presented above and then analyzed with the help of the experiments performed in this thesis.

2.3.1 Spin-density-wave phase

It is shown by many experiments, that magnetic order is established in a doping range around the mother compound and develops as a SDW [68, 70, 96–98]. In BFA the local magnetic moment at the Fe sites is $0.87\mu_B$ [68]. The spin alignment in a real-space and momentum-space picture is explained in the following [99, 100].

Applied to the pnictides, the SDW state in real space describes the orientation of the spins at the Fe sites. In the FeAs planes, the spins are aligned antiferromagnetically along one Fe-Fe direction and ferromagnetically along the perpendicular direction. This means that the 90° rotational symmetry Z_2 is broken. As the spin degrees of freedom are frozen out in a magnetically ordered system, the spin-rotational $O(3)$ symmetry is broken as well. In Fig. 2.8 two possible SDW states are shown in (c1)

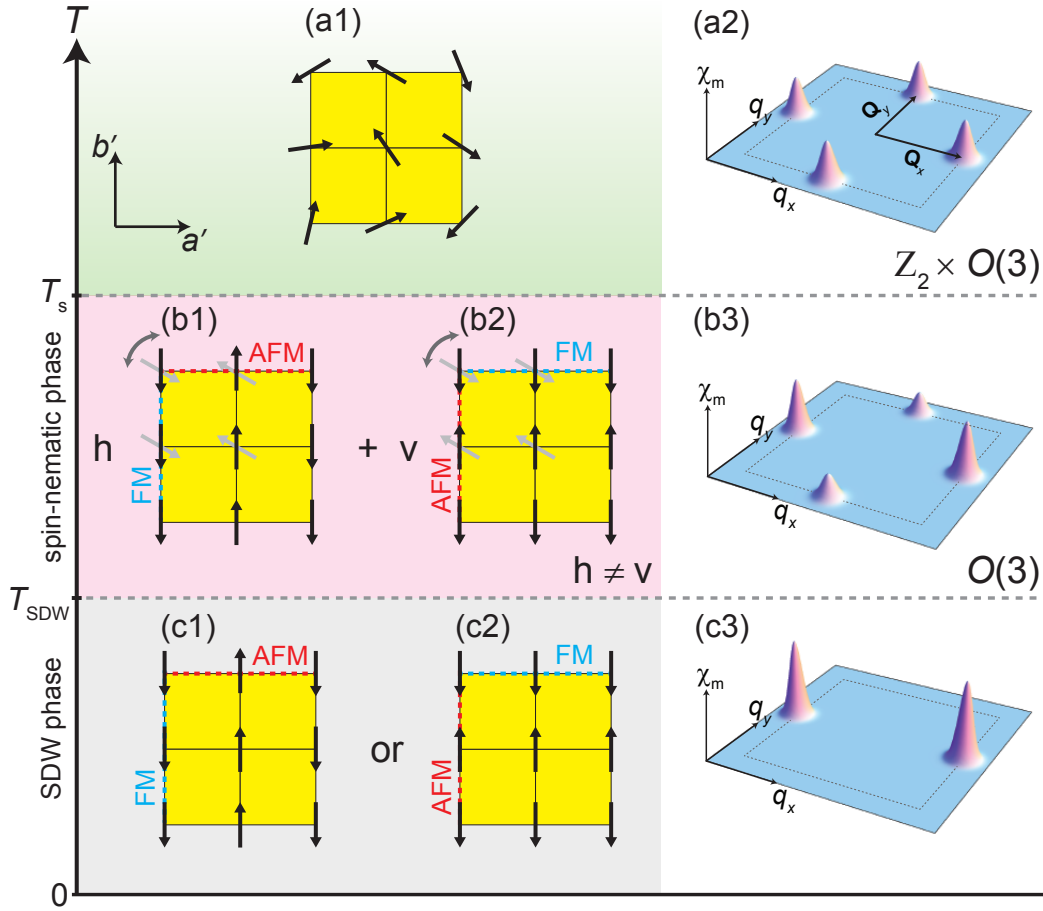


Figure 2.8: Development of the spin configuration with temperature in real and momentum space. Three sections are presented: (a1,a2) The normal state, (b1-b3) the spin-nematic phase between T_s and T_{SDW} , and (c1-c3) the SDW phase below T_{SDW} . Yellow squares depict 1 Fe unit cells with spins (black arrows) on the Fe sites. (a1) The spins are completely disordered in the normal state. (a2) shows the magnetic susceptibility (from Ref. [99]), equally peaked at the wavevectors $Q_x = (\pi/a', 0)$, $Q_y = (0, \pi/b')$, $-Q_x$, and $-Q_y$, where Q_x and Q_y are associated with an antiferromagnetic (AFM) order along a' and b' , respectively. Spin-rotational symmetry $O(3)$ and 90° rotation symmetry Z_2 is preserved. (b1-b3) The nematic state is visualized by a linear combination of two states depicted in (b1) and (b2). In (b1) the AFM direction is oriented along a' , in (b2) along b' . The prefactors h and v define the probabilities of the respective states. The grey double arrow on the upper left indicates spin-rotational symmetry. Another equally probable configuration is indicated by light grey arrows. As $h = v$ in (a1) and $h \neq v$ in the nematic phase, the Z_2 symmetry is broken. Consequently the magnetic susceptibility in (b3) equally shows the broken Z_2 symmetry. In this case, the susceptibility along Q_x is higher than along Q_y , i.e. $h > v$. (c1-c3) In the SDW state, $O(3)$ is broken as well and the system selects either the state of (c1) or the one of (c2). The susceptibility shows the case, where the configuration of (c1) is favored, the one of (c2) doesn't exist. Hence the magnetic response from the configuration of (c2) at Q_y has completely vanished.

and (c2). The (ideal) system chooses one of them, which extends throughout the whole crystal.

In momentum space, the corresponding wave vector is oriented along the AFM direction. If the wavelength extends over two Fe sites, as illustrated, the magnetic susceptibility exhibits a peak at $\pm Q_x = (\pi/a', 0)$ as shown in Fig. 2.8(c1) or at $\pm Q_y = (0, \pi/b')$ in (c2). The first case is depicted in (c3). As one state is chosen in the whole system, the other one cannot give a (magnetic) response.

The real-space picture implies magnetic moments fixed to the iron sites, i.e. the moments are localized. However, an itinerant (non-localized) state is also possible [101–105]. In any case the picture in momentum space remains valid.

This is highly relevant for the mechanism at the origin of the SDW. Localized magnetization can be achieved by AFM magnetic-exchange interactions, whereas itinerant magnetization is based on a nesting condition, as described above. The Fermi surface of the pnictides is predestined for a nesting by $Q_{x,y}$. The nesting is optimal for the undoped compound and weakens with increasing doping. Hence T_{SDW} decreases. The nesting also causes a SDW gap to open. As the nesting vector defines a superstructure the Fermi surface is folded back by Q and degeneracies appear where the Fermi surfaces intersect each other. Anticrossing lifts the degeneracies and a gap opens up. This gap decreases with increasing doping [106].

2.3.2 Nematic phase

Above T_{SDW} a nematic phase may be found. Signatures of a nematic phase have only been found for the electron-doped BFCFA and are lacking for BKFA. The driving force behind nematicity is currently debated with candidates being charge, orbital and spin interactions.

The spin picture is presented first. In contrast to the SDW state, $O(3)$ symmetry is preserved, whereas Z_2 is still broken [100]. Hence any net magnetization vanishes. The nematic state is a linear combination of the two states shown in Fig. 2.8(b1) and (b2) with different probabilities. These probabilities are quantified by the prefactors h and v attributed to the states with horizontally (along a') and vertically (along b') oriented AFM directions. If the AFM ordering vector point into x direction ($h > v$), the peaks in the susceptibility of (b3) are higher at $\pm Q_x$ than at $\pm Q_y$. The degree of nematic order can thus be defined as $h - v$.

A nematic state based on charge and orbital order is explained in Fig. 2.9, showing an orbital-nematic state. It is again a linear combination of two states with unequal population, defined by h' and v' . However, in contrast to spins there is no $O(3)$

symmetry. In the orbital picture this transforms from a continuous to an Ising-like symmetry, where only two instead of infinite orientations are possible. So even if $h' > v'$ the net orbital order vanishes.

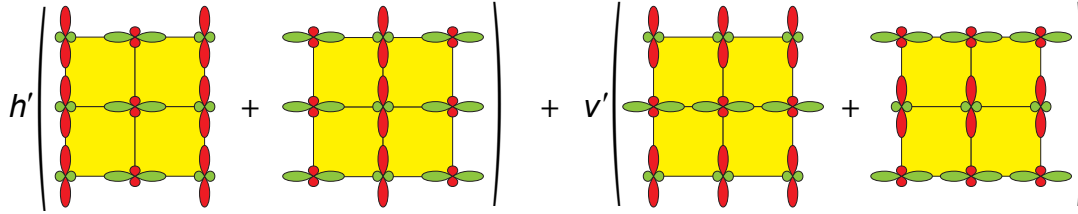


Figure 2.9: Illustration of an orbital-nematic state in analogy to Fig. 2.8. The orbitals d_{xz} and d_{yz} are shown as green and red lobes in the Fe lattice with Fe atoms at the corners of the yellow squares. Extended and shrunk orbitals illustrate orbital order, which breaks 90° rotational symmetry. The sums in the brackets add up to zero net orbital order. States with horizontal and vertical antiferro-orbital directions are associated with the prefactors h' and v' , respectively. The inequality $h' \neq v'$ is the condition for the existence of an orbital-nematic state. In the orbitally ordered state, the system develops long-range order according to one of the four states.

2.3.3 Fluctuations in the normal state

In the state above T_s the spins are completely disordered, see Fig. 2.8 (a1). $O(3)$ and Z_2 is preserved and hence $h = v$. The momentum picture (a2) also shows Z_2 symmetry. In this state, fluctuations emerge below a doping-dependent temperature. Yet it is unclear, as in the nematic phase, whether these fluctuations are of spin, charge or orbital origin.

Fluctuations can be understood as small patches, where the order-parameter is finite. In the case of nematic fluctuations, patches with $h > v$ and $h < v$ are equally present, in total no nematic order is formed. These patches have a typical extension in space of ξ , which is the correlation length and decay after a typical time τ . Both values are small for high temperatures. However, if ξ and τ diverge upon approaching a critical temperature T^* , a long-range ordered state is formed.

The relation to possible experiments probing fluctuations is formulated by the fluctuation-dissipation theorem [107]. A susceptibility is measured, which probes the response of a system to an external field. The external field is generated in a way to drive the system into the ordered state. The susceptibility then describes the tendency of the system to follow this external field. Hence the susceptibility also diverges at T^* . In a more theoretical view, the fluctuations are defined by a

correlation function which is proportional to the imaginary part of the related susceptibility.

In terms of Feynman diagrams, the fluctuations are illustrated by bosonic propagators. Spin fluctuations can, for example, be described by the Ornstein-Zernike propagator [108]

$$D_{\text{OZ}}(\mathbf{q}, \omega_m) = \frac{1}{|\omega_m| + v|\mathbf{q} - \mathbf{q}_c|^2 + m} \quad (2.5)$$

with the bosonic frequency ω_m , a velocity v , the momentum \mathbf{q} , the critical momentum \mathbf{q}_c , and the temperature-dependent mass $m \propto 1/\xi^2$. According to Fig. 2.8 the critical momenta for spin fluctuations are $(\pm\pi, 0)$ and $(0, \pm\pi)$.

A relation to superconductivity could be based on the existence of a QCP and quantum fluctuation emerging from this QCP. These fluctuations are candidates to mediate Cooper pairing. A superconducting dome develops around the QCP, extending to a doping range where no long-ranged magnetic or nematic order is present anymore.

2.3.4 Superconducting state

Superconductivity and SDW order share a region of coexistence in the phase diagram for both electron and hole doping. The superconducting ground state is discussed in the following for various underlying pairing interactions [109].

The ground state is described by a fermionic wave function having a spin- and a momentum-dependent part. For a singlet superconductor with Cooper pairs of the configuration $(\mathbf{k} \uparrow, -\mathbf{k} \downarrow)$, only even symmetries are allowed for the \mathbf{k} -dependent part due to the antisymmetry of a fermionic wave function. Knight shift measurements provide evidence for singlet pairing in the present systems [110].

Several configurations of the ground state are presented in Fig. 2.10, defined by the momentum dependence of the generally complex energy gap $\Delta(\mathbf{k})$. The simplest one is an isotropic gap on every FS sheet as shown in Fig. 2.10(a), i.e. $\Delta(\mathbf{k}) = \Delta_0$. The gap structure is of zero order s -wave symmetry referred to as s^{++} . An anisotropic gap of the same symmetry is displayed in Fig. 2.10(b), with minimal (Δ_{min}) and maximal (Δ_{max}) gaps as indicated. The second order s -wave symmetry (also called s^\pm) is depicted in Fig. 2.10(c) with a sign-change between electron and hole pockets but otherwise momentum independent. In Fig. 2.10(d) a gap of $d_{x^2-y^2}$ -symmetry is presented with nodes on the hole pockets. Nodes describe the momenta on the FS, where $\Delta(\mathbf{k}) = 0$. Fig. 2.10(e) illustrates a combination of states having the orthogonal symmetries s^\pm and $d_{x^2-y^2}$, which results in an $s + id$ state [111, 112].

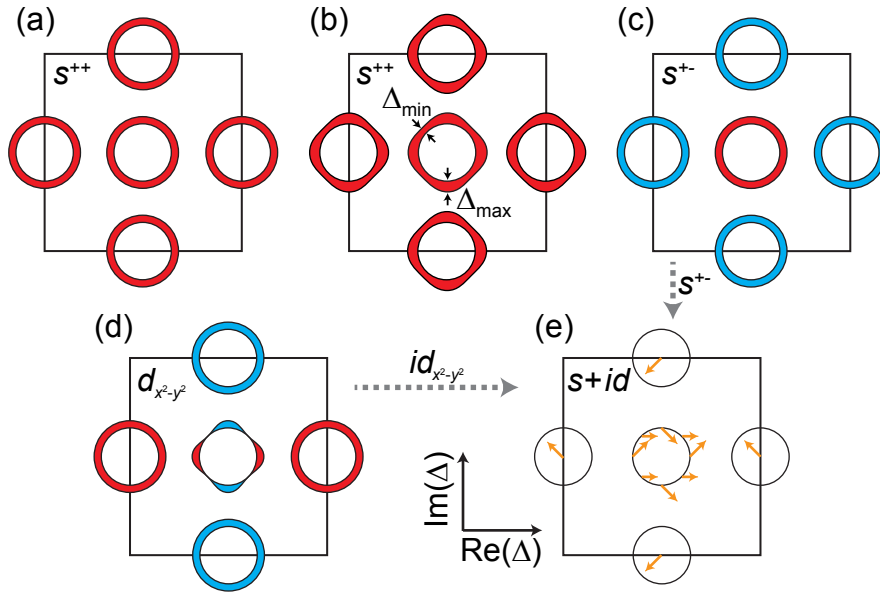


Figure 2.10: A selection of superconducting ground states [109]. The gap $\Delta(\mathbf{k})$ is illustrated by red (positive gap) and blue (negative gap) belts, surrounding the Fermi surface sheets. The thickness of the belts indicates the momentum-dependent magnitude. (a) and (b) show s^{++} states with no sign change. (c) depicts the sign-changing s^{\pm} state. (d) displays the $d_{x^2-y^2}$ -symmetric gap with nodes ($\Delta = 0$) at the hole pocket. (e) illustrates the combined state $s^{\pm} + id_{x^2-y^2}$. Orange arrows are vectors in the complex plane as defined by the coordinate system on the left hand side of (e) with $\text{Re}[\Delta(\mathbf{k})] = \Delta_s(\mathbf{k})$ and $\text{Im}[\Delta(\mathbf{k})] = \Delta_d(\mathbf{k})$. The single arrow in the center of each electron pocket is valid for the whole pocket. In contrast to the state in (d), the magnitude $|\Delta|$ never vanishes.

If such a state is formed, the system can gain energy from both s - and d -wave symmetric pairing interactions. The squared magnitude $|\Delta_s + i\Delta_d|^2 = \Delta_s^2 + \Delta_d^2$ shows that the full gap is always finite ($|\Delta(\mathbf{k})| > 0$).

The realization of the ground states discussed above depends on the pairing potential $V_{\mathbf{k},\mathbf{k}'}$. The BCS gap equation yields the ground state for a defined pairing potential as created by the underlying pairing mechanism. The actual mechanism in IBSs remains elusive and is strongly debated. Hence, the results for pairing mechanisms based on phonons, fluctuations and AFM exchange as listed in Fig. 2.11 will be discussed in the following. In the case of phonon-mediated pairing, both attractive channels cooperate and form an s^{++} ground state. A d -wave channel is also present but negligible [113–115]. Fluctuation-mediated pairing contains spin [49, 58, 77], charge [116] and orbital [117, 118] channels [15]. As spin-fluctuation interactions are repulsive they form a sign-changing s^{\pm} -wave or $d_{x^2-y^2}$ -wave ground state. In the case of charge-fluctuation mediated pairing the states e^+ and h^+ are present

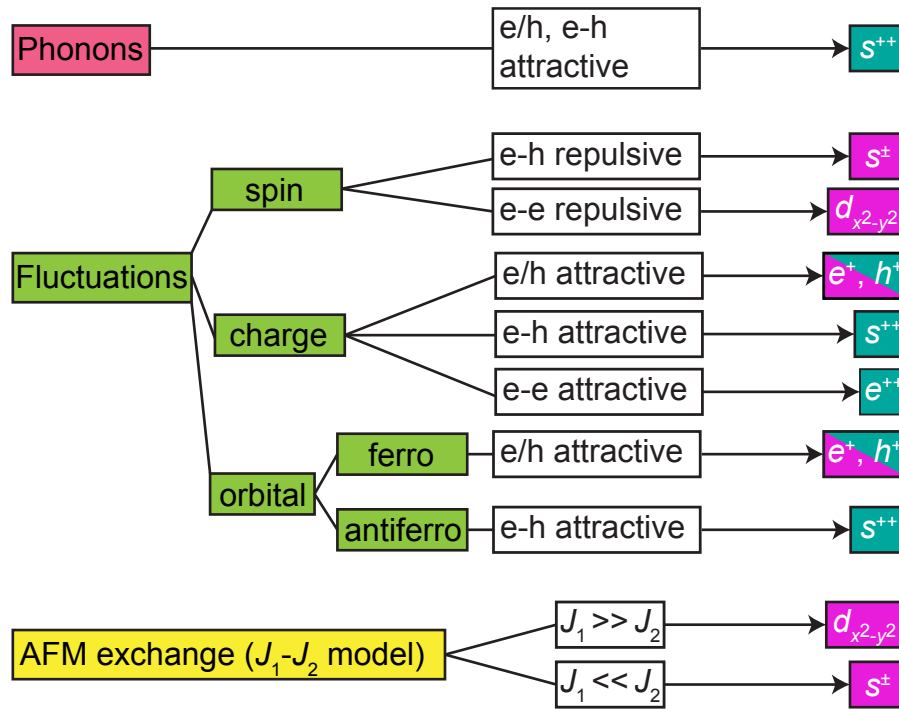


Figure 2.11: Interactions compiled as a tree diagram. Three candidates for the pairing mechanism are shown: Phonons, fluctuations, and anti-ferromagnetic (AFM) exchange interactions. They split into a variety of interactions in momentum space and resulting superconducting ground states. In this context, “e/h” stands for independent intra-band pairing in the electron (e) and hole (h) pockets. “e-e” and “e-h” describes inter-band pairing between two neighboring electron pockets and between electron and hole pockets, respectively. The resulting ground states are described by sign-preserving (turquoise) and sign-changing (pink) order parameters. A combination of both colors indicates that sign-changing and sign-preserving states are possible. s^{++} , s^{\pm} and $d_{x^2-y^2}$ correspond to the states as illustrated in Fig. 2.10(a), (c), and (d), respectively. Furthermore it is defined that e^{++} is a sign-preserving state between neighboring electron pockets, and e^+ as well as h^+ is sign-preserving within a single electron and hole pocket, respectively.

for the topmost channel. As both charge and ferro-orbital interactions rely on a small momentum transfer the relative sign between hole and electron pocket is not defined *a priori*. The smallest inter-band interaction or a form factor (e.g. $d_{x^2-y^2}$ symmetry) attributed to one of these channels determines the relative sign [119–121]. If the interaction between the Fe d - and As p - orbitals is included, the charge channel contains two more possible pairing channels [116]. The antiferro-orbital inter-band attractive interaction generates the sign-preserving s^{++} state. Pairing via AFM exchange yields the states $d_{x^2-y^2}$ and s^\pm . In the case of $J_1 \gg J_2$ the second strongest channel is a nodal s -wave state whereas a d_{xy} -wave state is subdominant for $J_1 \ll J_2$ [87–89, 122].

Chapter 3

Experiment

Here a brief introduction to Raman spectroscopy [55, 123] is given and the experimental setup is explained. Furthermore, a characterization of the investigated samples is presented.

3.1 Samples

A main aspect of this thesis is the study of the superconducting state in the hole-doped compound $\text{Ba}_{1-x}\text{K}_x\text{Fe}_2\text{As}_2$ in the range $0.22 \leq x \leq 0.70$. Fluctuations were investigated in the hole- and electron-doped samples at $x = 0.22$ and, respectively $y = 0.051$ in $\text{Ba}(\text{Fe}_{1-y}\text{Co}_y)_2\text{As}_2$. The data were compared to previously obtained results for undoped BaFe_2As_2 and $y = 0.025, 0.55, 0.61$ and 0.085 (cf. Refs. [73, 124, 125]).

Both electron- and hole-doped compounds were grown from FeAs self-flux. The elements Ba, K/Co, and prereacted FeAs were mixed in the desired ratio, enclosed in Al_2O_3 crucibles, and heated up in steps to 1000-1200 °C. For a temperature range of about 200 °C a small cooling rate in the range of 0.1-10 °C/h was applied [60, 65, 126–130]. During this process the single crystals grow. When the crystals reach their typical size of 5x5 mm (in the ab plane) and a thickness (along the c axis) of approximately 1 mm, the crucible is tilted to separate the flux from the crystals.

The K-doped crystals were grown in the groups of Thomas Wolf [65, 128] at the Karlsruhe Institute of Technology and Hai-Hu Wen at the National Laboratory for Superconductivity in Beijing [130], the Co-doped samples in the group of Ian Fisher at Stanford University [60].

The samples were characterized by determining the superconducting transition temperature T_c and the structural ordering temperature T_s . In the case of electron

doping, the SDW transition temperature T_{SDW} was obtained separately as it differs from T_s .

3.1.1 $\text{Ba}_{1-x}\text{K}_x\text{Fe}_2\text{As}_2$

The superconducting transition of the bulk was investigated by a contactless AC magnetic susceptibility measurement. An oscillating external field was applied parallel to the c -axis. In a type-II superconductor the magnetic field creates vortices which are usually pinned by defects. The depinning results in a hysteretic magnetization and the generation of higher harmonic contributions to the AC susceptibility which can be described by a Fourier series. Here the magnetic susceptibility of the third harmonic channel χ_3 was measured. Pick-up coils were used to obtain the magnetization of the sample via the induced voltage. A lock-in amplifier isolated the contribution at three times the frequency of the applied field. A detailed description is found in Ref. [131].

The amplitude of the induced voltage V_3^0 is proportional to $|\chi_3|$ and is plotted in Fig. 3.1 for all BKFA samples studied. The susceptibility is a measure for the dis-

Table 3.1: Superconducting transition temperature T_c and variation ΔT_c of differently doped samples $\text{Ba}_{1-x}\text{K}_x\text{Fe}_2\text{As}_2$ as obtained from Fig. 3.1. The sample ID refers to the documentation of this thesis.

K-content x	T_c (K)	ΔT_c (K)	Sample grower	Sample ID
0.22	24.6	0.9	T. Wolf	151111
0.25	30.9	2.1	H.-H. Wen	140728
0.35	38.9	0.9	T. Wolf	141001
0.40	38.6	0.4	H.-H. Wen	100909
0.43	36.7	1.3	T. Wolf	150218
0.48	34.3	1.1	T. Wolf	141027
0.62	26.6	1.4	T. Wolf	150115
0.70	21.6	0.8	T. Wolf	150717

sipation in the system. As long as $T \lesssim T_c$, the external field can move the vortices and energy is dissipated resulting in a finite susceptibility. For smaller temperatures however, the pinning potential increases and the vortices stay fixed at their position. When the sample is cooled, the signal is expected to set in abruptly at T_c and form an asymmetric peak [132]. However, in most of the samples a slow increase, a “foot”, precedes this peak. The width of this foot is associated with the variation ΔT_c of T_c , as caused e.g. by spatial inhomogeneities in the doping concentration or

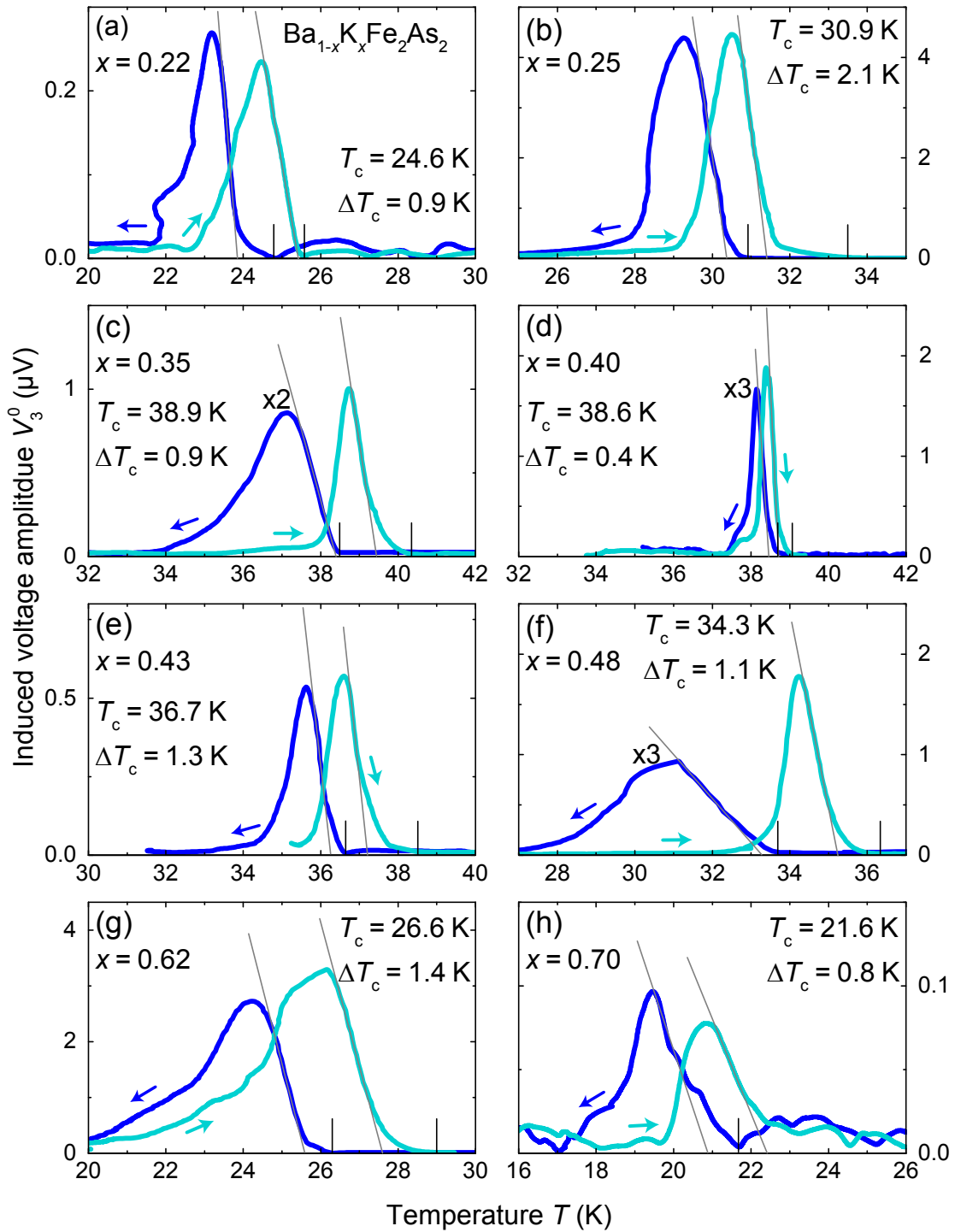


Figure 3.1: The superconducting transition in $\text{Ba}_{1-x}\text{K}_x\text{Fe}_2\text{As}_2$. Measurements of V_3^0 as a function of temperature for various doping levels are presented. For comparison, the temperature range extends over 10 K for every panel. The grey lines illustrate the linear extrapolation of the right flank, the black lines indicate the temperature, where the signal starts to emerge out of the noise, determining T_c and ΔT_c , respectively. (a) shows a small bump on the left flank at 22 K, which is an artifact caused by a fluctuating cooling rate.

disorder. The extrapolation of the linear part of the right hand side of the peak we define as T_c . Here, the resistivity is already zero and the static susceptibility reaches its midpoint.

The voltage V_3^0 was recorded as a function of temperature upon cooling and warming the sample through the superconducting transition with a typical rate of 2 K/min. Averaging over both measurements yields T_c as listed in Table 3.1 for $0.22 \leq x \leq 0.70$. For ΔT_c the maximal value is reported.

For $x = 0.22$ the structural transition temperature T_s was determined in addition to the superconducting transition at T_c . For this sample, T_s and T_{SDW} are identical. Below T_s the 1 Fe unit cell changes from tetragonal to orthorhombic and twin boundaries form [133]. This structural transition was identified by exploiting the emergence of stripes on the surface of the sample [73, 74, 125, 134, 135]. The stripes can be observed on the sample surface in the focus of the laser and are oriented along the crystallographic axes a or b . They appear abruptly below a certain temperature.

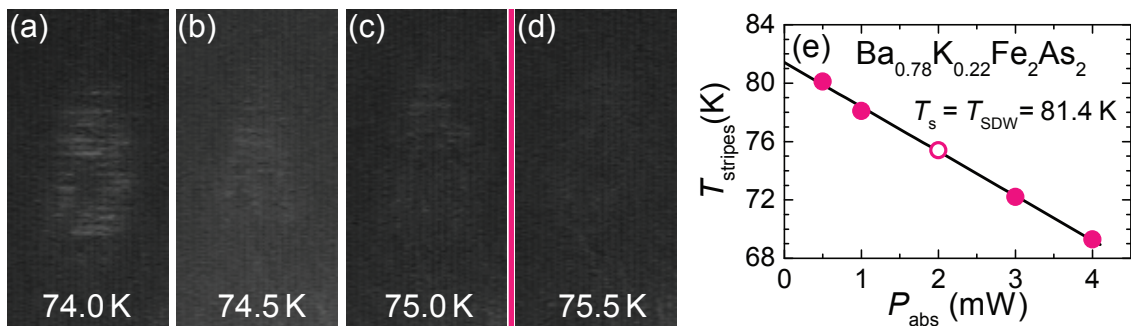


Figure 3.2: Determination of T_s by the observation of stripes [135]. (a-d) show the elastically scattered light from the laser focus on the sample surface. These images were taken with an absorbed laser power of 2 mW. The temperature indicated is that of the sample holder. The stripes, which can be clearly observed at 74.0 K fade towards higher temperatures and vanish between 75.0 K and 75.5 K. (e) The transition temperature T_{stripes} , indicated for 2 mW by the pink bar is determined for several absorbed laser powers P_{abs} . The open symbol corresponds to T_{stripes} as obtained from the images on the left, the black line shows a linear extrapolation to $P_{\text{abs}} = 0$.

As twin boundaries are deviations from the perfect crystal, they can generate an increased polarity at the sample surface, resulting in the adsorption of molecules of the residual gas in the cryostat. The light is scattered elastically from these molecules and makes the twin boundaries visible as stripes. This is displayed in Fig. 3.2. As the laser light is partially absorbed inside the sample, the sample temperature is slightly increased in the focus. Accordingly, the transition temperature T_{stripes} is obtained as a function of the absorbed laser power P_{abs} , shown in (e). The observed

linear dependence yielded $T_s = 81.4$ K and the laser-induced heating of 3.0 K/mW. As T_s could be determined with an uncertainty of 0.2 K, the doping in the laser focus is very homogeneous.

3.1.2 $\text{Ba}(\text{Fe}_{1-y}\text{Co}_y)_2\text{As}_2$

A similar analysis was performed for the Co-doped compound for $y = 0.051$, see Fig. 3.3. Here, the structural transition temperature is $T_s = 60.9$ K, the laser-induced

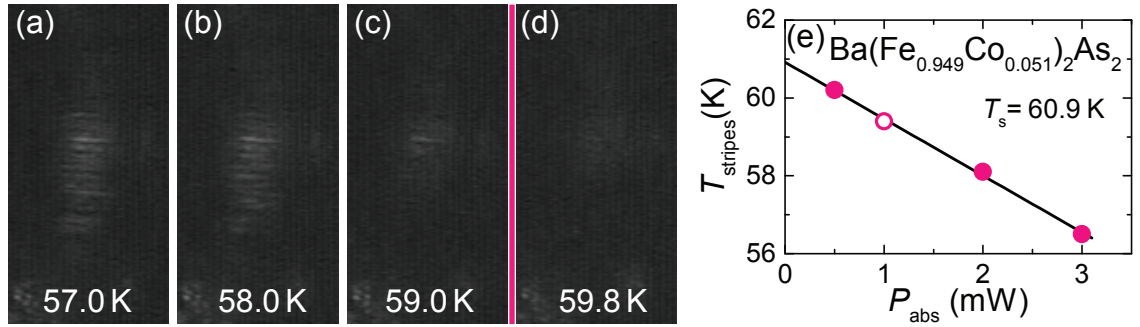


Figure 3.3: Determination of T_s in $\text{Ba}(\text{Fe}_{0.949}\text{Co}_{0.051})_2\text{As}_2$ [134]. The figure is built up in analogy to Fig. 3.2. (a-d) show the stripes at $P_{\text{abs}} = 1$ mW.

Table 3.2: Structural (T_s) and SDW (T_{SDW}) transition temperatures of the samples referred to in this thesis ($\text{Ba}_{1-x}\text{K}_x\text{Fe}_2\text{As}_2$ and $\text{Ba}(\text{Fe}_{1-y}\text{Co}_y)_2\text{As}_2$). The references lead to the corresponding Raman measurements.

K,Co-content	T_s (K)	T_{SDW} (K)	Sample ID	References
$x = 0.22$	81.4	81.4	151111	this thesis, [135]
$x, y = 0.000$	135	135	100310	[124, 136]
$y = 0.025$	102.5	98	131028	[124, 125]
$y = 0.051$	60.9	49.5	150330, 100121	this thesis, [124, 134]
$y = 0.055$	unknown		090810	[124]
$y = 0.061$	not existent		090126	[124]
$y = 0.085$	not existent		090723, 110123	[124]

heating was found to be 1.5 K/mW.

According to the phase diagram of Fig. 2.1, the SDW transition is expected to be approximately 10 K below T_s . With the help of Raman scattering the temperature $T_{\text{SDW}} = 49.5$ K was determined as explained in Appendix 7.5.

The study of fluctuations in this thesis is an extension of earlier work on differently doped samples [124, 125]. All the samples compiled in Tab. 3.2 are taken into account to analyze the phase diagram of fluctuations.

3.2 Raman spectroscopy

Raman spectroscopy is equivalent with inelastic light scattering [55, 123, 137]. A photon of momentum \mathbf{k}_i , frequency ω_i and polarization \mathbf{e}_i hits a sample, and the scattered photon (\mathbf{k}_s , ω_s , \mathbf{e}_s) is analyzed. In the scattering process an excitation in the sample is either created or annihilated. The first process is called Stokes

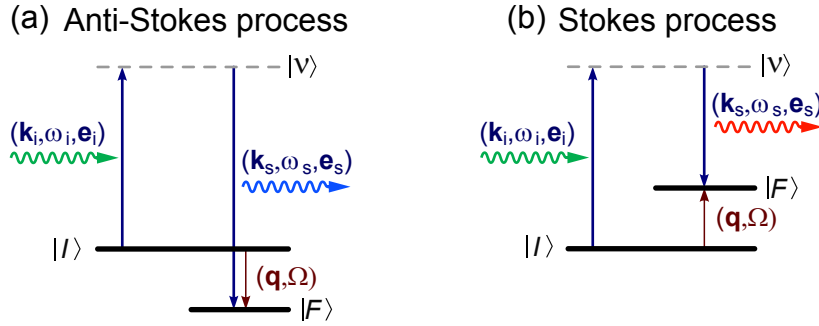


Figure 3.4: Energy level diagram of the Raman effect. The energy levels of the initial $|I\rangle$, intermediate $|\nu\rangle$, and final state $|F\rangle$ are depicted. (a) shows the Anti-Stokes process where an excitation is destroyed and (b) the Stokes process where an excitation is created. Hence the incident photon (green wavy line) transform into a blue- or red-shifted scattered photon, respectively.

process, in this case the scattered photon is red-shifted and leaves the sample with a lower energy than the incident photon. The annihilation of an excitation is called Anti-Stokes process, and the scattered photon is blue-shifted. Both processes are shown in Fig. 3.4. Here the incident photon creates an electron-hole pair in the state $|\nu\rangle$, which in general is not an eigenstate, out of the initial state $|I\rangle$. If this intermediate state happens to be a real state, e.g. an electron is lifted above a band gap, the scattering intensity can be strongly enhanced. In either case, the electron-hole pair emits (absorbs) an excitation, recombines and emits a red-shifted (blue-shifted) scattered photon, leaving the sample in the final state $|F\rangle$.

The Raman shift $\Omega = \omega_s - \omega_i$ probes the energy of the excitation. In a Raman spectrum, the scattering intensity is measured as a function of the Raman shift Ω . Due to the dispersion of light, high energies and small momenta are transferred. Hence the momentum of a probed excitation is close to zero, i.e. $\mathbf{q} \approx 0$ [138]. Some

the desired wavelength and deflect the plasma lines produced by the ion laser. To adjust the power absorbed in the sample and set the polarization, additional optical elements are needed. The power is regulated by rotating the $\lambda/2$ wave plate with respect to the polarizer P. The combination of the polarizer P and the Soleil-Babinet compensator SBC modifies the polarization in a way that any elliptical polarization can be set. The polarization outside the sample is chosen in a way that the desired polarization results inside the sample. A detailed explanation can be found in Ref. [139]. The lens L8 focuses the beam on the sample surface, which is the ab -plane for all measurements in this thesis.

The scattered light is collected along the surface normal by an objective O2. A $\lambda/4$ wave plate and another polarizer are used to select either linearly or circularly polarized light. Another $\lambda/2$ wave plate rotates the polarization into the direction of the highest sensitivity of the spectrometer. The spectrometer selects a small window of photon energies. This window can be set manually to choose the energy resolution; a typical value is 5 cm^{-1} (0.6 meV). The CCD camera counts the photons passing through the band pass. Finally, a computer controls the position of the spectrometer, reads the CCD and associates the recorded intensities (photon counts per second and absorbed power P_{abs}) with the Raman shift Ω (in units of cm^{-1}) and a spectrum is generated.

Chapter 4

Theory

In this chapter the interpretation of the Raman response is addressed from a theoretical point of view. First, electronic Raman scattering is described in general and then certain processes are studied: These are (i) Cooper-pair-breaking processes in the superconducting ground state [55, 123, 140–143], (ii) excitations in the presence of residual interactions emerging in the spectra as “Bardasis-Schrieffer” (BS) modes [43, 45, 46] and (iii) fluctuations above the SDW phase appearing only as higher-order processes, described by the so-called “Aslamasov-Larkin” (AL) [72, 108, 144, 145] diagrams. The quantitative analysis using a 3-dimensional model of the doping-dependent Fermi surface [48] was implemented during this thesis. Therefore, Raman scattering in the superconducting state is discussed in detail here.

4.1 Basic principles of electronic Raman scattering

In a Raman scattering experiment the reaction of a system to an external perturbation by photons is investigated. On the basis of a linear response theory the scattered light can be linked to the incident light via a susceptibility [146]. The derivation of this susceptibility is outlined briefly in the following. Several authors elaborated on this derivation in detail [55, 123, 147–152]. Only the major physical steps are presented here following by and large Ref. [55].

4.1.1 Fermi's golden rule

The calculation of any transition rate from an initial to a final state is described by Fermi's golden rule, which is the main ingredient to obtain the scattering cross section. Applied to Raman scattering this reads [55]

$$\frac{\partial^2 \sigma}{\partial \Omega \partial \omega_s} = \hbar r_0^2 \frac{\omega_s}{\omega_i} \frac{1}{\mathcal{Z}} \sum_{I,F} e^{-\beta E_I} |M_{F,I}|^2 \delta(E_F - E_I - \hbar \Omega) \quad (4.1)$$

with the Raman shift Ω , the frequency of the incident and scattered light ω_i and ω_s , respectively, the Thompson radius $r_0 = e^2/mc^2$, and the partition function \mathcal{Z} . The sum includes $\beta = 1/k_B T$, the energies $E_{I,F}$ of the initial (I) and final (F) states and the matrix element $M_{F,I} = \langle F|M|I \rangle$, where M is the effective light-scattering operator, transforming I to F .

I and F describe states of the many electron system. The interaction with light transforms I to F , as specified by an interaction Hamiltonian. It is emphasized that this interaction Hamiltonian especially contains the polarizations of the incident and scattered light, \mathbf{e}_i and \mathbf{e}_s , respectively.

With the explicit form of the light-scattering operator M , the summation over all final states F and the thermal averaging over the initial states I , the cross section can be rewritten as [55]

$$\frac{\partial^2 \sigma}{\partial \Omega \partial \omega_s} = \hbar r_0^2 \frac{\omega_s}{\omega_i} \sum_I \frac{e^{-\beta E_I}}{\mathcal{Z}} \int d\tau e^{-\beta \Omega \tau} \langle I|T_\tau \tilde{\rho}(\mathbf{q}, \tau) \tilde{\rho}(-\mathbf{q}, 0)|I \rangle \quad (4.2)$$

with T_τ the time-ordering operator with respect to the complex time τ and the Raman density [55]

$$\tilde{\rho}(\mathbf{q}) = \sum_{\mathbf{k}, \sigma} \gamma(\mathbf{k}, \mathbf{q}) c_{\mathbf{k}+\mathbf{q}, \sigma}^\dagger c_{\mathbf{k}, \sigma}, \quad (4.3)$$

including the Raman vertex γ and fermionic creation and annihilation operators c^\dagger and c . The polarizations \mathbf{e}_i and \mathbf{e}_s are now incorporated in the Raman vertex.

The general result is a density-density correlation function giving the scattering cross section (4.2), which can now be compared to the experiment. However, within this equation, only the coupling of the electronic density to the light is described. If bosons such as phonons, magnons, or spin fluctuations are available and Raman active, corrections must be included, which will be discussed in the following parts. An adequate description of these corrections is the goal of a theoretical approach, ideally embedded in a microscopic picture.

4.1.2 Raman susceptibility

For this aim Feynman diagrams are used to illustrate the relevant processes. Evaluating the Feynman diagrams yields the Raman susceptibility χ . The quantity extracted from the experiment is $\chi'' = \text{Im}(\chi)$, the imaginary part describing dissipative processes. The fluctuation-dissipation theorem relates the cross section with the imaginary part of the susceptibility by [55, 107]

$$\frac{\partial^2 \sigma}{\partial \Omega \partial \omega_s} \propto -[1 + n(\Omega, T)] \chi''(\mathbf{q}, \Omega) \quad (4.4)$$

with the Bose-Einstein distribution $n(\Omega, T)$.

The general Feynman diagram of a Raman scattering process is shown in Fig. 4.1. The coupling of light with electrons is described by the Raman vertex γ . This part was extracted in the previous section. Without any excitations or interactions the

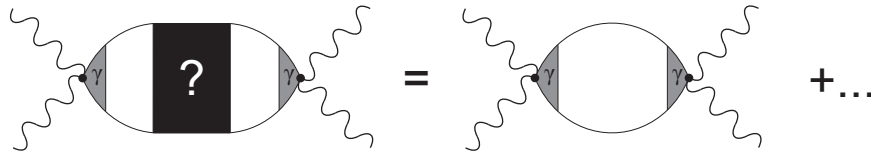


Figure 4.1: Feynman diagram of the general Raman response. Wavy lines indicate incident and scattered photons, solid lines electronic propagators. The vertex, that couples the electrons to the light is the Raman vertex γ . The black box incorporates all the interactions and excitations in the system. If none are present, only the bare bubble on the right hand side remains.

first-order diagram on the right hand side, the “bare bubble” builds up the full response. In the normal state, this diagram describes particle-hole excitations. The black box incorporates all higher order renormalizations of the bare bubble.

For example, a bosonic optical phonon propagator can be introduced, yielding a peak in the Raman spectrum at the characteristic phonon frequency. The phonon eigenvectors are determined by the symmetry operations of the crystal (and can be described by irreducible representations of the crystal’s point group), which can be extracted as well. The Raman vertex links the photon polarizations and the eigenvectors, yielding symmetry selection rules.

4.1.3 Selection rules

Selection rules are not only applicable to phonons. They are applicable to any kind of excitation. The Raman vertex shows a crucial dependence on the polarization of the incident and scattered light [153, 154]. Therefore the vertex is decomposed into symmetries μ . Depending on the choice of \mathbf{e}_i and \mathbf{e}_s certain symmetries μ are

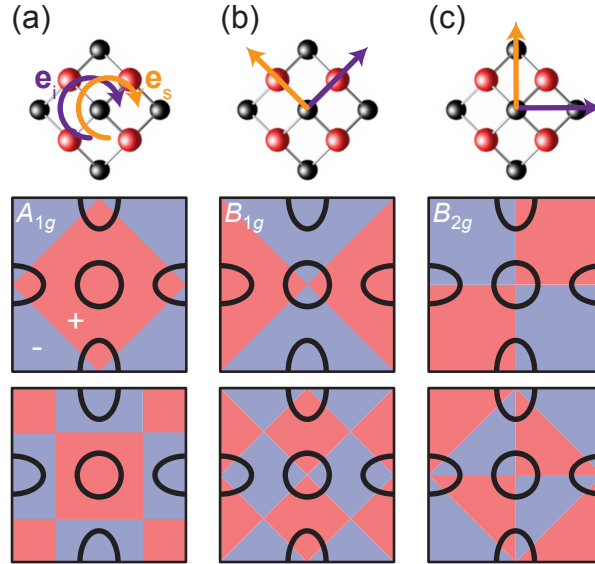


Figure 4.2: Polarization configurations and graphical representations of A_{1g} , B_{1g} and B_{2g} symmetries [154]. The signs of these representations correspond to the signs of the respective Raman vertex. The polarization configurations are indicated on the FeAs-layer. The round arrows display circular polarized light, the straight ones linear polarized light. The lowest order A_{1g} symmetry is a constant and not shown here.

isolated. Thus the Raman vertex can be described by three properties: (i) A basis set of Raman vertices can be obtained with elements γ_μ assigned to every even symmetry μ , (ii) depending on the symmetry, the vertex highlights the response from electrons having certain momenta in the BZ, and (iii) the vertex is enhanced if the incident or scattered photon energy is close to a band gap.

The first property will be investigated in detail. Fig. 4.2 shows the sign of the Raman vertex γ_μ in the BZ, indicated along with the Fermi surfaces for the first and second order. The Raman vertex has a node ($\gamma = 0$) at the momenta, where positive and negative areas touch. Here only symmetries $\mu \in \{A_{1g}, B_{1g}, B_{2g}\}$ are shown. The response in A_{2g} symmetry is typically very small and neglected here. The E_g symmetry is defined with respect to the ac and bc planes, hence not relevant as well. For certain polarization configurations \mathbf{e}_i , \mathbf{e}_s , the response from excitations having different symmetries is projected out. This is a vital part of the experimental

analysis, as the symmetry of an excitation encodes valuable information about its nature.

4.2 Raman response in the presence of interactions

Specific interactions and excitations are studied in the following replacing the black box in the Feynman diagram of Fig. 4.1. From a theoretical point of view, these interactions and excitations can be described by bosonic propagators.

4.2.1 Coupling between electrons and fluctuations in the normal state

The phase diagram of Fig. 2.1 showed a region above the SDW state, where fluctuations are expected to appear. Yet the nature of these fluctuations remains unknown. The question arises, if Raman scattering can probe these fluctuations and which results can be obtained from the experiment.

To address the first point the bare bubble is renormalized by introducing a bosonic fluctuation propagator. Several diagrams can be constructed involving a certain

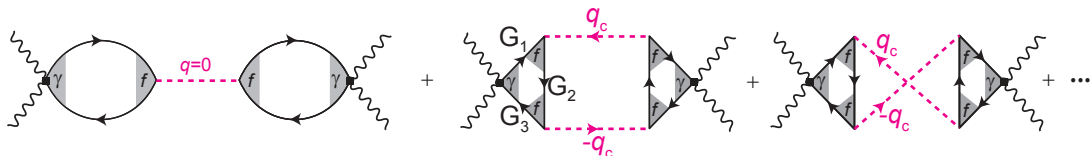


Figure 4.3: Raman scattering processes involving one (first-order) and two (second-order) fluctuations. Solid lines are fermionic propagators with the corresponding Green's functions G_i , dashed pink lines fluctuation propagators, and wavy lines are photons. The Raman vertex γ and the form factor f describe the interaction of fermions with light and fluctuations, respectively. Both processes provide for a vanishing net momentum. The fermionic triangles of the second order processes are called “electronic loops”.

number of these propagators. A selection of diagrams with one and two propagators is depicted in Fig. 4.3, the second-order diagrams are called AL diagrams [72, 108, 120, 144, 155–158]. Processes involving self-energy correction are omitted [145]. The fluctuation propagators in the case of AL diagrams can be described by the Ornstein-Zernike propagator D_{OZ} from Eq. 2.5. The diagrams show, how fluctuations can be probed by Raman scattering.

However, there are some constraints. First, no momentum can be transferred in a Raman scattering process. This is realized in the first-order diagram by a vanishing momentum of the fluctuation propagator. In the second-order diagram, any momentum \mathbf{q}_c is possible, as long as both fluctuation momenta (\mathbf{q}_c and $-\mathbf{q}_c$) cancel. Another constraint is given by the Raman vertex. In the first-order diagram, the electron-fluctuation vertex f must have the same symmetry as the Raman vertex γ to avoid cancellation. This means that a fluctuation of e.g. B_{1g} symmetry can only be observed with a polarization configuration, that projects out B_{1g} . An example for this case are charge and orbital fluctuations possessing a B_{1g} -symmetric form factor f .

This is different in the case of the second-order AL diagrams. Here, the coupling between light and fluctuations is realized via an electronic loop Λ_0^μ . The electronic loop contains the Raman vertex and, in general, form factors that are related to the symmetry of a fluctuation. However, as these form factors enter quadratically as f^2 , which is insensitive to sign changes, they are irrelevant for symmetry considerations. Thus they are usually omitted in the diagrams. A simplified form of the electronic loop, which sufficiently describes the selection rules, reads [108, 145]

$$\Lambda_0^\mu(\mathbf{q}_c) = T \sum_{\mathbf{k}} \gamma_\mu(\mathbf{k}) X G_1(\mathbf{k}) G_2(\mathbf{k} + \mathbf{q}_c) G_3(\mathbf{k}) + \text{“}\mathbf{q}_c \leftrightarrow -\mathbf{q}_c\text{”}. \quad (4.5)$$

with fermionic propagators G_1 , G_2 , and G_3 . The indices indicate different energy dependencies, X is an operator taking care of the corresponding energy integrals in the multi-band system. For further approximation, the three Green’s functions are assumed to pin the vectors \mathbf{k} and $\mathbf{k} \pm \mathbf{q}_c$ onto the Fermi surface but are irrelevant otherwise. This defines the so-called “hot spots” \mathbf{k}_0 being the origin of the vectors $\pm\mathbf{q}_c$, which connect two FS sheets. For a certain critical vector and a set of

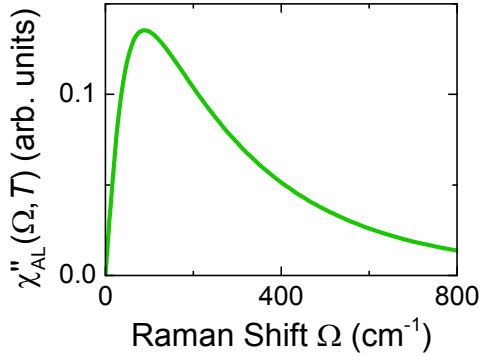


Figure 4.4: Generic Raman response as obtained from the uncrossed AL diagram involving a phenomenological fluctuation propagator. Note the finite slope for $\Omega \rightarrow 0$.

corresponding momenta \mathbf{k}_0 a simple selection rule demands

$$\Lambda_0^\mu(\mathbf{q}_c) \propto \sum_{\mathbf{k}_0} \gamma_\mu(\mathbf{k}_0) \quad (4.6)$$

to be finite for a finite response. This is only the case for adequate symmetries μ . For example, a response in μ is expected, if the critical vectors exclusively connect parts of the FS where γ_μ has the same sign. Note that this symmetry is not necessarily equal to the symmetry f of the fluctuation itself. The application of this selection rule to spin fluctuations is described in App. 7.1.

A typical Raman response as obtained from the AL diagrams (Fig. 4.3) is shown in Fig. 4.4 [47, 73, 108, 145]. From this response several properties of the fluctuations can be extracted. The selection rules hint towards the critical vectors \mathbf{q}_c . The mass m , which is an intrinsic property of the propagator D_{OZ} as defined in Eq. 2.5 (dashed pink lines in the AL diagrams of Fig. 4.3) can be obtained as a function of doping and temperature.

4.2.2 Interactions in a multi-band superconductor

To describe the response of a superconductor, the lowest order diagram (the bare bubble) is sufficient. The propagators in the superconducting state are different from those above T_c . A gapped system can still be described by the single-particle Green's function (propagator) [159],

$$G(\mathbf{k}, i\omega_n) = -\frac{i\omega_n + E_{\mathbf{k}}}{(i\omega_n)^2 + E_{\mathbf{k}} + \Delta_{\mathbf{k}}^2}, \quad (4.7)$$

it is the coherence of the state that requires another propagator to be taken into account, the anomalous Green's function

$$F(\mathbf{k}, i\omega_n) = F^\dagger(\mathbf{k}, i\omega_n) = \frac{\Delta_{\mathbf{k}}}{(i\omega_n)^2 + E_{\mathbf{k}} + \Delta_{\mathbf{k}}^2}. \quad (4.8)$$

The response in the superconducting state is given by a coherent superposition of G and F and is illustrated in Fig. 4.5.

An important conclusion can be derived from these diagrams. Evaluating the diagrams yields a Raman response which depends quadratically on $\gamma_\mu(\mathbf{k})$. As $\gamma_\mu^2(\mathbf{k})$ is positive, sign-changes as e.g. in B_{1g} symmetry cannot be resolved, i.e. the symmetry selection rules are lost. However, the selectivity in momentum space is still preserved. This means, that every symmetry μ individually highlights or attenuates

the response originating from certain parts of the Fermi surface, according to the momentum dependence of $\gamma_\mu^2(\mathbf{k})$.

The Raman response at $T = 0$ for the simplest case of an isotropic gap 2Δ and a

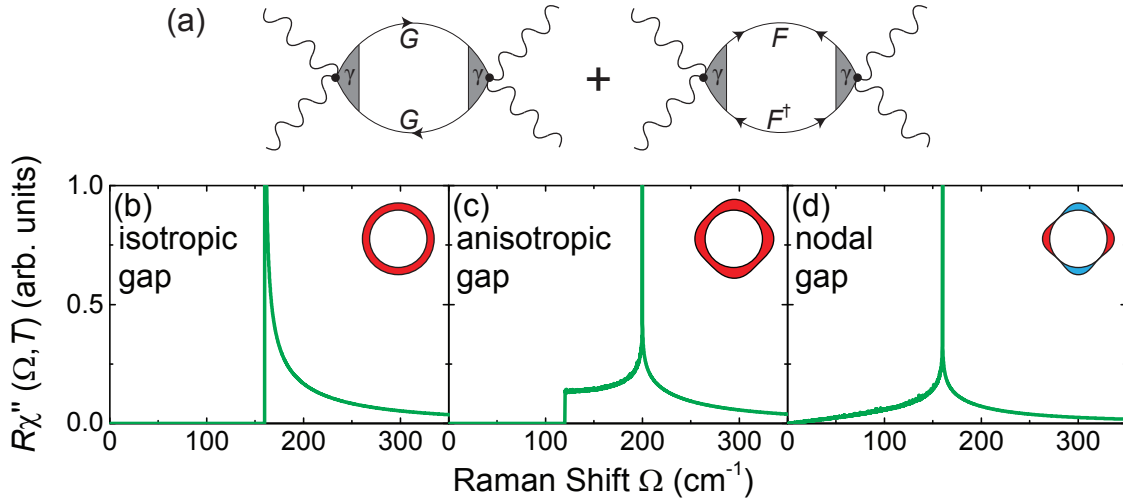


Figure 4.5: Feynman diagrams and corresponding response from the superconducting gap [160]. (a) Wavy lines illustrate photons, solid lines with a single arrow indicate normal Green's functions G and double-arrow lines anomalous Green's functions F and F^\dagger . The Raman vertices γ are highlighted in grey. (b-d) show the response for different \mathbf{k} -dependent gaps in the approximation of a constant Raman vertex. The corresponding gaps are presented in the insets, according to the gaps on the hole pockets of Fig. 2.10(a), (b), and (d).

constant Raman vertex is depicted in Fig. 4.5(b). The response vanishes inside the gap, i.e. below 2Δ , as there are no available states. Above 2Δ the equal contributions from the two diagrams form a square-root singularity right at 2Δ followed by a monotonic decay. Two further examples are shown in (c) and (d), the Raman vertex is still kept constant. The response of an anisotropic gap exhibits a “step-peak” structure, the step is located at $2\Delta_{\min}$, the peak at $2\Delta_{\max}$. For higher energies the typical decay is observed. In the case of a nodal gap as in (d) the response never vanishes. For every energy a pair-breaking process can occur, as the gap ranges from zero to $2\Delta_{\max}$. At twice the maximum gap, a peak is present.

In a multi-band system, the total response is simply the sum of the response from every band. In principle, isotropic gaps on n bands can produce n peaks in the Raman spectrum at $2\Delta_n$.

In A_{1g} symmetry however, the spectra are modified by a screening term. The screening originates from Coulomb-interaction, which can couple only to the totally symmetric A_{1g} Raman vertex. In this case the bare bubble is renormalized by an infinite

series of diagrams as illustrated in Fig. 4.6. A summation in a 5-band model yields the renormalized response [143]

$$\chi_{\text{sc}}^{\gamma\gamma} = \sum_{a=1}^5 \chi_a^{\gamma\gamma} + V \sum_{a,b=1}^5 \chi_a^{\gamma 1} \chi_b^{1\gamma} \sum_{n=0}^{\infty} \chi_{\text{C}}^n \quad (4.9)$$

with

$$\chi_{\text{C}} = V \sum_{i=1}^5 \chi_i^{11}. \quad (4.10)$$

Here, χ_i^{pq} describes the bare bubble on band i with vertices p and q being either γ for the coupling to light or 1 for the coupling by the Coulomb interaction. Evaluating

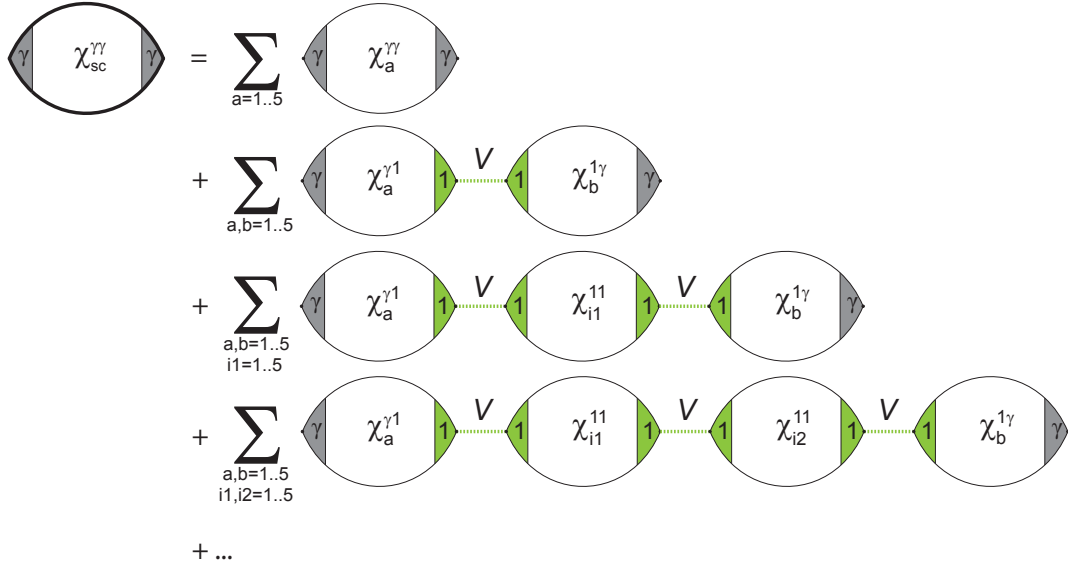


Figure 4.6: Multi-band screening in A_{1g} symmetry. The renormalized susceptibility $\chi_{\text{sc}}^{\gamma\gamma}$ is obtained by the evaluation of a geometric series, involving the Coulomb-interaction V (green dashed line) coupling via the totally symmetric vertex 1. The combination of the vertices yields the susceptibilities $\chi^{\gamma\gamma}$, $\chi^{\gamma 1}$, $\chi^{1\gamma}$, and χ^{11} . Band indices range from 1 to 5 in the case of a 5-band model. Wavy photon lines are omitted.

the geometric series and using the equality $\chi^{\gamma 1} = \chi^{1\gamma}$ the relation

$$\chi_{\text{sc}}^{\gamma\gamma} = \sum_{a=1}^5 \chi_a^{\gamma\gamma} + \left(\sum_{a=1}^5 \chi_a^{\gamma 1} \right)^2 \frac{V}{1 - V \sum_{i=1}^5 \chi_i^{11}} \quad (4.11)$$

is found. For a large Coulomb interaction V this simplifies to

$$\chi_{sc}^{\gamma\gamma} = \sum_{a=1}^5 \chi_a^{\gamma\gamma} - \frac{(\sum_{a=1}^5 \chi_a^{\gamma 1})^2}{\sum_{i=1}^5 \chi_i^{11}} \quad (4.12)$$

and shows, that screening is determined mostly by the sum $\sum_{a=1}^5 \chi_a^{\gamma 1}$, where γ enters linearly. If the sum is large, a huge screening effect is expected, reducing the response considerably. A_{1g} is the only symmetry, where positive and negative regions of $\gamma(\mathbf{k})$ do not (necessarily) add up equally. Hence screening can have an influence in A_{1g} symmetry only.

4.3 Bardasis-Schrieffer mode

Another possible excitation, that replaces the black box, is the BS mode [43, 45–47, 155, 161–163]. A BS mode is a collective, bosonic mode in the superconducting state. Such a mode exists if the pairing interaction $V_{\mathbf{k},\mathbf{k}'}$ between the electrons of a Cooper

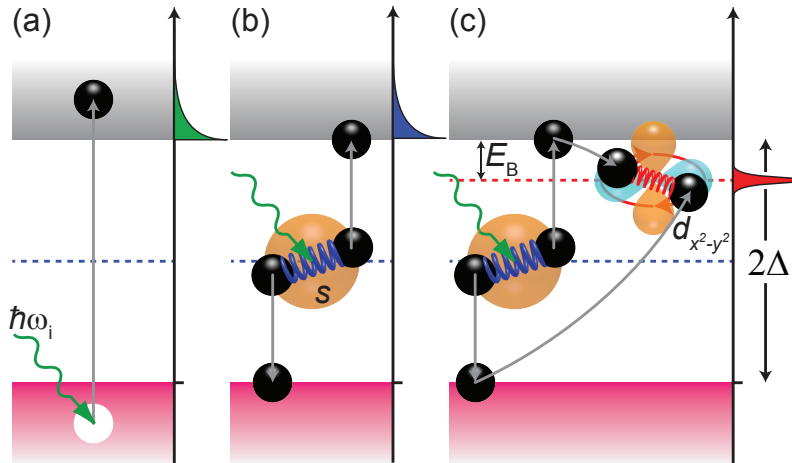


Figure 4.7: Combined processes yielding the Raman response in the presence of a subdominant interaction [47, 162]. Occupied and unoccupied bands of a superconductor are shown in pink and grey, respectively. The dashed line in the middle illustrates the Fermi energy. (a) The incident photon lifts an electron (black) above the superconducting gap 2Δ . (b) A Cooper pair of the s -wave ground state is broken by applying an energy of 2Δ . (c) A Cooper pair is split and immediately recombines as a bound pair. The bound pair has $d_{x^2-y^2}$ symmetry, the corresponding in-gap state is split off from the unoccupied states by the binding energy E_B .

pair is not isotropic as in the BCS approximation but depends on momentum. Then it can be expanded into orthogonal functions dictated by the crystal symmetry. As

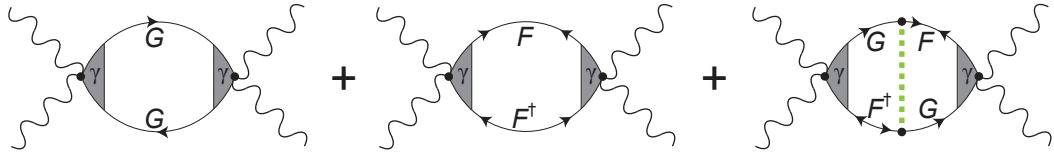


Figure 4.8: Feynman diagrams referring to the three processes of Fig. 4.7. The first two terms are responsible for the pair-breaking peak, the third diagram includes the subdominant interaction resulting in the BS mode to emerge.

an immediate consequence, there exist pairing channels beyond the superconducting ground state [43]. Usually they are much weaker than the ground state interaction. In BKFA however, pairing interactions with similar strength are present [47, 162]. As the interactions are orthogonal, they compete with each other (On the other hand, if two non-orthogonal interaction were present, they would always support each other and generate a common superconducting ground state of their symmetry). For a

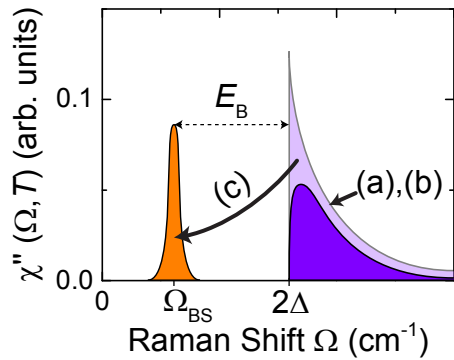


Figure 4.9: Schematic Raman response in the presence of a subdominant interaction. The pair-breaking peak above 2Δ (light purple) is generated by processes as illustrated in Fig. 4.7(a) and (b). The process shown in Fig. 4.7(c) drains spectral weight out of the pair-breaking peak into the BS mode (orange) at Ω_{BS} , leaving only a reduced pair-breaking peak (dark purple). The binding energy is determined by $E_B = 2\Delta - \Omega_{BS}$.

$\Delta_0 e^{i\varphi}$ [42]. In general, the phase has a momentum dependence and can thus be classified by symmetries. If the ground state, for example, has A_{1g} symmetry and the subdominant interaction has B_{1g} symmetry, the phase oscillates with a B_{1g} pat-

hierarchy of competing pairing interactions, the dominant interaction determines the superconducting ground state. The emergence of a BS mode in the experiment reflects the presence of a subdominant interaction.

But how can this be understood microscopically? The BS mode can be described in a particle picture and a wave picture. The wave picture illustrates the collective character of the mode and the particle picture leads to a qualitative description of the Raman response.

In the wave picture the BS mode is characterized by an oscillation of the phase φ as defined in the complex description of the gap $\Delta =$

tern. This underlines the collective behavior of the BS mode as all the Cooper pairs at the Fermi energy participate.

In contrast to that, just one Cooper pair is considered in the particle picture as illustrated in Fig. 4.7. The corresponding Feynman diagrams are illustrated in Fig. 4.8 and can be separated into three terms related to the three panels of Fig. 4.7.

The first diagram shows the bare bubble built up by the single-particle propagators G . This process is illustrated in Fig. 4.7(a). An incident photon excites one particle above the gap 2Δ . The second diagram includes the anomalous Green's function F , the corresponding process is shown in Fig. 4.7(b). A Cooper pair is broken, which costs an energy of 2Δ . Both processes combined yield the typical Raman response of a superconductor [see e.g. Fig. 4.5(b)].

In the third diagram, the subdominant interaction is introduced. This diagram refers to the combined process of Fig. 4.7(c). The electrons of the broken Cooper pair recombine as a bound pair in the gap with a binding energy E_B . This process costs an energy of $2\Delta - E_B$. At this energy a peak in the Raman spectrum is expected. An important property can be derived from the renormalized diagram. Due to the subdominant interaction the diagram decomposes into two equal halves. Each of them is described by a product of G and F and the Raman vertex enters linearly [46]. Hence the selection rules are restored (in contrast to the other two diagrams) and the symmetry of the BS mode can be determined.

All the three diagrams combined yield the total response as shown schematically in Fig. 4.9. In the absence of a subdominant interaction, a typical square-root singularity would emerge at 2Δ , as equally generated by process (a) and (b). Switching on the subdominant interaction activates process (c), resulting in two effects on the spectrum: (i) Spectral weight is drained from the pair-breaking peak and (ii) the BS mode emerges below 2Δ , split off by the binding energy E_B . An approximation yields the relative strength of the subdominant coupling parameter to be $\lambda_d/\lambda_s \approx \sqrt{E_B/2\Delta}$ for an s -wave symmetric ground state and a d -wave symmetric subdominant interaction [45].

4.4 Competing interactions embedded in a 5-band model

In Section 5.1 a quantitative analysis of the Raman spectra in the presence of interactions will be presented. To this end a band structure is required. Here the 5-band tight-binding model developed by Graser and coworkers [77] is presented, on

the basis of which the experimentally obtained Raman results are studied.

4.4.1 Rigid band model

Starting from the five Fe d -orbitals the transformation to a band basis is discussed first, then the backfolding from the 1 Fe BZ to the 2 Fe BZ is outlined for the 3-dimensional case.

The tight-binding Hamiltonian of the five d -orbitals consists of five on-site energies

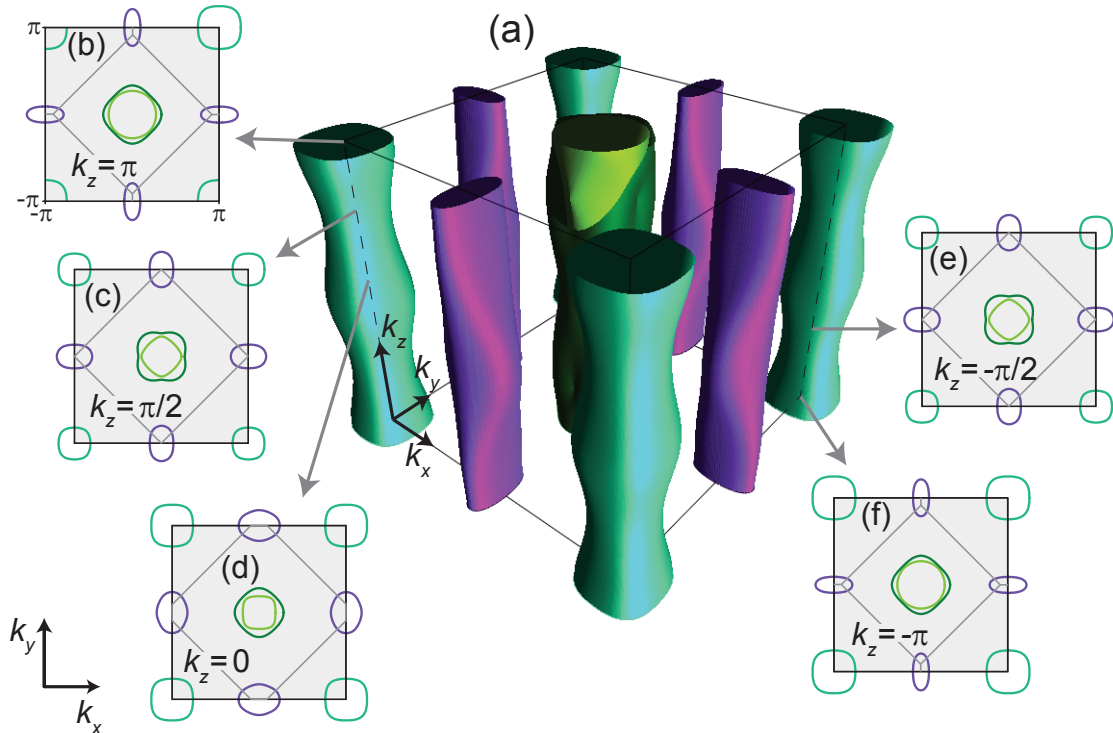


Figure 4.10: Fermi surface of the 1 Fe BZ. (a) shows the complete Fermi surface. Green surfaces depict hole pockets, purple ones electron pockets. Thin grey lines indicate the boundaries of the 1 Fe BZ, ranging from $-\pi$ to π on every axis. (b-f) displays several two-dimensional cuts at certain values of k_z . Here the black lines frame the 1 Fe BZ, the grey lines illustrate the boundaries of several adjacent 2 Fe BZs.

and ten inter-orbital hopping parameters as described by Eq. 2.1. A diagonalization performs the transformation from an orbital to a band basis, yielding five bands in the 1 Fe BZ.

As a simplification the rigid band model is used, where only the filling $6 + z$ determines the doping-dependent Fermi energy. At optimal hole doping, the K-content of 0.4 yields a filling of 5.8. The corresponding Fermi surface is shown in Fig. 4.10. Note that only three bands cross the Fermi energy, generating five different Fermi

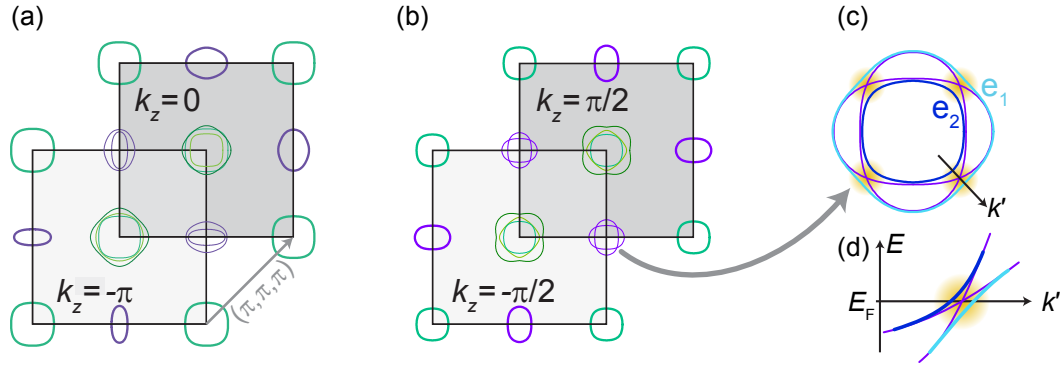


Figure 4.11: Backfolding and anticrossing. (a) Panels (f) and (d) of Fig. 4.10 are arranged on top of each other, shifted by the vector $(\pi, \pi, 0)$. As both panels differ by a value of $\Delta k_z = \pi$, the total shifting vector is (π, π, π) . (b) The same shift is illustrated for different k_z cuts. (a) shows intersecting hole pockets, (b) additionally exhibits intersecting electron pockets. (c) The intersecting electron pockets of (b) are enlarged. Lifting the degeneracies at the highlighted spots yields an outer (e_1) and inner (e_2) electron pocket. (d) illustrates the underlying splitting in energy along the diagonal vector k' .

surface sheets. Two different electron-like and three different hole-like sheets are visible. All of them encircle an axis in k_z direction. The pockets which can be shifted onto each other by the reciprocal lattice vector are considered as the same pocket.

The question arises, if the As superstructure has a significant influence on the electronic structure, as induced by finite hopping via As. Several experiments indicate an impact on the Fermi surface motivating the inclusion of the superstructure [164]. This is formally achieved by a backfolding from the 1 Fe BZ to the 2 Fe BZ. As the 2 Fe BZ follows the additional translational symmetry by the vector (π, π, π) , backfolding is equivalent to imposing this new symmetry to the band structure of the 1 Fe BZ. Thus the whole band structure is shifted by (π, π, π) , then the emerging degeneracies are lifted yielding the bands of the 2 Fe BZ.

This procedure is exemplarily demonstrated in Fig. 4.11. The three hole pockets are shifted on top of each other. The same happens for the two electron pockets. A constant splitting energy is introduced leading to three non-intersecting hole pockets and two separated electron pockets appearing as an outer and inner pocket e_1 and e_2 , respectively. Note that this reconstruction for the electron pockets only happens around $k_z = \pm\pi/2$. At $k_z = 0, \pm\pi$ the original electron pockets do not intersect each other.

The resulting Fermi surface of the 2 Fe BZ is presented in Fig. 4.12, however for reasons of simplicity still shown in the (larger) 1 Fe BZ.

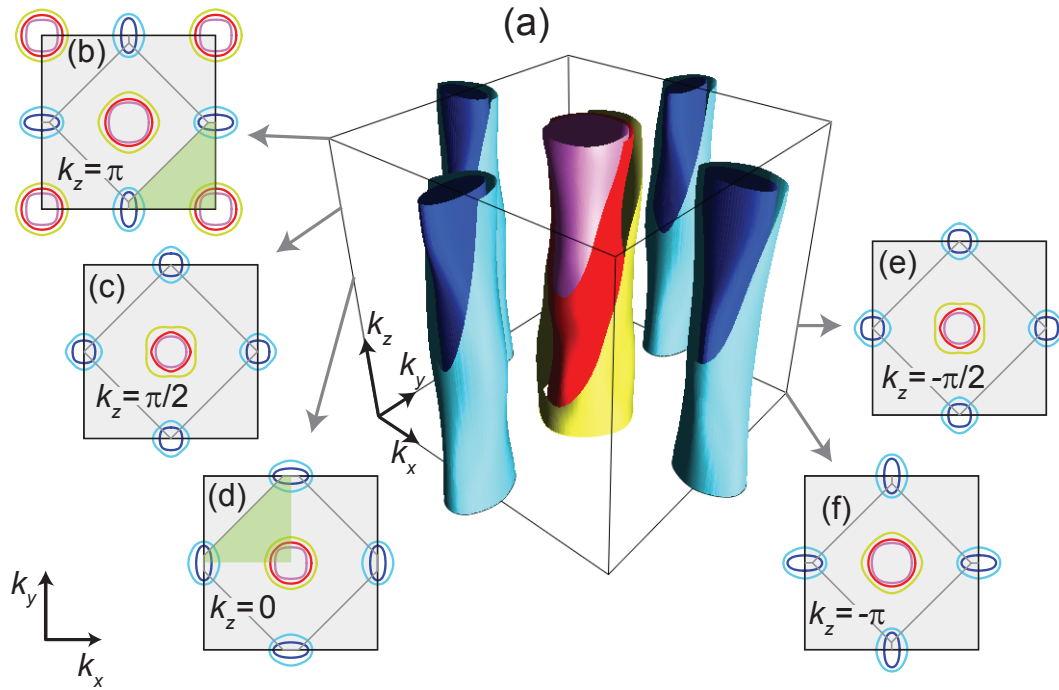


Figure 4.12: Fermi surfaces of the folded band structure. (a) The Fermi surface is still shown in the 1 Fe BZ even though the more complicated 2 Fe zone would be the correct one. Hence the Fermi surfaces can be transformed into each other by the translation operation along the vector (π, π, π) . Two new electron pockets emerge (light and dark blue) and three new hole pockets (magenta, red and yellow). (b) shows that these hole pockets are repeated at the corners of the 1 Fe BZ. They are omitted for all the following representations. (b,d) To illustrate the Fermi surface in the 2 Fe BZ, we highlighted one and the same area with respect to the 2 Fe zone by the green shaded part.

4.4.2 Gap structure and subdominant interactions

This Fermi surface structure is now used as a starting point for various interactions. The dominant interaction is responsible for the superconducting ground state, causing a gap with the energy $\Delta(\mathbf{k})$ to emerge on the Fermi surface. In combination with the Raman vertex $\gamma(\mathbf{k})$, the Raman response of this multi-band system can be obtained.

In addition to that, several subdominant interactions can be included, acting on the various Fermi pockets. These interactions are usually classified by symmetry. From a theoretical point of view, any interaction can be described by a set of eigenvalues λ_i and the corresponding eigenvectors $g_i(\mathbf{k})$. The eigenvalue is the coupling strength and the eigenvector defines the momentum dependence, i.e. is the form factor of this interaction channel, and consequently determines the symmetry.

As described above, the Raman response is modified in the presence of subdominant

interactions. Spectral weight is drained off of the pair-breaking peak and BS modes appear. One BS mode can be expected per (orthogonal) subdominant coupling channel [165].

Chapter 5

Results and Discussion

In the last chapter the way was paved for a quantitative analysis of the experimental data to be presented in the following four sections. In the first section a continuation of earlier work by Kretzschmar and coworkers [47, 125] will be described, where collective modes were found in $\text{Ba}_{0.6}\text{K}_{0.4}\text{Fe}_2\text{As}_2$. These modes were interpreted in terms of BS modes [43]. However, the experimental data left room for different explanations. New aspects were found within this work by a temperature-dependent Raman measurement and the application of a quantitative model calculation. This analysis revealed the true nature of the observed peaks and provided evidence for at least one BS mode in a multi-band superconductor. It could be concluded, that two competing pairing interactions are present, the stronger of which forming the superconducting ground state.

The hierarchy of interactions turned out to be sensitive to the size of the Fermi surface sheets and thus can be tuned by changing the doping. The doping dependence will be examined in the second section and discussed for different models of the pairing mechanism.

Fluctuations as those appearing above the SDW phase could mediate the pairing. Motivated by this possibility, the fluctuations above T_{SDW} were investigated in the third section as a function of temperature and doping, extending earlier work based on Ref. [73]. Questions as to the microscopic origin of the fluctuations, their correlation length and strength will be addressed. Special attention is paid to the question if the fluctuations reflect signatures of the electron-hole asymmetry.

Finally, a phonon anomaly at optimal doping will be discussed in the fourth section, which may open a new perspective for probing interactions or excitations in the vicinity of a QCP.

5.1 Experimental evidence for competing pairing interactions in optimally doped $\text{Ba}_{0.6}\text{K}_{0.4}\text{Fe}_2\text{As}_2$

The major step towards revealing the pairing mechanism is the knowledge of the relevant interactions. In a multi-band system, various interactions such as phonon-mediated, AFM exchange and fluctuation-based interactions (see Fig. 2.11) are present [49, 58, 77, 87, 113, 116], the intertwining of which yields the rich phenomenology of the IBSs [39, 40, 100, 117, 119, 120]. To gain insight into this complex structure of interactions, a way to disentangle them must be found. This was achieved here by (i) exploiting the Raman selection rules, (ii) analyzing the temperature evolution of the prominent features appearing in the symmetry-resolved spectra, and (iii) applying a quantitative model calculation to the experimental results of $\text{Ba}_{0.6}\text{K}_{0.4}\text{Fe}_2\text{As}_2$.

5.1.1 Symmetry analysis

Following this path, a first study sheds light on the superconducting state of optimally doped $\text{Ba}_{0.6}\text{K}_{0.4}\text{Fe}_2\text{As}_2$. The Raman experiments were realized with an excitation wavelength of $\lambda_L = 575 \text{ nm}$ and an energy resolution of 5 cm^{-1} . The results for the symmetry dependence of the Raman spectra are presented in Fig. 5.1. The spectra were collected in both the superconducting state at 10 K (light blue) and in the normal state at 44 K (orange), just above $T_c = 38.6 \text{ K}$.

To gain symmetry-resolved information, the pure symmetries A_{1g} , A_{2g} , B_{1g} , and B_{2g} [55] were extracted from spectra accessible by polarizations in the Fe-As-planes. The symmetries refer to the Brillouin zone of the 1 Fe unit cell. Linear combinations of these symmetries as obtained by polarizations RR, xy, and x'y' are shown in Fig. 5.1(a-c). All spectra have a similar contribution of A_{2g} symmetry. Including the spectra in RL polarization, the bare A_{2g} spectra could be extracted. Their contribution proved to be the smallest of all four symmetries, the A_{2g} spectra are structureless and do not change between 10 and 44 K.

This enables an identification of the various features by their pure symmetry. The features are for example the phonons [166] in (a) at 188 and in (b) at 215 cm^{-1} having A_{1g} and B_{2g} ($= B_{1g}$ with respect to the crystallographic unit cell) symmetry, respectively. Another phonon mode appears at 130 cm^{-1} in both A_{1g} and B_{2g} symmetry. This phonon has E_g symmetry but shows up in these two in-plane symmetries as the vector \mathbf{e}_i of the incoming photons has a finite projection on the c -axis if the

angle of incidence is large and \mathbf{e}_i is not perpendicular to the plane of incidence. The phonons show only little changes between the normal and superconducting state. Hence the phonons are disregarded in the following analysis, where the effects emerging in the superconducting state are explored. Except for A_{2g} , all symmetries exhibit superconductivity-induced features. These features are extracted in Fig. 5.1(d) by plotting the difference $\Delta R\chi''(\Omega) = R\chi''(\Omega, 10\text{ K}) - R\chi''(\Omega, 44\text{ K})$. This is done to minimize all the features which do not change when entering the superconducting state. Note that the phonon of B_{2g} symmetry slightly hardens and softens between 44 and 10 K. This creates the narrow artifact at 215 cm^{-1} in the B_{2g} difference spectrum which is ignored in the current analysis. It is emphasized that the temperature independence of the A_{2g} spectra enables the isolation of pure symmetries in the difference spectra. The three Raman-active symmetries exhibit various distinct features. In terms of the total spectral weight of these features, the three symmetry channels are similar.

The analysis commences with the superconducting energy gap, which is expected to open up below T_c [4, 141, 167, 168]. In a complex system like BKFA it is not surprising if multiple Fermi surfaces host several gaps with different magnitudes. This was indeed detected by several other techniques such as ARPES [75, 169], neutron scattering [170], muon spin rotation [171], infrared spectroscopy [172], scanning tunneling spectroscopy [173], specific heat [174], and critical field measurements [35]. Thus the symmetry analysis is crucial to distinguish between the response from several gaps and other features like a BS mode. In Raman spectroscopy, the opening of a gap Δ manifests itself in a reduction of scattering intensity below 2Δ in conjunction with an increase in intensity just above the gap edge.

Here the shift of spectral weight [55, 123, 147] is observed in all three symmetries. The reduction of spectral weight (negative values in $\Delta\chi''$) is followed by an increase above roughly 155 cm^{-1} . The range, in which this increase appears, is marked by the light grey shaded area in Fig. 5.1(d). Importantly, the increase sets in at a common energy for all three symmetries. Even if the peak positions for the different symmetries do not coincide in energy, it is safe to assume, that all the features above 155 cm^{-1} are pair-breaking phenomena. They originate from at least one full gap with the gap edge $2\Delta_{\min} \approx 155\text{ cm}^{-1}$. Eventually the spectra of the normal and superconducting state merge ($\Delta\chi'' \rightarrow 0$) at higher energies.

To characterize the gap another coincidence is remarkable, as indicated by the vertical grey line. Here, the superconducting B_{2g} response crosses the normal state response, the B_{1g} response exhibits a peak and the A_{1g} response shows its steepest

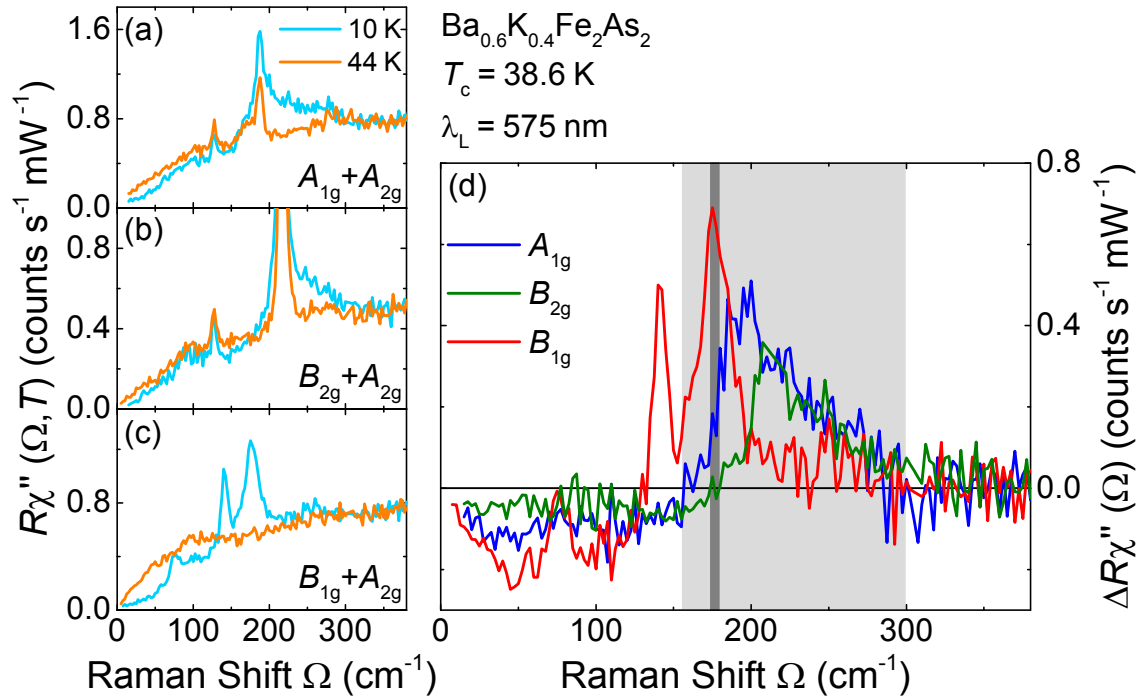


Figure 5.1: Raman spectra of $\text{Ba}_{0.6}\text{K}_{0.4}\text{Fe}_2\text{As}_2$. (a-c) show spectra in the normal (orange) and superconducting (light blue) state containing linear combinations of different symmetries. (d) As A_{2g} is temperature independent the difference spectra $\Delta R\chi''(\Omega) = R\chi''(\Omega, 10 \text{ K}) - R\chi''(\Omega, 44 \text{ K})$ resolve the bare symmetries A_{1g} , B_{2g} , and B_{1g} . Earlier measurements on the same sample with an excitation wavelength of 532 nm can be found in Refs. [47, 125].

slope. The single peak above 155 cm^{-1} is suggestive for a single more or less isotropic gap. It is likely that the same gap causes the increase of intensity in both B_{2g} and A_{1g} symmetry. This suggests that a single gap is responsible for the pair-breaking processes close to the gap edge. Another feature is a peak at about 80 cm^{-1} which is most pronounced in B_{1g} symmetry. There is a weak hump in A_{1g} symmetry at a similar energies. As the energy of this peak coincides with an ARPES measurements [75] of a smaller gap, this peak is analyzed in terms of a second pair-breaking peak. Beyond the similarities there are also distinct differences between the symmetries above 155 cm^{-1} . They can either be caused by an anisotropic gap structure or by a \mathbf{k} -dependence of the scattering intensity. With the help of quantitative model calculations this issue will be clarified below. It is clear that further investigation is required, especially with respect to the peak in B_{1g} symmetry at 175 cm^{-1} which has an untypical line shape for a pair-breaking peak. It has a width of only 17 cm^{-1} and does not show the typical decay at higher energies [142, 143, 175].

The main focus of this analysis will be placed on the B_{1g} feature at 140 cm^{-1} , which is by far the narrowest peak having a width of 7 cm^{-1} , close to the resolution limit, and pure B_{1g} symmetry. If the assumption of the gap edge being at 155 cm^{-1} is correct, this mode lies inside the gap. As there are no other states inside the gap to scatter from at $T = 0$, it is not surprising that the lifetime of this mode is high and thus the linewidth is small.

Following the considerations of the previous chapters the data are consistent with the scenario of an s -wave ground state ($2\Delta_{\min} \approx 155\text{ cm}^{-1}$) and a d -wave BS mode [43, 45–47, 147, 162] at 140 cm^{-1} . This set of measurements provides clear evidence for the $d_{x^2-y^2}$ character (i.e. appearance in B_{1g}) of the mode. Hence the origin of such a mode is a subdominant $d_{x^2-y^2}$ interaction.

5.1.2 Temperature dependence

In addition to the symmetry analysis, the temperature dependence may furnish further support for the identification of the B_{1g} peaks at 140 and 175 cm^{-1} with a BS mode and a pair-breaking peak, respectively.

To this end, spectra at various temperatures between 8 K and 46 K were obtained in B_{1g} symmetry as compiled in Fig. 5.2. Fig. 5.2(a) shows the temperature evolution of the spectra in B_{1g} symmetry. To extract the peak positions, the electron-hole continuum [55, 176, 177] in the vicinity of the peaks is approximated by a smooth function, as depicted by the black line in Fig. 5.2(b). A subtraction of the continuum leaves the bare peaks which were then fitted by two Lorentz functions, yielding the peak frequency, the width and an estimate for the error. The small red and blue lines in Fig. 5.2(a) illustrate the peak positions. The grey shaded areas indicate the error range and the dashed lines the peak positions at $T = 8\text{ K}$. The inset compiles all peak positions, normalized to the energy at the lowest temperature.

The temperature dependences of the two peaks are found to be different. The narrow peak (red) softens at higher temperature, whereas the high-energy peak (blue) depends only weakly on temperature up to $0.7T_c$. This substantiates one part of the assumption as it indicates that the peaks emerge from two distinct effects.

It must be checked however, if the observed temperature dependence is consistent with the interpretation of these effects as a BS mode and a pair-breaking peak, as indicated in Fig. 5.2. At first glance, the temperature evolution of a pair-breaking peak is assumed to follow the BCS prediction for the gap size $\Delta(T)$ [4]. However, there are various reasons for a deviation from the BCS behavior.

An Eliashberg calculation for $\text{SmFeAsO}_{0.8}\text{F}_{0.2}$ and $\text{Ba}_{0.6}\text{K}_{0.4}\text{Fe}_2\text{As}_2$ [178] in the

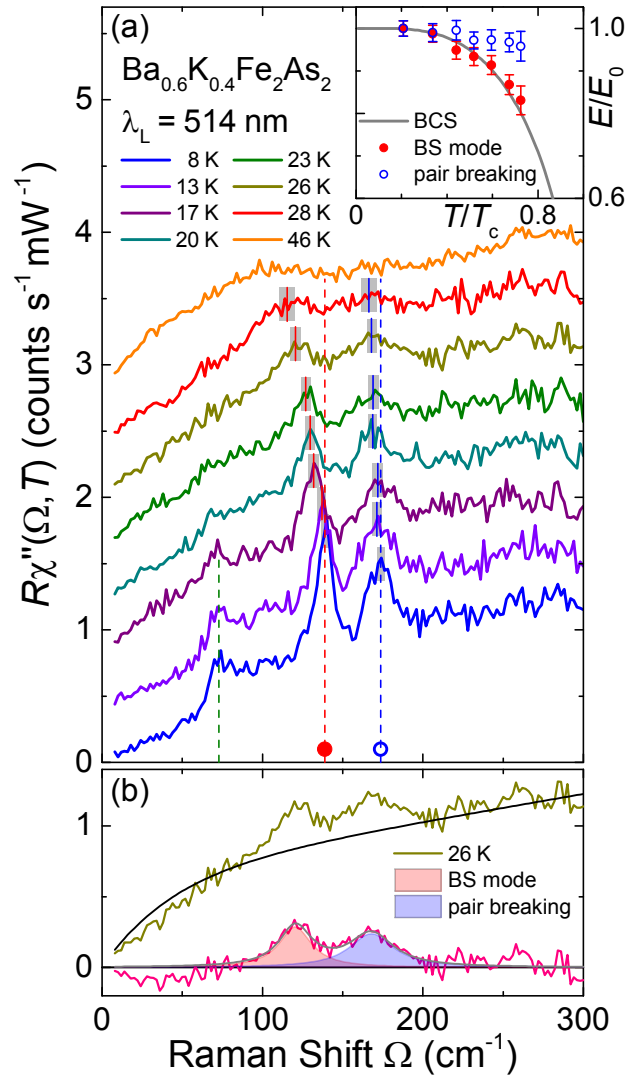


Figure 5.2: Temperature dependence of the peaks in B_{1g} symmetry. (a) shows spectra taken at temperatures ranging from 8 to 46 K, stacked above each other with an offset of 0.4. The peak energies of the BS mode (full red dots) and the pair-breaking peak (open blue dots) are compiled in the inset. (b) They are extracted by a fit with two Lorentzian curves after subtraction of a phenomenological electronic continuum (black curve). The red and blue shaded areas indicate the contribution from the BS mode and the pair-breaking peak, respectively.

strong coupling limit showed that the gap itself stays nearly constant for a wide temperature range until it suddenly drops to 0 close to T_c . The Eliashberg calculation accounts for the renormalization effects appearing in the case of strong coupling by self-energy corrected Green's functions.

Another approach includes renormalization effects by introducing a temperature and energy-dependent scattering rate $\Gamma(T, \Omega)$ [148, 149, 179–181] enabling the treatment of strong coupling effects as well as impurity scattering. The Raman spectra get influenced in two ways: (i) The 2Δ singularity is chopped off. However, this effect is insufficient to suppress the pair-breaking peak for all temperatures up to 28 K [Fig. 5.2(a)]. (ii) The peak position can no longer be associated with twice the single-particle gap (which follows the BCS temperature dependence). Now, the temperature variation of the peak position deviates from a BCS-like prediction towards a weaker temperature dependence of the pair-breaking peak [148, 149, 179]. In contrast to that, though a bit counterintuitive, the BS mode is expected to follow the single-particle gap, i.e. has a BCS temperature dependence [45] if, as usual, the subdominant coupling parameters are independent of temperature and energy.

Following these considerations, the weakly temperature-dependent peak is the pair-breaking peak, whereas the other peak with a BCS-like temperature evolution is unlikely to have the same origin. This analysis consolidates the assumption about the nature of these two peaks and is another piece of evidence for the collective character of the narrow mode thus supporting the identification as a BS mode. Yet the unusual shape of the pair-breaking peak remains unexplained, especially the missing $1/\Omega^2$ tail expected from the relation $\chi''(\Omega) \propto 1/(\Omega\sqrt{\Omega^2 - 4\Delta^2})$ [123].

5.1.3 Phenomenological model

The shape anomalies of the pair-breaking peak in the presence of BS modes can be accounted for in a phenomenological description [46, 48, 162]. In addition, the band and momentum dependence of the gap $\Delta(\mathbf{k})$ and indications of the anisotropy of the pairing potential $V_{\mathbf{k},\mathbf{k}'}$ can be derived thereof. More specifically, those components of $V_{\mathbf{k},\mathbf{k}'}$ can be extracted which the BS modes can be traced back to. Since the BS modes reflect subleading pairing instabilities beyond the winning ground state the components will be labeled $V_{\mathbf{k},\mathbf{k}'}^{\text{sub}}$. To decompose $V_{\mathbf{k},\mathbf{k}'}^{\text{sub}}$ into symmetries, the eigenvalues λ_i and eigenvectors $g_i(\mathbf{k})$ are determined. λ_i and $g_i(\mathbf{k})$ correspond to the pairing strength and form factor of channel i . The symmetry of channel i is described by the momentum dependence of the form factor. In the present case, $g(\mathbf{k})$ of the subdominant channel has B_{1g} symmetry.

The quantities $\Delta(\mathbf{k})$, $g(\mathbf{k})$, and λ shall now be obtained based on the tight-binding 5-band model [48] outlined in the previous chapter. To illustrate the derived quantities in \mathbf{k} -space, the 1 Fe Brillouin zone is used, unless stated otherwise. The symmetries A_{1g} , A_{2g} , B_{1g} , and B_{2g} are thus defined with respect to the 1 Fe BZ, e.g. B_{1g} has nodes along the diagonals of the $k_x k_y$ plane. However, as the 1 Fe unit cell does not account for the total crystal symmetry, especially the As superstructure [34], the 2 Fe BZ is the adequate zone to describe the additional translational symmetry by the vector (π, π, π) [48].

This vector is shown as dark grey arrow in Fig. 5.3(c), embedded in the 1 Fe BZ. The figure illustrates the Raman vertices $\gamma_n^\mu(\mathbf{k})$ for different symmetries $\mu \in \{A_{1g}, B_{2g}, B_{1g}\}$ and bands n . The momentum-dependent and symmetry-resolved vertices are a measure for the Raman scattering intensity, originating from a certain \mathbf{k} -point in the respective symmetry. They are calculated using the effective mass approximation [55, 147] (in the proper 2 Fe cell),

$$\gamma_n^{A_{1g}}(\mathbf{k}) = \frac{1}{2} \left\{ \frac{\partial^2 E_n(\mathbf{k})}{\partial k_x \partial k_x} + \frac{\partial^2 E_n(\mathbf{k})}{\partial k_y \partial k_y} \right\}, \quad (5.1)$$

$$\gamma_n^{B_{2g}}(\mathbf{k}) = \frac{\partial^2 E_n(\mathbf{k})}{\partial k_x \partial k_y}, \quad (5.2)$$

$$\gamma_n^{B_{1g}}(\mathbf{k}) = \frac{1}{2} \left\{ \frac{\partial^2 E_n(\mathbf{k})}{\partial k_x \partial k_x} - \frac{\partial^2 E_n(\mathbf{k})}{\partial k_y \partial k_y} \right\}, \quad (5.3)$$

where E_n is the energy of band n . In practice, the evaluated \mathbf{k} -points are limited to the Fermi surface of band n . Justification for using the effective mass approximation yielding Eqs. 5.1, 5.3, and 5.2 is presented in App. 7.2. The resulting Raman vertices are compiled in Fig. 5.3. A closer look reveals that a contribution from every band can be expected in A_{1g} symmetry. For B_{2g} and B_{1g} symmetry only the outer electron bands will give a substantial contribution to the Raman response which will be particularly helpful to interpret the B_{1g} spectrum.

In the absence of a subdominant coupling, the response will be built up by the superconducting gaps at the various Fermi surfaces, weighted by the squared Raman vertex. The Raman response $\chi''(\mathbf{q} = 0, \Omega) = \text{Im}\chi(\mathbf{q} = 0, \Omega)$ is calculated using the bare bubble approximation at $T = 0$ [123, 147]

$$\chi(\Omega) = \sum_n \sum_{\mathbf{k}} \gamma_n^2(\mathbf{k}) \lambda_n(\mathbf{k}, \Omega) \quad (5.4)$$

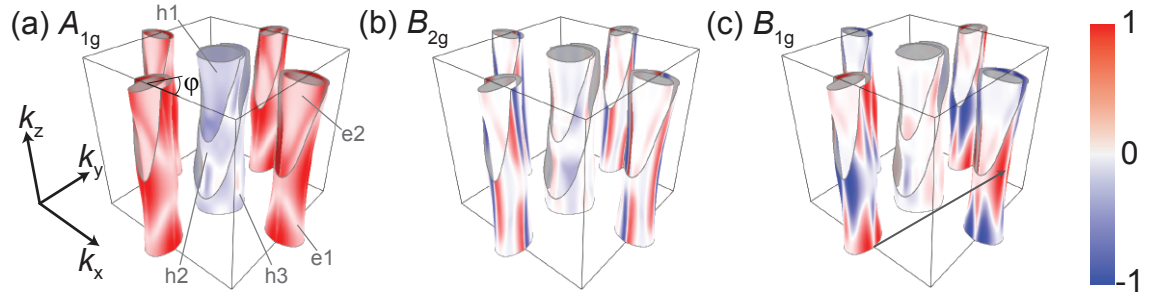


Figure 5.3: Raman vertices of A_{1g} , B_{2g} , and B_{1g} symmetry as derived from Eqs. 5.1 - 5.3. The thin black lines depict the edges of the 1 Fe BZ with the Γ -point in the center. The vertex on each Fermi surface $n \in \{h1, h2, h3, e1, e2\}$ is illustrated with a colorscale showing positive (red) and negative (blue) regions, the brightness of the color scales with the magnitude of the vertex. In B_{2g} and B_{1g} symmetry the vertex on the outer electron band e1 is by far the largest. The dark grey arrow in (c) shows the (π, π, π) translational symmetry, responsible for the sign change of the B_{1g} vertex along k_z .

with the Tsuneto function λ_n [182]. This is valid for B_{1g} and B_{2g} symmetry, where the response on the FS n is given by

$$\chi_n''(\Omega) = 4\pi \left\langle \frac{\gamma_n^2(\mathbf{k}) |2\Delta_n(\mathbf{k})|^2}{\Omega \sqrt{\Omega^2 - |2\Delta_n(\mathbf{k})|^2}} \right\rangle \quad (5.5)$$

for $\Omega > |2\Delta_n(\mathbf{k})|$ and $\chi_n''(\Omega) = 0$ for $\Omega < |2\Delta_n(\mathbf{k})|$ with $\langle \dots \rangle$ denoting the individual FS average. The total response is a simple summation $\chi''(\Omega) = \sum_n \chi_n''(\Omega)$. The susceptibility of the totally symmetric A_{1g} symmetry is affected by the Coulomb interaction which introduces a multi-band screening term [143, 183–185] renormalizing the susceptibility to

$$\chi^{A_{1g}}(\Omega) = \sum_n \sum_{\mathbf{k}} \gamma_n^2(\mathbf{k}) \lambda_n(\mathbf{k}, \Omega) - \frac{\sum_n \sum_{\mathbf{k}} \gamma_n(\mathbf{k}) \lambda_n(\mathbf{k}, \Omega)}{\sum_n \sum_{\mathbf{k}} \lambda_n(\mathbf{k}, \Omega)} \quad (5.6)$$

as derived in Chapter 4.

With the response known from the experiment and the Raman vertices derived from the rigid band model, an iterative fitting procedure is applied to determine the gaps $\Delta_n(\mathbf{k})$. Using a suitable starting guess for the gaps, the equations are evaluated numerically and are compared with the spectra, then the gaps are varied until a satisfactory agreement is obtained. This procedure will exclusively be performed for the A_{1g} and B_{2g} symmetries, as B_{1g} is expected to deviate substantially due to the subdominant coupling.

The gap on the outer electron band e1 [defined in Fig. 5.3(a)] will be discussed in

detail to illustrate the procedure. The response of this gap is expected to dominate the B_{2g} spectrum, as the B_{2g} Raman vertex on band e1, γ_{e1}^2 , is considerably larger than the vertices on all other bands [see Fig. 5.3 (b)]. The spectrum shows that the gap opens at $2\Delta_{\min} \approx 155 \text{ cm}^{-1}$, then the intensity rises monotonically and reaches its maximum at $2\Delta_{\max} \approx 210 \text{ cm}^{-1}$. A slope like this, covering a range of about 50 cm^{-1} , can only be observed if the Raman vertex is vanishingly small around $2\Delta_{\min}$. Otherwise, e.g. for a constant Raman vertex as shown in Fig. 4.5(c) the pair-breaking response would exhibit a step at $\Omega = 2\Delta_{\min}$. As there is no step observed the minimum gap must be located in areas where γ_{e1}^2 is small [white in Fig. 5.3(b)]. Following the crystal symmetry a fourfold symmetry of the gap around the outer electron band is assumed which results in a \mathbf{k} -dependent gap as indicated in Fig. 5.4. This contributes to the B_{2g} spectrum as illustrated in Fig. 5.5(b) and (e). The spectrum is dominated by the pair-breaking response (light blue) of the outer electron pocket e1.

Table 5.1: Gap energies (meV) obtained by the model calculation for bands h1-e2. The ARPES results are from Ref.[75], with the same value for the hole bands h1 and h2, as they were not distinguishable in the ARPES measurement.

Band	$\Delta_{\min}^{\text{Raman}}$	$\Delta_{\max}^{\text{Raman}}$	$\Delta_{\text{av}}^{\text{ARPES}}$
h1	9.5	12.1	12.3 ± 0.6
h2	10.4	15.9	12.3 ± 0.6
h3	4.2	5.0	5.8 ± 0.8
e1	10.3	13.3	12.2 ± 0.3
e2	10.8	11.4	11.4 ± 0.5

To obtain the gaps on the other pockets, and their contribution to the response, this analysis is continued with initial guesses from ARPES measurements [75, 76, 83, 169]. For the hole bands they suggest a k_z -dependence [80, 186] of the gaps rather than an angular variation. Eventually a gap on every band is defined, all of them being compiled in Fig. 5.4. The model parameters and \mathbf{k} -dependences of the gaps are summarized in Table 5.1, along with ARPES results. The functional form of the gaps on the hole bands is $\Delta_{h_i}(k_z) = \Delta_{h_i}^+ + \Delta_{h_i}^- \cos(k_z)$ with a k_z -dispersion, whereas the gaps on the electron bands $\Delta_{e_i}(\varphi) = \Delta_{e_i}^+ + \Delta_{e_i}^- \cos(4\varphi)$ vary by the azimuthal angle φ . Here the average $\Delta^+ = (\Delta_{\min}^{\text{Raman}} + \Delta_{\max}^{\text{Raman}})/2$ and the variation $\Delta^- = (\Delta_{\min}^{\text{Raman}} - \Delta_{\max}^{\text{Raman}})/2$ are used.

One finds that the gap magnitudes are in agreement with the photoemission measurements. The gap anisotropy in the Raman experiments is larger than in the

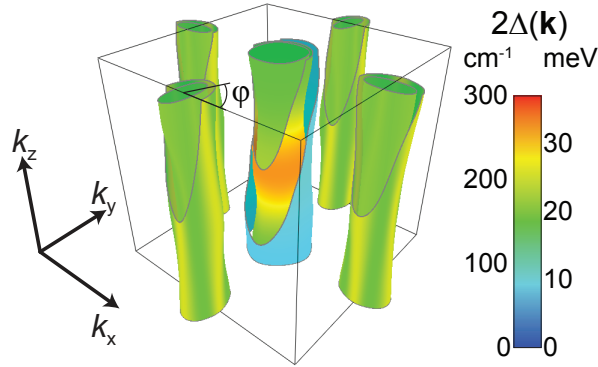


Figure 5.4: Gap structure $2\Delta(\mathbf{k})$ as a false color plot. The gap magnitude and anisotropy is compiled here for every Fermi surface. The gaps on the hole bands have a k_z dispersion, those on the electron bands a variation along the azimuthal angle φ .

photoemission though still small on an absolute scale. All the magnitudes are in a similar range, except for the gap on the outer hole band h3.

The results of the phenomenological Raman response using the vertices dictated by the band structure (Fig. 5.3 and the momentum dependence of the gap (Fig. 5.4) is shown in Fig. 5.5. The black lines in (a) and (b) are the response as obtained from Eq. (5.5) and (5.6) with the parameters given in Table 5.1. A comparison with the difference spectra [Fig. 5.1(e)] is the best approximation here as the weak-coupling model does not account for any quasi-particle interaction leading, among other things, to the extended electron-hole continuum. Negative intensities of $\Delta\chi''$ below the gap edge are a consequence of the gap. Thus the negative intensity is disregarded.

For the black curves one overall scaling factor is naturally required for all symmetries. In addition a relative scaling factor is used per symmetry. They are 0.23 for A_{1g} and 0.67 for B_{2g} with respect to 1 for B_{1g} . Then, for the most prominent peaks an agreement of the model calculations with the experiment is observed. The spectra in A_{1g} and B_{2g} symmetry are reproduced very accurately. Now Eq. 5.5 will be applied to calculate the response for B_{1g} symmetry which has not been included for the determination of the gaps yet. This yields the grey line in Fig. 5.5(c) and, as shown in (f), mainly the gap on band e1 contributes. However, the agreement between theory and experiment is unsatisfactory.

In the following the subdominant coupling will be considered with the goal to improve the agreement. Doing so results in a shift of spectral weight out of the pair-breaking peak (grey area) into the BS mode. The redistribution of intensity is

described by [46]

$$\delta\chi''_{B_{1g}}(\Omega) = \frac{8}{\Omega^2} \text{Im} \left\{ \frac{\langle \gamma^{B_{1g}}(\mathbf{k}) g(\mathbf{k}) \Delta_{e1}(\mathbf{k}) \bar{P}(\tilde{\Omega}_{\mathbf{k}}) \rangle^2}{(\lambda_d^{-1} - \lambda_s^{-1}) - \langle g^2(\mathbf{k}) \bar{P}(\tilde{\Omega}_{\mathbf{k}}) \rangle} \right\}. \quad (5.7)$$

which yields the total B_{1g} response $\chi''_{\text{tot}, B_{1g}} = \chi''_{B_{1g}} + \delta\chi''_{B_{1g}}$. $\bar{P}(\tilde{\Omega}_{\mathbf{k}})$ is the response kernel with $\tilde{\Omega}_{\mathbf{k}} = \Omega/2\Delta_{e1}(\mathbf{k})$ such that

$$\bar{P}(\tilde{\Omega}_{\mathbf{k}}) = \begin{cases} \frac{\tilde{\Omega}_{\mathbf{k}}}{\sqrt{1-\tilde{\Omega}_{\mathbf{k}}^2}} \arcsin(\tilde{\Omega}_{\mathbf{k}}), & |\tilde{\Omega}_{\mathbf{k}}| < 1 \\ \frac{\tilde{\Omega}_{\mathbf{k}}}{\sqrt{\tilde{\Omega}_{\mathbf{k}}^2-1}} \left[\ln \left(|\tilde{\Omega}_{\mathbf{k}}| - \sqrt{\tilde{\Omega}_{\mathbf{k}}^2-1} \right) + i\frac{\pi}{2} \right], & |\tilde{\Omega}_{\mathbf{k}}| > 1. \end{cases} \quad (5.8)$$

The dominant parameter λ_s is attributed to the superconducting ground state. The ground state can either be an s^{++} or s^\pm wave state [see Fig. 2.10(b) and (c), respectively] which cannot be distinguished by light scattering experiments. In any case, the gap has A_{1g} symmetry but remains observable in other symmetries as well because the Raman vertex and the gap enter the response quadratically. This is different for the BS mode. The mode originates from the subdominant coupling of the d -wave interaction with the coupling strength λ_d . Its \mathbf{k} -dependence is described by the form factor $g(\mathbf{k})$. For the BS mode the unique chance arises to determine the symmetry (phase) of the subdominant coupling. The numerator in Eq. 5.7 determines the selection rule. To get a finite Fermi surface average, the symmetry of $\gamma(\mathbf{k})g(\mathbf{k})\Delta_{e1}(\mathbf{k})\bar{P}(\tilde{\Omega}_{\mathbf{k}})$ must contain a totally symmetric A_{1g} contribution to avoid total cancellation. $\gamma(\mathbf{k})$ has B_{1g} symmetry, $\Delta_{e1}(\mathbf{k})\bar{P}(\tilde{\Omega}_{\mathbf{k}})$ transforms as A_{1g} . Hence $g(\mathbf{k})$ must have B_{1g} symmetry. Since $\gamma(\mathbf{k})$ highlights the outer electron pocket the subdominant interaction having B_{1g} symmetry acts on the outer electron band $e1$, generating a BS mode.

The position of this mode is determined by the root in the denominator generating a pole in $\delta\chi''$. Assuming λ_s to be close to 1, the ratios of the coupling strengths λ_d/λ_s can be estimated to be as large as 0.6. This ratio λ_d/λ_s and the \mathbf{k} -dependence $g(\mathbf{k})$ were determined in an iterative way similar to the extraction of the gap values. It turns out that the subdominant interaction is strongest close to those momenta, where the gap maxima of the s -wave ground state are located. In these regions it resembles the \mathbf{k} -dependence of $\gamma(\mathbf{k})$. So except for the diagonal direction, where $g(\mathbf{k})$ vanishes, $g(\mathbf{k}) \propto \gamma(\mathbf{k})$. This momentum dependence of $g(\mathbf{k})$ is a result of the complex interrelation of $\gamma(\mathbf{k})$ and $g(\mathbf{k})$. For nearly constant $g(\mathbf{k})$ the FS average of

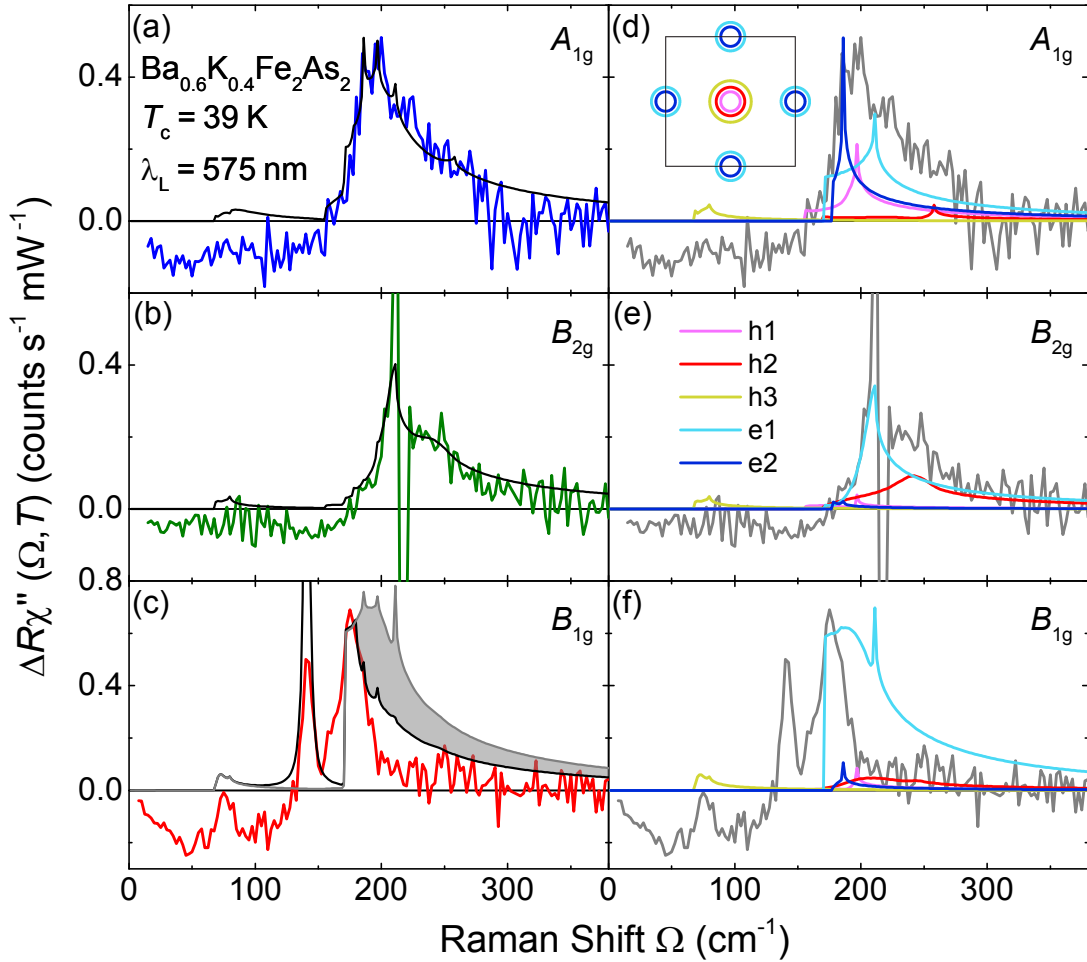


Figure 5.5: Comparison of the model calculations with the difference spectra. (a,b) The black curves in A_{1g} and B_{2g} symmetry are the calculated Raman response functions. (c) The grey curve shows the B_{1g} response generated solely by pair breaking, whereas the black curve shows the response after switching on the subdominant interaction. Spectral weight from the pair-breaking peak (grey shaded area) is shifted into the BS mode. (d-f) show the measured spectra in grey with the response calculated separately for each band. The colors indicate the bands as illustrated in the inset of (d). There is no screening applied in the calculation shown in (d) and no subdominant interaction included in (f). Note the dominance of the contribution from e1 (light blue) in (e) and (f).

$\gamma(\mathbf{k})g(\mathbf{k})$ would cancel and the BS mode would not appear.

$g(\mathbf{k})$ is displayed in Fig. 5.6. The comparison with Fig. 5.4 shows immediately that the subdominant coupling drains spectral weight from the regions close to $2\Delta_{e1}^{\max}$ but rather than $2\Delta_{e1}^{\min}$. This central result of the analysis clearly indicates a competition of the subdominant pairing with the dominant one for certain regions of the Fermi surface.

To derive $V_{\mathbf{k},\mathbf{k}'}^{\text{sub}}$ from this analysis, it is necessary to determine \mathbf{k} and \mathbf{k}' , which give

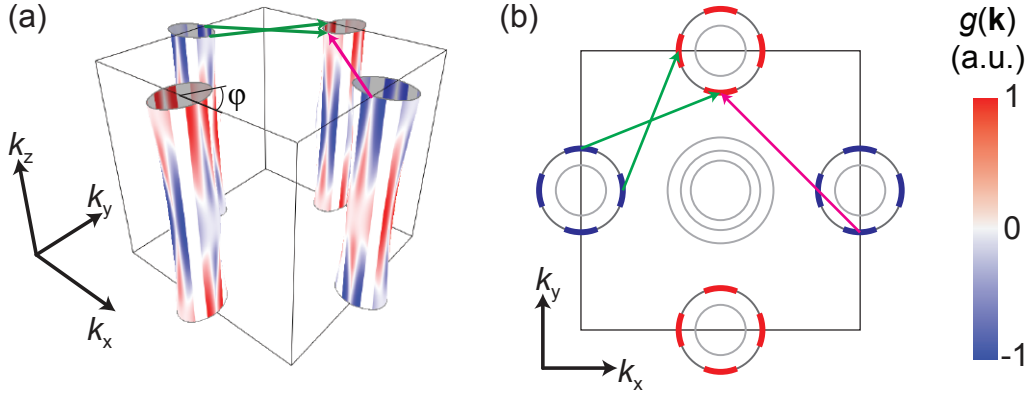


Figure 5.6: The structure of the subdominant coupling $g(\mathbf{k})$ on the outer electron band. (a) The sign change along k_z is a consequence of the (π, π, π) translational symmetry. Two possible scattering scenarios are depicted. The corresponding vectors are shown in green for one scenario and pink for the other. They act between every pair of neighboring Fermi surface sheets but are shown just for one pair here. (b) Qualitative momentum structure of $g(\mathbf{k})$.

the initial and final momentum of a scattering process. Next to an intra-band interaction, where \mathbf{k} and \mathbf{k}' are located in the same pocket, two suggestions are proposed for possible inter-band interaction vectors $\mathbf{k}' - \mathbf{k}$ found very commonly in literature [48, 49]. The green and pink arrows show these vectors exemplarily. The pink one is close to the $(\pi, \pi, 0)$ vector. The origin and tip of this vector are simultaneously experiencing an altering (between vanishing and maximal $g(\mathbf{k})$) interaction potential on their way around the outer electron pocket. The green ones on the other hand connect those parts of the FS, where $g(\mathbf{k})$ is maximal.

Although this question cannot be clarified ultimately, a conclusion on the interaction can be drawn that both vectors have in common: They represent an inter-band interaction with a sign change between the Fermi surfaces connected by the interaction vectors.

5.1.4 Discussion

The experimental results narrow down the types of interactions (as outlined in Fig. 2.11). Here, the resulting constraints are discussed before other proposals for collective modes [155, 161, 163, 187] are summarized.

Interactions

In the superconducting state, a nearly isotropic and full gap was found on every pocket. Hence the ground state either has s^{++} or s^\pm symmetry, a nodal structure is excluded.

A phonon-driven mechanism would yield the correct ground state (s^{++}), however, the strength of the subdominant $d_{x^2-y^2}$ pairing interaction is negligible in this case [113–115] and thus cannot reproduce the BS mode as observed. However, a combination of a phonon-driven ground state and a subdominant interaction e.g. generated by spin fluctuations remains possible.

An AFM exchange interaction yields an s^\pm ground state in the case of $J_1 \ll J_2$. A subdominant $d_{x^2-y^2}$ interaction is present here as well but too weak to yield a ratio of $\lambda_d/\lambda_s \approx 0.6$ [88]. In addition, inelastic neutron scattering experiments yield $J_1 \gg J_2$ for BaFe₂As₂ [91]. In this branch the present Raman experiments are already in conflict with the ground state.

In the case of fluctuation mediated pairing, a full gap can be generated in the spin, charge and (antiferro) orbital channel. As the ferro-orbital and the intra-band charge channel acquire a $d_{x^2-y^2}$ form factor, also a subdominant interaction can be produced by these three channels. Further insight is gained from the momentum dependence of $g(\mathbf{k})$ as depicted in Fig. 5.6 and the possible interaction vectors. For the (subdominant) B_{1g} -symmetric pairing, Kuroki and coworkers [49] argue that in the case of spin-fluctuation mediated pairing the orbital matching of the $d_{x^2-y^2}$ orbital contribution between two neighboring electron pockets becomes crucial and quenches the simple $(\pi, \pi, 0)$ nesting [50, 51, 78, 111, 188]. The $d_{x^2-y^2}$ orbital contribution of the electron pockets is maximal along k_x and k_y but small along the diagonal directions $\varphi \in \{45^\circ, 135^\circ, 225^\circ, 315^\circ\}$ defining the momenta of strong and weak interactions, respectively. This momentum dependence qualitatively coincides with that of $g(\mathbf{k})$. The corresponding nesting vectors are the intersecting ones connecting two neighboring electron pockets (green arrows in Fig. 5.6).

This provides a consistent explanation of the Raman experiments in the picture of spin-fluctuation mediated pairing: The superconducting ground state of s^\pm sym-

metry is generated by repulsive spin fluctuations acting between the electron and hole pockets with the nesting vectors $(\pm\pi, 0, 0)$ and $(0, \pm\pi, 0)$. The subdominant interaction is of B_{1g} symmetry as generated by spin-fluctuation exchange between neighboring electron pockets with the interacting nesting vectors [49, 51, 77, 90, 94].

Leggett modes

A recent theoretical study [189] shows, that Leggett modes with A_{1g} symmetry contribute to the Raman response of IBSs. In the original theory by A. Leggett [187] a collective phase mode is discussed. In the simplest case of a 2-band model, intra-band interactions can generate the superconducting ground state having gaps $\Delta^{e,h} = \Delta_0^{e,h} e^{i\varphi^{e,h}}$ on the electron and hole bands e and h. If an inter-band interaction is present, an oscillation of the relative phase $\varphi^e - \varphi^h$ can appear, resulting in a Josephson-like oscillation, the Leggett mode [187, 190–193].

In the special case of the IBSs, where the Raman vertices of hole and electron-pockets change sign in A_{1g} symmetry, a Leggett mode affects the A_{1g} -symmetric Raman response [189]. Here, the approximation of a two-band model with parabolic bands having the same density of states, similar gaps $|\Delta^e| = |\Delta^h|$, and constant Raman vertices $\gamma^e = -\gamma^h$ in A_{1g} symmetry is made. If the Leggett mode is not considered, the A_{1g} Raman response is expected to be the typical pair-breaking peak at $2\Delta^{e,h}$ [Fig. 4.5(b)]. If Leggett modes are included two cases must be considered: Intra-band dominated pairing and inter-band dominated pairing. In the first case, the pair-breaking peak disappears completely (see Fig. 2 of Ref. [189]) and a narrow Leggett mode appears below twice the gap edge. Such a mode is not observed in the present analysis. In the second case, the pair-breaking peak is replaced by a Leggett mode at $2\Delta^{e,h}$, with a response that is similar to that of pair breaking. This is another possibility that could explain the response in A_{1g} symmetry suggesting inter-band dominated pairing in the ground state [189]. As the B_{2g} and B_{1g} spectra are unaffected by Leggett modes with A_{1g} symmetry, the central results of the analysis remain valid.

The particle-hole channel

In general, the particle-hole channel must also be considered for the BS mode in B_{1g} symmetry. The theory of Scalapino and Devereaux [46] accounts for the subdominant interaction to act in the particle-particle (p-p) channel only. There are theories that include the particle-hole (p-h) channel as well. The theory by Khodas and coworkers (Ref. [155]) will be discussed in greater detail here.

They consider the simplified case [194] of a two-band model with couplings in the s - and d -wave channel. As they examine vertex corrections both in the p-p and p-h channel they also have to include a mixing term between p-p and p-h channel. This results in a renormalized Raman susceptibility. The theory expects two distinct modes to appear in Raman scattering experiments, one p-p like, the other p-h like. They further argue that only one in-gap mode exists if the mixing between the channels is high. This is the case when the term $\langle GF \rangle$, i.e. the term that interchanges p-p and p-h channels, is large, with G and F being the normal and anomalous Green's functions, respectively. The relevance of the mixing term can be derived from the \mathbf{k} -dependence of the gap, which enters F and thus GF linearly, see Eq. 4.7 and 4.8. In the case of nearly isotropic and sign-preserving gaps on the electron-bands $\langle GF \rangle$ is finite and the inclusion of the p-h channel results in a single in-gap mode of B_{1g} symmetry. Further calculations show that this mode would then have a combined p-p and p-h character and indicate that even the inclusion of the p-h channel does not alter the results obtained above.

Open problems

Up to this point, the two most pronounced B_{1g} features were explained. However, the third peak at 80 cm^{-1} has not been addressed in detail so far. The spectral weight of this peak is largest in B_{1g} symmetry, in A_{1g} only a weak hump with 10% of the spectral weight is visible. The response in B_{2g} symmetry shows no clear feature at all as visible in Fig. 5.1. This peak was assigned to the pair-breaking peak originating from the gap on the outer hole pocket, as suggested by ARPES experiments. However, the phenomenological model yields a peak in B_{1g} symmetry with a spectral weight that is by far too small, see Fig. 5.5, making another origin more likely. Raman experiments on further doping levels in section 5.2 provide evidence for another BS mode of d -wave symmetry at 80 cm^{-1} with an even stronger subdominant coupling strength but less spectral weight.

Finally, the selection rules need to be addressed. In Ref. [122], Hirschfeld points out that the bands involved in the generation of the BS mode are hard to identify within a complex multi-band system as here. From the calculation of the Raman vertices (Fig. 5.3) it is clear that in BKFA only the outer electron pockets are projected out in B_{1g} symmetry. While the vertices allow for the identification of the band where the observed features arise from, their momentum dependence also shows that only a fraction of the FS is projected.

5.2 Doping dependence of competing interactions in $\text{Ba}_{1-x}\text{K}_x\text{Fe}_2\text{As}_2$ ($0.22 \leq x \leq 0.70$)

In the previous part, evidence was provided for the emergence of a BS mode in optimally doped $\text{Ba}_{0.6}\text{K}_{0.4}\text{Fe}_2\text{As}_2$. It was further possible to assign and quantitatively describe the prominent features related to superconductivity [162]. This analysis shall now be extended to various doping levels to unravel the relation of the pairing interactions with the electronic band structure [50, 51, 77]. The smooth changes of the Fermi surface sheets close to optimal doping allows for a continuous tuning of the inter-band couplings λ_s and λ_d and helps gaining insight into their microscopic origin.

Furthermore, superconductivity was explored far off optimal doping, inside the SDW state at $x = 0.22$ and $x = 0.25$, and for the high doping levels $x = 0.62$ and $x = 0.70$. The highest studied doping $x = 0.70$ is close to the doping level where the electron pockets disappear completely ($x \approx 0.8$) and reemerge as hole pockets [80] as detected in KFe_2As_2 [195]. The doping and measuring temperatures are indicated in the phase diagram of Fig. 5.7. All Symmetries were measured for the respective temperatures.

First, a general overview of the spectra is presented with a focus on the superconductivity-induced features, then the more exotic states below the SDW ordering temperature are discussed. Special attention is payed to the range around optimal doping for a more quantitative analysis of the coupling channels. Finally the samples with doping concentrations of $x = 0.62$ and $x = 0.70$ are studied utilizing the results obtained from the optimally doped samples.

5.2.1 Doping dependence of the superconducting features

The doping dependence of the symmetry-resolved spectra in the normal and superconducting state are compiled in Fig. 5.8. All measurements shown here were

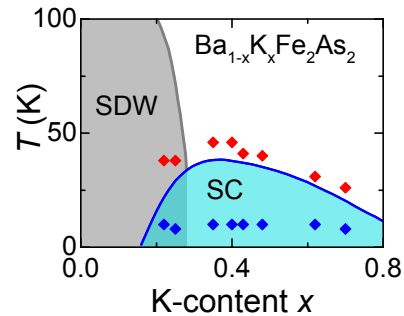


Figure 5.7: Sampling points in the phase diagram of $\text{Ba}_{1-x}\text{K}_x\text{Fe}_2\text{As}_2$. The phase diagram is adopted from Ref. [70]. For the investigation of superconductivity spectra between $x = 0.22$ and $x = 0.70$ were recorded at low temperatures in the superconducting state (blue diamonds) and in the normal state, right above T_c (red diamonds). Between approximately 0.16 and 0.28 SDW and superconductivity coexist.

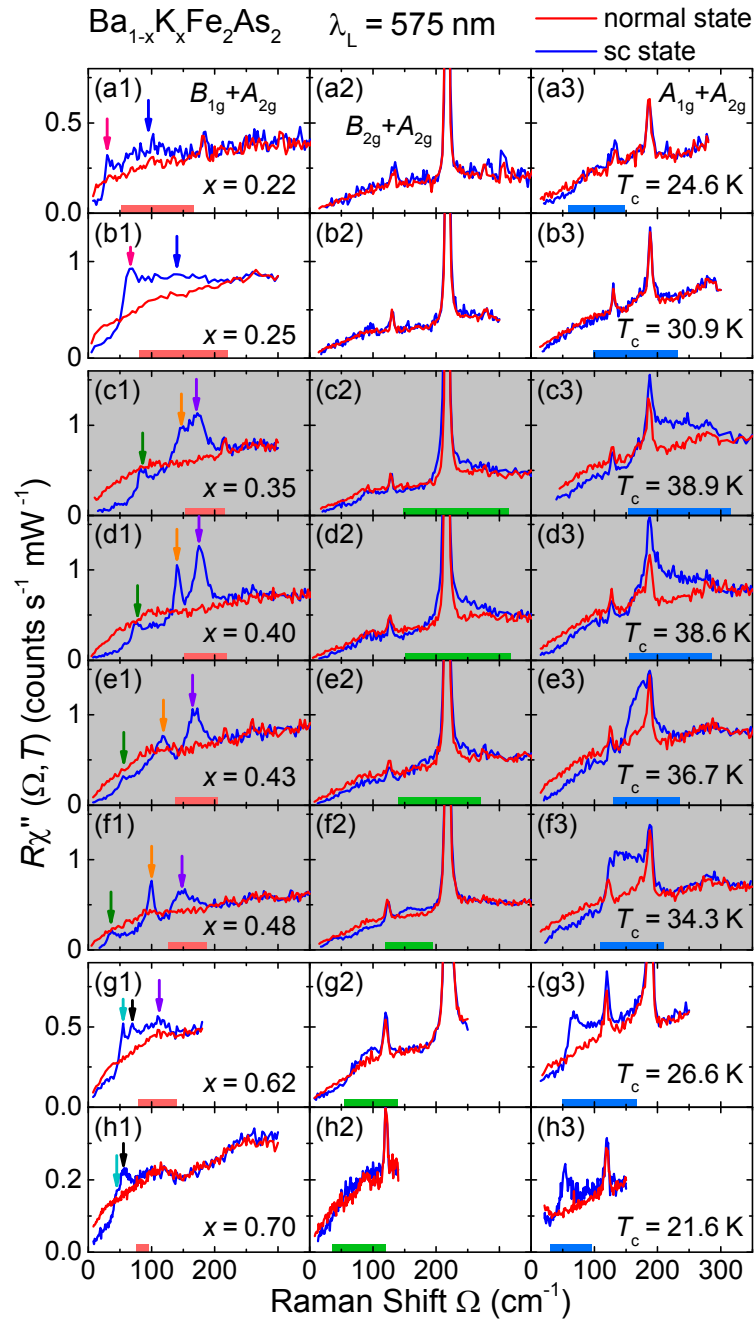


Figure 5.8: Superconducting and normal state spectra of $\text{Ba}_{1-x}\text{K}_x\text{Fe}_2\text{As}_2$ for eight doping levels $0.22 \leq x \leq 0.70$. The panels are labeled from a to h for different doping levels appended by 1, 2 and 3 for B_{1g} , B_{2g} and A_{1g} symmetry, respectively. All spectra contain a small contribution from A_{2g} symmetry (see App. 7.3). The data are split into three qualitatively different regions: (a) and (b) show the spectra inside the SDW state. (c-f) compile spectra around optimal doping and are shaded in grey. (g) and (h) show the doping levels $x = 0.62$ and $x = 0.70$. The energy ranges of the pair-breaking peaks are marked by horizontal bars at the bottom of each panel. The arrows in B_{1g} symmetry highlight the features that emerge in the superconducting state. The color code introduced here is maintained in the whole section.

performed with an excitation wavelength of 575 nm. To analyze these measurements the spectra were investigated in detail in order to extract the superconductivity-induced features and study their evolution with doping in comparison with results from Refs. [47, 124, 125, 134, 135, 155, 162, 196, 197].

As a starting point, the spectra at optimal doping ($x = 0.4$) are chosen, which were extensively studied in the previous section. The spectra of Fig. 5.8(d1-d3) are identical to those in Fig. 5.1. Three peaks are detected in B_{1g} symmetry, marked by the green, orange and purple arrow in Fig. 5.8(d1). The orange arrow identifies the BS mode, which is split off from the pair-breaking peak. The remainder of this pair-breaking peak is indicated by the purple arrow. Its spectral range from the onset of the peak to the merging point with the normal spectrum is indicated by a red bar at the bottom of the panel. The ranges for the B_{2g} and A_{1g} symmetries are indicated in green and blue in columns 2 and 3, respectively. These bars show the features at the highest energies which are located in a range around $2\Delta/k_B T_c = 7$, as compiled in Fig. 5.9. Eliminating the dependence on T_c [4] enables a comparison of the B_{1g} peak with the full range of the pair-breaking features as found in B_{2g} and A_{1g} symmetry.

The spectra close to optimal doping, in the range from $x = 0.35$ to $x = 0.48$, are qualitatively similar. All the features observed in the optimally doped compound also exist in this doping range. Especially the three peaks in B_{1g} symmetry as indicated by green, orange and purple arrows in Fig. 5.8(c1), (d1), (e1), and (f1) are clearly visible. In (c1) the BS mode overlaps with the pair-breaking peak but can still be resolved. The binding energy E_B , corresponding to the energy difference between the BS mode and the pair-breaking peak increases with doping. For $x = 0.43$ and $x = 0.48$, the pair-breaking features of all symmetries move to lower energies along with the decrease of T_c . This is accompanied by a reduction of intensity, i.e. the spectral weight of the pair-breaking peak decreases, especially for B_{1g} and B_{2g} symmetry.

This decrease continues through $x = 0.62$ and $x = 0.70$. (Note the different intensity scale in Fig. 5.8.) Here, for $x > 0.48$, the B_{1g} response is qualitatively different from that around optimal doping. There are still three peaks at $x = 0.62$ but the monotonic decrease of the first peak's energy (green arrow), clearly visible around optimal doping, is not continued. For $x = 0.70$ only one feature (black arrow) remains pronounced with a small shoulder (cyan arrow) at its left wing.

Below $x = 0.35$, at $x = 0.22$ and $x = 0.25$, the spectra experience another discontinuous change. Here the three-peak structure in B_{1g} symmetry turns into a

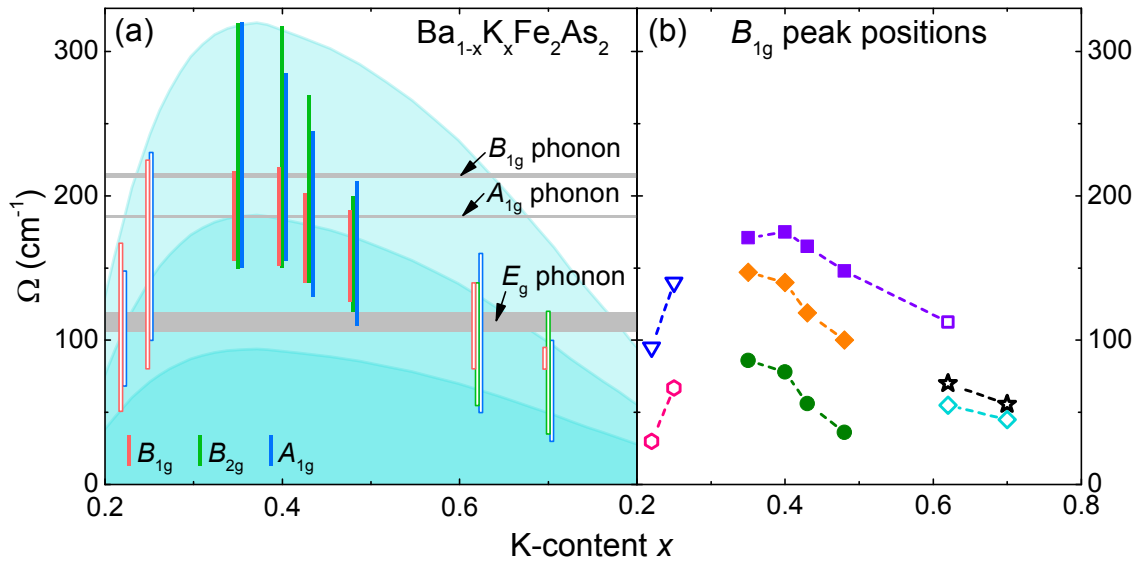


Figure 5.9: Compilation of all features in $\text{Ba}_{1-x}\text{K}_x\text{Fe}_2\text{As}_2$. (a) shows the energy range where pair breaking occurs, illustrated by vertical bars in B_{1g} (red), B_{2g} (green) and A_{1g} (blue) symmetry. They correspond to the horizontal bars of Figure 5.8. The blue shaded areas show regions in units of $2\Delta/k_B T_c$, from 0 to 3.52 for the area at the bottom, from 3.52 to 7 for the middle one, and for 7 to 12 for the topmost area. The horizontal grey bars illustrate the energy range of the optical phonons in B_{1g} (upper bar) A_{1g} (middle bar) and E_g (lower bar) symmetry. Note that the B_{1g} Fe phonon appears in the B_{2g} symmetry of the 1 Fe unit cell. (b) compiles the peak positions in B_{1g} symmetry as marked by the arrows in Fig. 5.8. Open bars and symbols are used if the interpretation is not in analogy to the optimally doped case.

single peak (pink arrow) followed by a broad hump (blue arrow). In A_{1g} symmetry, the intensity of the pair-breaking peak decreased rapidly and in B_{2g} symmetry the spectra in the superconducting and the normal state are identical.

The investigation of the doping dependence of the spectra led to a classification into three phenomenologically different categories. Furthermore, the energy ranges of the pair-breaking peaks and the peak positions of the features in B_{1g} symmetry could be obtained. Their doping dependence is illustrated in Fig. 5.9. The vertical bars correspond to the horizontal bars of Fig. 5.8. Outside $0.35 \leq x \leq 0.48$ the interpretation is different from that around optimal doping.

As a guide to the eye, blue shaded areas are introduced which show different regions of $2\Delta/k_B T_c$. The pair-breaking peaks for $0.22 \leq x \leq 0.40$ reach up to ratios of 12 and are in agreement with other measurements [171, 172, 198–201]. This ratio progressively decreases with increasing doping. In the optimally doped range between $x = 0.35$ and $x = 0.48$, the onset energies of the pair-breaking peaks of

approximately $5k_{\text{B}}T_{\text{c}}$ coincide in B_{1g} and B_{2g} symmetry. Small discrepancies of these energies arise from the continuous rather than abrupt intensity onset which occurs in the presence of a gap anisotropy. The gradual increase entails some uncertainty in the determination of the onset energy. In spite of these complications the agreement across the symmetries is remarkable and supports the identification of the pair-breaking peaks and their onset energies on the outer electron pocket for the doping concentrations $0.35 \leq x \leq 0.48$. The energy range in B_{2g} symmetry extends to higher values than in B_{1g} symmetry, which indicates the shift of spectral weight out of the B_{1g} pair-breaking peak into the BS mode. The corresponding peak positions are illustrated in Fig. 5.9(b) and show the increase of the binding energy E_{B} from $x = 0.35$ to $x = 0.48$.

Next to the superconductivity-induced features, three Raman-active optical phonons are observed [166, 202]. Their peak positions extend over an energy range marked by the horizontal grey bars in Fig. 5.9(a) and will be analyzed in detail in Section 5.4.

5.2.2 Effects of Fermi surface reconstruction in the SDW phase

A SDW instability emerges for doping levels $x \leq 0.28$ [70]. The onset of superconductivity lies at $x = 0.16$, in between, a coexistence is expected [60, 170, 203, 204]. As introduced above, two of the samples lie in this doping range, one at $x = 0.22$, the other at $x = 0.25$. New structures appear in the spectra of this doping range. In the following, these structures are analyzed in detail in order to compare them with a model that explicitly takes into account the reconstruction of the Fermi surface [106, 205–207], that is expected to arise from the superstructure imposed by the SDW order.

The strongest structures were found to appear in B_{1g} symmetry. A single peak followed by a broad hump is observed in Fig. 5.8 (a1) and (b1) at $x = 0.22$ and $x = 0.25$, respectively. For elucidating the origin of the various peaks the temperature dependence is studied for both doping levels as shown in Fig. 5.10. (a) indicates, that the hump moves down to lower energies upon increasing the temperatures up to 15 K. This coincides with a reduction of the energy where the superconducting and normal spectra merge. In contrast to that, the peak at 31 cm^{-1} stays nearly pinned as indicated by the dashed vertical line. At this energy there is no peak in A_{1g} symmetry. At higher energies, a hump is observed in the A_{1g} spectrum at 8 K. The

yellow area marks the energy range of this hump, starting at 58 cm^{-1} and ending at about 148 cm^{-1} , where normal and superconducting spectra merge. This range completely coincides with the hump in B_{1g} symmetry. The coincidence suggests pair breaking and a highly anisotropic gap to be at the origin of this hump. The usual anisotropy parameter $r = (\Delta_{\max} - \Delta_{\min})/(\Delta_{\max} + \Delta_{\min})$ equals 0.4 here similar to what was observed by thermal transport experiments [208].

The B_{1g} spectra for $x = 0.25$ are very similar. The peak stays pinned at 67 cm^{-1} , independent of temperature. The hump in the 120 cm^{-1} range also shifts to lower energies, but this effect is weaker here. For comparing the two doping levels the energy scales are normalized to the respective T_c values. The normalization is inspired by BCS theory, that states a constant ratio $2\Delta/k_B T_c \approx 3.52$ for the weak coupling case [4]. Hence the difference spectra of both doping levels are plotted as a function of the normalized energy which reveals that the position of both the peak and the hump move downwards on reducing the doping.

These findings can now be compared to the model by Maiti *et al.* [112]. The model is based on the reconstruction of the FS in the SDW state which affects the (superconducting) gap structure in the coexisting state. A widely used interpretation of this coexistence is a phase separation in \mathbf{k} -space rather than in real space [209, 210]. In this picture the parts of the Fermi surfaces, which are well nested by the SDW vector $Q_{\text{SDW}} = (\pi, 0)$, are gapped out by the SDW gap. The remaining electrons, having momenta away from the best nesting condition, can still participate in superconductivity [106, 206]. The model calculations show that the reconstructed Fermi surfaces are sensitive to small changes of the doping. A simplified 2D band structure with a circular hole pocket in the center and elliptic electron pockets at $(\pi, 0)$ and $(0, \pi)$ is used. In the SDW state the electron pocket around $(\pi, 0)$ is back-folded onto the hole pocket encircling the Γ point by $Q_{\text{SDW}} = (\pi, 0)$ [106] thus breaking the 90° rotational symmetry. The combined pockets exhibit four degeneracy points, where the pockets intersect each other. These degeneracies are lifted by the opening of the SDW gap Δ_{SDW} , yielding band energies which are the eigenvalues of

$$\begin{pmatrix} \epsilon_1(\mathbf{k}) & M(x) \\ M(x) & \epsilon_2(\mathbf{k}) \end{pmatrix} = \begin{pmatrix} 1 - k_x^2 - k_y^2 & M(x) \\ M(x) & -1 + 0.55k_x^2 + 2k_y^2 \end{pmatrix} \quad (5.9)$$

with the energies of the original bands $\epsilon_1(\mathbf{k})$ (circular hole band) and $\epsilon_2(\mathbf{k})$ (elliptic electron band) slightly different from those used in Ref. [206]. The sizes of the original pockets vary only slowly with doping. Hence the approximation of doping independent (original) pockets is made. The SDW order parameter is tuned by

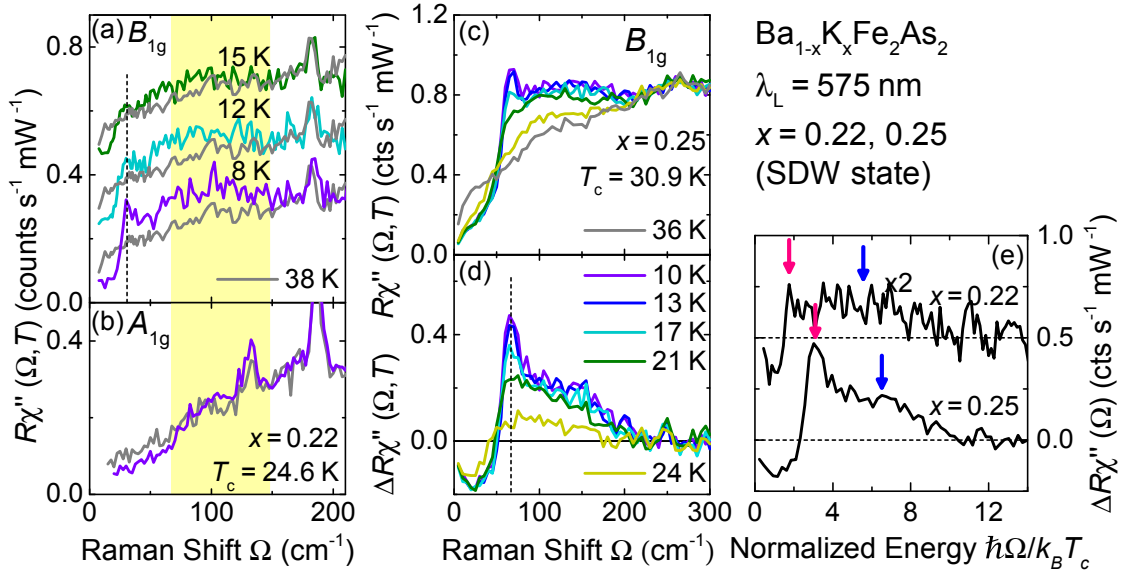


Figure 5.10: Temperature dependence of the Raman response for $\text{Ba}_{1-x}\text{K}_x\text{Fe}_2\text{As}_2$ for $x = 0.22$ and $x = 0.25$. (a) shows the temperature evolution of the spectra in B_{1g} symmetry for $x = 0.22$. The spectra are stacked by an offset of 0.2 and shown along with the spectrum in the normal state (grey) at 38 K. (b) depicts the spectra of A_{1g} symmetry. The yellow area highlights the hump in A_{1g} symmetry and is extended to (a) for comparison. (c) and (d) present B_{1g} spectra and respective difference spectra for $x = 0.25$. (e) shows a comparison of difference spectra of both doping levels stacked by $0.5 \text{ counts mW}^{-1} \text{ s}^{-1}$ with the pink arrow indicating the peak energy on an energy scale normalized to the respective T_c . The blue arrow shows the maximum of the hump.

$M(x)$. Upon reducing the doping level x the SDW gap and $M(x)$ increase rapidly along with an increase of T_{SDW} . Eventually, four new Fermi surfaces are formed, two larger ones, which are hole pockets and two smaller ones of electron character. An example is shown in Fig. 5.11(a). Right below $x \approx 0.28$ [70], a small value of the SDW gap yields new pockets, which nearly follow the original ones. Increasing values of Δ_{SDW} reduce the size of the new pockets. At a certain doping below $x = 0.28$ the small pockets disappear and at even lower doping levels also the larger ones disappear, i.e. the FS is completely gapped out by the SDW. The evolution of the FS with doping is indicated in Fig. 5.12(c-f), corresponding to the phase diagram of (a).

To calculate the superconducting gaps in the coexistence phase, Maiti and coworkers [206] started with interaction parameters yielding the proper gap structure at optimal doping, i.e. nearly isotropic gaps of s^\pm symmetry. These parameters were defined in band basis, according to the bands of the original 1 Fe BZ. Upon trans-

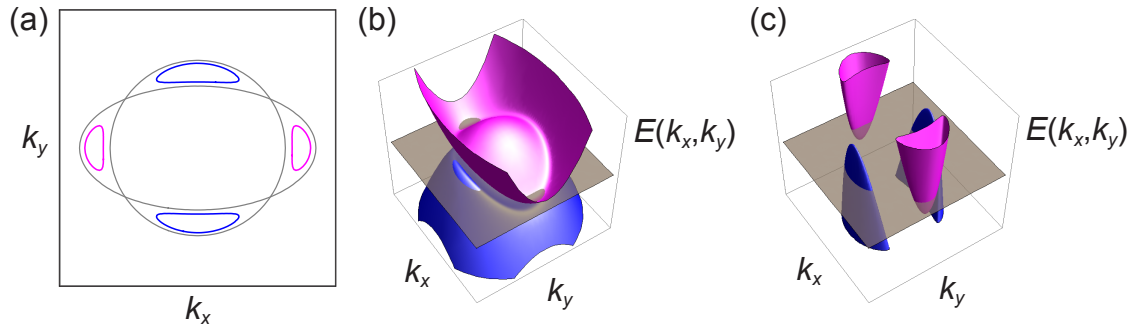


Figure 5.11: Fermi surface reconstruction in the SDW state [205, 206]. (a) shows the original pockets in grey, the circular hole pocket and the elliptical electron pocket in a BZ, which has the size of only a quarter of the original 1 Fe BZ. Due to anti crossing at the intersection points the blue and pink “banana”-shaped pockets emerge ($M = 0.281$ in Eq. 5.9). (b) shows their dispersions $E(k_x, k_y)$ which are stretched in (c) by a factor of 10 along the E -axis with the Fermi energy illustrated as the grey plane. The larger FS (blue) has a hole-like character, the smaller ones (pink) an electron-like character.

forming (folding) the bands by the procedure described above, the interaction parameters are transformed in the same way, i.e. by the same transformation matrix. One ends up with new interaction parameters defined with respect to the new bands. The larger pockets host a large gap and the smaller pockets a small gap. Both gap magnitudes merge towards the optimally doped case for very small Δ_{SDW} . For increasing Δ_{SDW} , they find a strong angular dependence of the gaps, even accidental nodes are possible. The largest gap values are found at the tips of the reconstructed Fermi surfaces [206].

A comparison of this phenomenology with the experiment makes it tempting to assign the two observed features to the two gaps of the model. The hump is associated with the superconducting gap on the larger FS, whereas the peak emerges from the superconducting gap on the smaller one. If this is correct, the peak should vanish when the small FS disappears. The hump is expected to persist down to lower doping levels, but finally also vanishes when the FS is fully gapped out. This marks the onset of superconductivity at $x = 0.16$ [70]. Hence the doping dependence was scrutinized by extrapolating the peak positions down to lower doping levels, as shown in Fig. 5.12(b). Striking evidence in favor of the results of the model calculation are found. Further clarification can be expected from studies of more doping levels, e.g. at $x = 0.15$ where the model predicts only the larger pocket to exist.

Finally, the Raman vertices of the new pockets are calculated to derive an estimate for the intensities that can be expected in the spectra for different symmetries. The effective mass approximation according to Eqs. 5.1, 5.3, and 5.2 is used. The

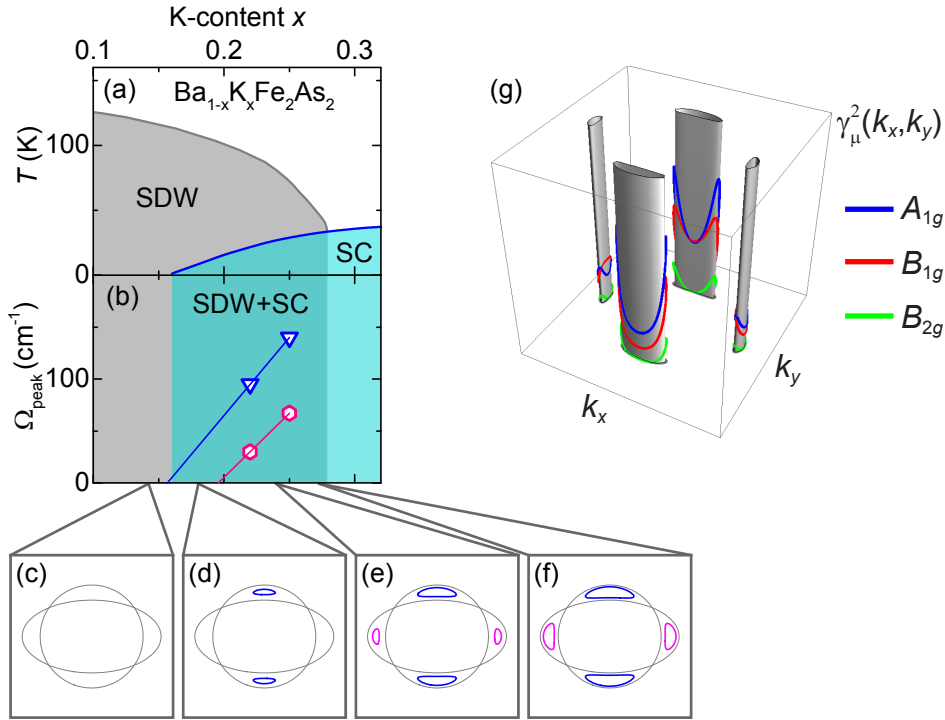


Figure 5.12: Analysis of the peak energies and Raman vertices in the coexisting state. (a) shows the phase diagram with the coexisting phase of superconductivity and SDW extended to (b) by the dark blue shaded area. The frequencies of the peak (pink) and the hump (blue) are depicted and extrapolated to zero frequency. (c-f) illustrate the doping dependent FS reconstruction. (g) The FS of (e) is used to calculate the squared Raman vertices. The 2D Fermi surfaces are artificially extended in γ_{μ}^2 -direction for illustrative purpose, indicating the Raman vertex at the FS.

squared Raman vertices of the three symmetries A_{1g} , B_{1g} and B_{2g} are plotted in Fig. 5.12(g). The B_{2g} Raman vertex is suppressed in comparison to A_{1g} and B_{1g} in agreement with the temperature independence of the response in B_{2g} symmetry. As 90° rotational symmetry is broken both A_{1g} and B_{1g} symmetries are affected by Coulomb screening effects. Note, that the phenomenological model applied in Section 5.1 yielded intensity factors for the response in each symmetry resulting in a suppression of the response in A_{1g} symmetry by a factor of 3 with respect to B_{1g} symmetry. If this factor is considered here as well, an agreement of the theory and the experiment is achieved. Although the interpretation of the peak at lower energies in terms of a collective mode can not completely be excluded, it is less plausible than the phenomenology by Maiti *et al.*. In addition, the qualitative success of the phenomenology can be considered a support of repulsive pairing interactions from which it started.

5.2.3 Evolution of competing pairing interactions close to optimal doping

The previous section clearly showed a strong dependence of the superconductivity-induced features on the shape of the Fermi surface. It follows a study in the doping range $0.35 \leq x \leq 0.48$ where the smooth evolution of the FS with doping serves as the basis on which the pairing interactions are tuned, see Fig. 2.5 of Chapter 2 [80, 81]. In BKFA the doping is directly proportional to the filling, which defines the number of extra holes. Hence the hole pockets grow and, simultaneously, the

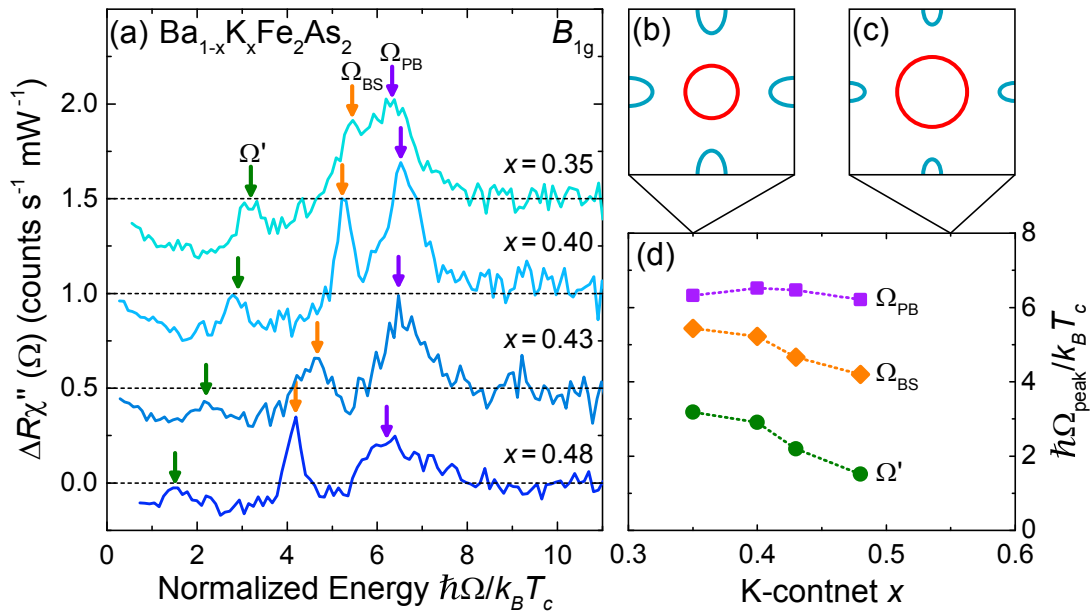


Figure 5.13: Doping dependent spectra of $\text{Ba}_{1-x}\text{K}_x\text{Fe}_2\text{As}_2$ in B_{1g} symmetry, ranging from $x = 0.35$ to 0.48. (a) shows difference spectra on a normalized energy scale. (b) and (c) display two sketches of the Fermi surface [48, 80] giving an orientation in the doping range. The size change is exaggerated for better visibility. (d) compiles the peak positions as a function of doping, associated with the pair-breaking peak at $\Omega_{PB}(x)$ (purple), the BS mode at $\Omega_{BS}(x)$ (orange) and the low energy peak at $\Omega'(x)$ (green).

electron pockets shrink with doping.

According to Fig. 5.13, which shows all energies in units of $k_B T_c$, the B_{1g} spectra symmetry exhibit the strongest doping dependence. The two modes at low energies (at Ω' and Ω_{BS}) move more than the high-energy peak (at Ω_{PB}). This dichotomy is clearly visualized in Fig. 5.13(d). The peak frequencies (in absolute units) are summarized in Table 5.2. Fig. 5.13 shows that (i) the high energy peak (purple arrows), assigned to the surviving part of the pair-breaking peak, stays at a nearly constant ratio of $\hbar\Omega_{PB}/k_B T_c \approx 6.5$, (ii) the narrow peak in the middle (orange

Table 5.2: Peak frequencies as obtained from B_{1g} spectra of $\text{Ba}_{1-x}\text{K}_x\text{Fe}_2\text{As}_2$ in the doping range $0.35 \leq x \leq 0.48$.

K-content x	Ω_{PB} (cm^{-1})	Ω_{BS} (cm^{-1})	Ω' (cm^{-1})
0.35	171	147	86
0.40	175	140	78
0.43	165	119	56
0.48	148	100	36

arrows), identified as BS mode, splits increasingly off the pair-breaking peak with increasing doping and (iii) the small peak (green arrows) shows a similar evolution as the BS mode.

Advanced theoretical studies [165] propose that the peak at Ω' (green) might be attributed to a second BS mode rather than a pair-breaking peak. In fact, two BS modes can independently show up in the same symmetry (B_{1g} in this case) if they correspond to orthogonal (e.g. first and second order B_{1g}) interactions. As this mode signals a second subdominant interaction to be present, having a much larger binding energy and hence higher subdominant coupling, the corresponding peaks are reinvestigated in the light of this hypothesis.

Identification of the low energy peak

For this purpose, the doping dependence of Ω' is compared with the magnitudes of the pair-breaking peaks found in the literature. Fig. 5.14 shows the results from ARPES and heat capacity measurements. According to ARPES experiments a small gap opens up on the outer hole pocket. However, the peak frequency Ω' does not follow the trend observed in the ARPES experiments [198] and the heat capacity measurements by Kant and coworkers [211]. In contrast, there is an agreement with the heat capacity measurements by Hardy and coworkers [212].

As this comparison is not finally conclusive, two possible origins for the peak at Ω' are discussed in the following: (i) The peak at Ω' is a pair-breaking peak and corresponds to a gap on the outer hole pocket [163]. (ii) A second BS mode appears at Ω' .

To solve this issue, the symmetry-resolved spectra are compared in Fig. 5.15. In addition, the temperature dependence of the optimally doped sample is reinvestigated and finally the spectral weight of a possible pair-breaking peak is discussed on the basis of the phenomenological model calculation applied in Section 5.1.

In Fig. 5.15, the peak frequency $\Omega'(x)$ is highlighted in green for each doping level

along with features at comparable frequencies in other symmetries. In order to check for coincidences, the various doping levels will be discussed successively. At $x = 0.35$, the spectrum in B_{2g} symmetry (c2) exhibits a weak peak in the superconducting

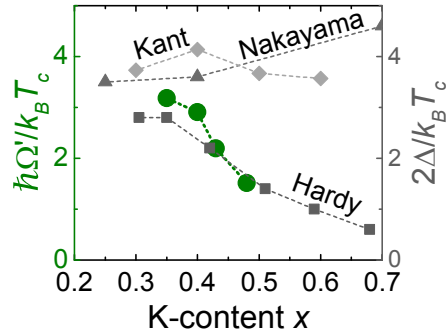


Figure 5.14: Comparison of $\Omega'(x)$ with gap magnitudes from literature. ARPES measurements by Nakayama *et al.* [198] and heat capacity measurements by Kant *et al.* [211] and Hardy *et al.* [212] show the doping dependence of the small gap $2\Delta/k_B T_c$. Dashed lines are guides to the eye.

state in a similar position as $\Omega'(0.35)$. However, since the spectrum above T_c shows a similar yet weaker structure, the difference spectra are expected to provide more insight. Apparently, both the onset and center positions of the B_{2g} peak are at energies higher by 7.5 cm^{-1} (corresponding to 3 sampling points) than the respective B_{1g} energies. As there is no close by feature in A_{1g} symmetry either, the B_{1g} peak at $\Omega'(0.35)$ has no correspondence in the other symmetries. For $x = 0.40$ there are neither prominent features in B_{2g} (d2) nor A_{1g} (d3) symmetry, corresponding to $\Omega'(0.40)$. The difference spectra reveal a weak hump in A_{1g} , with an onset of roughly 10 cm^{-1} below the onset of the peak in B_{1g} symmetry. Even though screening effects may reduce the intensity of potential pair-breaking features in A_{1g} , they are still expected to onset at the same energy 2Δ [55, 143]. A similar behavior is observed at $x = 0.43$. No indication of a peak is present neither in the raw data [Fig. 5.15(e1)] nor in the difference spectra [Fig. 5.15(e4)] for symmetries other than B_{1g} . Hence for all three doping levels there is more experimental evidence for a BS mode than for a pair-breaking peak.

In contrast peaks close to $\Omega'(0.48)$ are observed both in B_{2g} (f2) and A_{1g} (f3) symmetry. The A_{1g} peak is 5 cm^{-1} above $\Omega'(0.48)$, so only the peak in B_{2g} symmetry remains to consider. In fact, a pair-breaking peak cannot be excluded *a priori*. The missing A_{1g} signature of a putative gap and the results from the other doping levels suggest the peaks at Ω' to more likely originate in BS modes than pair breaking.

The question arises as to why no pair-breaking features are visible in the range of Ω' although the gap of the outer hole band is expected to be near by. Three arguments must be considered in this context: (i) The model calculation of Section 5.1 predicts a low intensity for a peak arising from pair-breaking at the outer hole pocket as shown in Fig. 5.5. Presumably the signal-to-noise ratios too poor to clearly resolve

the spectrum above T_c shows a similar yet weaker structure, the difference spectra are expected to provide more insight. Apparently, both the onset and center positions of the B_{2g} peak are at energies higher by 7.5 cm^{-1} (corresponding to 3 sampling points) than the respective B_{1g} energies. As there is no close by feature in A_{1g} symmetry either, the B_{1g} peak at $\Omega'(0.35)$ has no correspondence in the other symmetries.

For $x = 0.40$ there are neither prominent features in B_{2g} (d2) nor A_{1g} (d3)

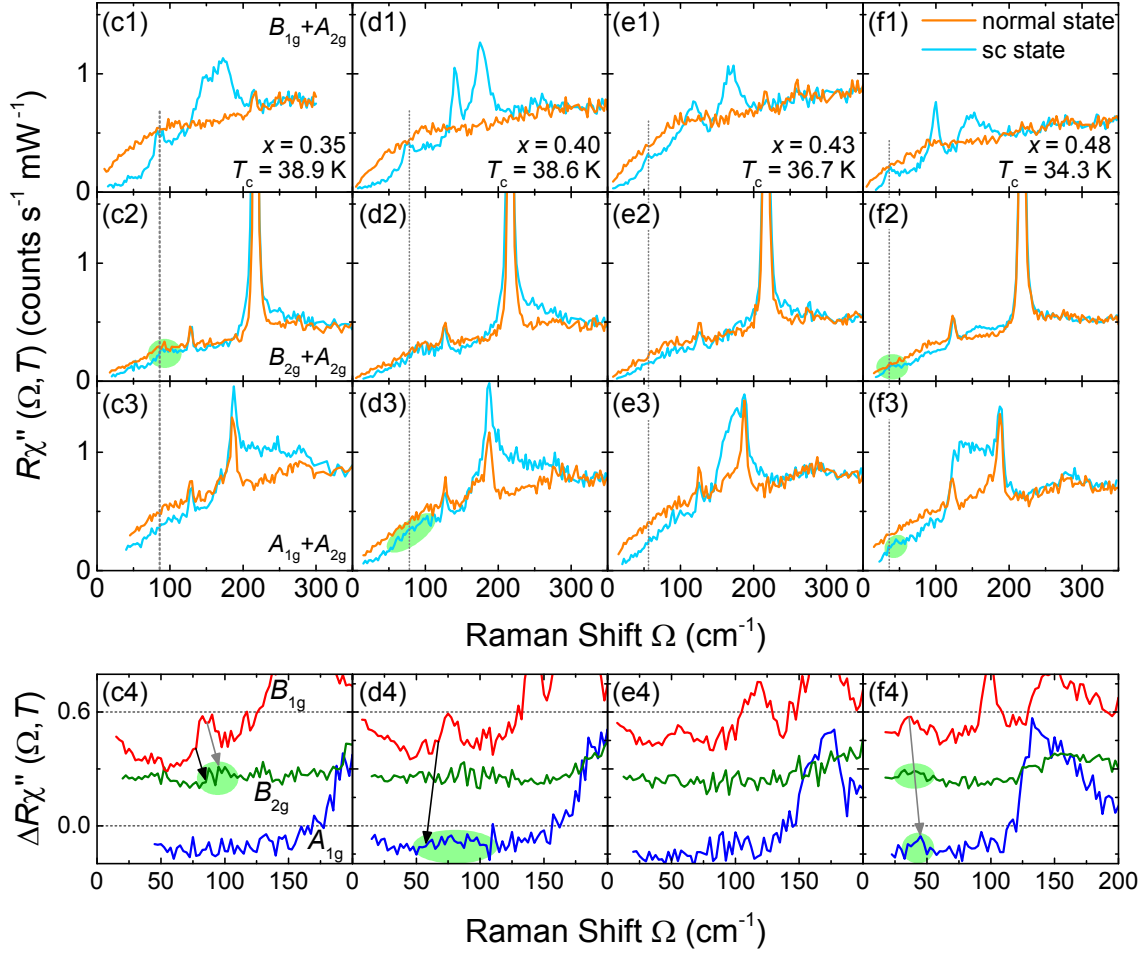


Figure 5.15: Symmetry-resolved spectra of $\text{Ba}_{1-x}\text{K}_x\text{Fe}_2\text{As}_2$ around optimal doping. (c-f) display spectra of doping levels $x = 0.35$ to $x = 0.48$, appended by 1, 2, and 3 referring to the symmetries $B_{1g} + A_{2g}$, $B_{2g} + A_{2g}$ and $A_{1g} + A_{2g}$, respectively [according to Fig. 5.8], 4 compiles the difference spectra. They show the bare symmetries and are stacked with an offset of 0.3. Note that the energy scale is different to enlarge the examined features. Dotted grey lines indicate the positions $\Omega'(x)$ of the low energy peak in B_{1g} symmetry. Green ellipses highlight features in other symmetries close to $\Omega'(x)$. (c4-f4) The arrows indicate the onset (black) and peak (grey) positions. The base of the arrows refer to B_{1g} symmetry, the head to the highlighted features in other symmetries.

this feature. (ii) Theoretical calculations suggest, that in the present two-gap system the pair-breaking peak related to Ω' vanishes if it exists at energies above the BS

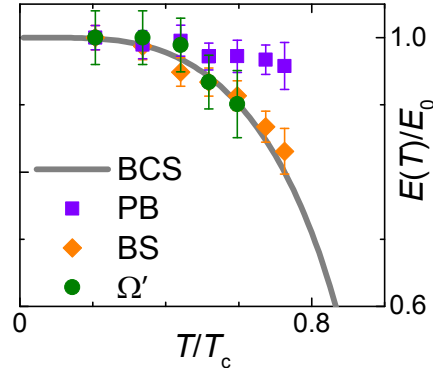


Figure 5.16: Temperature dependence of the three peaks in B_{1g} symmetry of the optimally doped sample. The peak energies are normalized to their respective energy E_0 at $T = 8$ K.

mode due to vertex corrections [122]. Hence in total only three peaks remain in B_{1g} symmetry, two BS modes and the surviving part of the high energy pair-breaking peak, as observed. (iii) The temperature dependences of the three superconducting B_{1g} peaks at optimal doping, as shown in Fig. 5.16, are studied. The peak positions are extracted from the spectra of Fig. 5.2. The peak at $\Omega'(x = 0.40, T)$ shifts to lower frequencies with increasing temperature and follows the same temperature dependence as the BS mode at 140 cm^{-1} [162]. Due to the simultaneous decrease of the intensity, the concomitant increasing of measurement time and the accumulation of surface layers, it was not possible to obtain data at $T > 23$ K.

In spite of the limited temperature range, also this study leads to the conclusion that the peaks at $\Omega'(x)$ are most naturally interpreted in terms of BS modes and thus correspond to a second subdominant channel in B_{1g} symmetry. As B_{1g} highlights the electron pockets only (see Fig. 5.3 of Section 5.1), the mode is attributed to a phase oscillation of the gap on the electron pockets, as it is the case for the weaker subleading channel at Ω_{BS} as well.

Competing pairing interactions as a function of doping

Given the compelling experimental evidence for the interpretation of the two low-energy B_{1g} modes in terms of two BS excitons a hierarchy of competing pairing interactions is the natural conclusion for BKFA near optimal doping. The discussion starts with a quantification of the relative pairing propensities and includes

two independent model calculations scrutinizing the interactions and leading to a hypothesis for the most relevant pairing mechanism.

Fig. 5.17(a) illustrates the resulting generic Raman response in B_{1g} symmetry which emerges from this picture. The BS modes are renamed as $\Omega_{\text{BS1}} \equiv \Omega'$ (green) and Ω_{BS2} (orange). BS1 is split off further from 2Δ than BS2, as quantified by the binding energies $E_{\text{B}}^{(1)}$ and $E_{\text{B}}^{(2)}$, respectively. Hence BS1 corresponds to a stronger

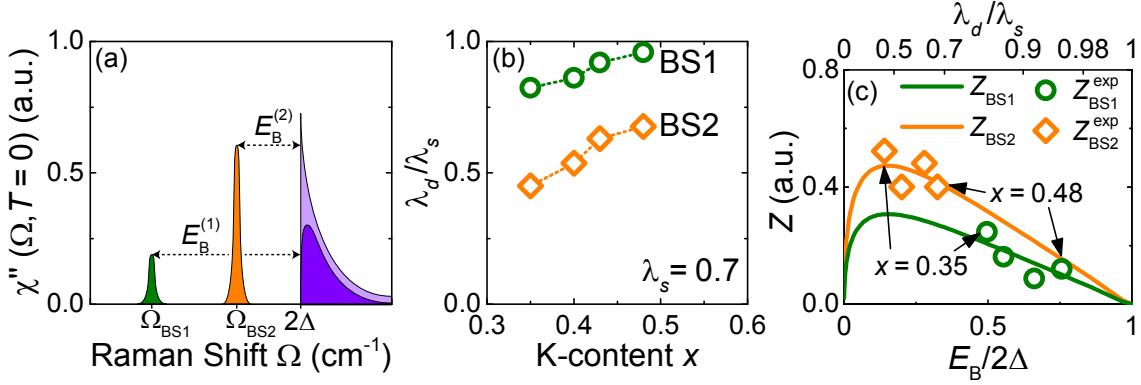


Figure 5.17: Results of the analysis in the doping range $0.35 \leq x \leq 0.48$. (a) shows a schematic drawing of the Raman response in B_{1g} symmetry. Green and orange peaks refer to the BS modes. The pair-breaking peak in the absence of BS modes is shown in light purple, the surviving part in the presence of the modes in dark purple. (b) For both modes the ratio $\lambda_{d(i)}/\lambda_s$ is extracted, with $i = 1, 2$ corresponding to BS1 and BS2, respectively. (c) shows the spectral weights Z of the modes. The experimentally obtained spectral weights $Z_{\text{BS1}}^{\text{exp}}$ and $Z_{\text{BS2}}^{\text{exp}}$ are shown along with prediction of Eq. 5.11 with the relation $Z_{\text{BS1}} = 0.65Z_{\text{BS2}}$. With $\lambda_s = 0.7$, the scaling on the top axis of abscissa is obtained.

subdominant channel than BS2. From the position of the BS(i) ($i = 1, 2$) modes and the magnitude of the corresponding superconducting gap, the coupling parameters $\lambda_{d(i)}$ can be extracted. As there are too many degrees of freedom the approximation of an isotropic gap ($\Delta(\mathbf{k}) = \Delta$) on the electron pockets has to be made. This gap is defined by the peak in B_{1g} symmetry at $2\Delta = \Omega_{\text{PB}}$ as illustrated in Fig. 5.13. The pairing parameters are related to the frequency of the BS mode $\Omega_{\text{BS}(i)}$ by [45, 46]

$$\langle g_{(i)}^2(\mathbf{k}) \rangle \bar{P}(\Omega_{\text{BS}(i)}) \equiv \eta_{(i)} \bar{P}(\Omega_{\text{BS}(i)}) = \left[\frac{\lambda_z^{(i)}}{\Omega_{\text{BS}(i)}^2} (2\Delta)^2 + \frac{1}{\frac{1}{\lambda_{d(i)}} - \frac{1}{\lambda_s}} \right]^{-1} \xrightarrow{\lambda_z^{(i)}=0} \frac{1}{\lambda_{d(i)}} - \frac{1}{\lambda_s} \quad (5.10)$$

with definitions as in Eq. 5.8. For the determination of the ratio $\lambda_{d(i)}/\lambda_s$ the factor $\eta_{(i)} \equiv \langle g_{(i)}^2(\mathbf{k}) \rangle$ is irrelevant. The additional coupling parameter $\lambda_z^{(i)}$, which acts in the particle-hole (or zero-sound) channel, appears in Eq. 5.10. It was neglected in Ref. [46] but its magnitude can be as large as $\lambda_z^{(i)} = -\lambda_{d(i)}$ in the BCS approx-

imation [45]. Since the potential influence of λ_z increases with increasing λ_s the ratio $\lambda_{d(i)}/\lambda_s$ was calculated for various realistic values of λ_s for the two limiting cases $\lambda_z = 0$ and $\lambda_z = -\lambda_d$ (App. 7.4). For $\lambda_s \approx 0.7$ relevant here [48, 49, 51] $\lambda_z^{(i)}$ was found to be of small influence. With $\lambda_z = 0$ and $\lambda_s = 0.7$, the ratios $\lambda_{d(i)}/\lambda_s$ of BS1 and BS2 are shown in Fig. 5.17(b). The ratio $\lambda_{d(1)}/\lambda_s$ always stays well above $\lambda_{d(2)}/\lambda_s$, reaching close to 1 ($\lambda_d = \lambda_s$) and thus proving the existence of a strong competition between s -wave and d -wave channels. A clear increase of the ratios $\lambda_{d(i)}/\lambda_s$ with doping is observed for both modes as can either be caused by the increase of the subdominant pairing strengths or the weakening of the dominant pairing.

The analysis of the relative spectral weights of the modes provides further insight. First, the dependence of the spectral weight on the binding energy is derived following Refs. [45] and [46]. Close to $\Omega_{\text{BS}(i)}$, the expansion $\eta_{(i)}\bar{P}(\Omega_{\text{BS}(i)}) \approx 1/\lambda_{d(i)} - 1/\lambda_s + \frac{\partial\eta_{(i)}\bar{P}}{\partial\Omega}\Big|_{\Omega=\Omega_{\text{BS}(i)}}(\Omega - \Omega_{\text{BS}(i)})$ can be used. According to Eq. 5.7, the spectral weight in the limit of an isotropic gap is given by

$$\begin{aligned} Z_{\text{BS}(i)}(\Omega_{\text{BS}(i)}) &= \theta_{(i)} \int_{-\infty}^{\infty} d\Omega \operatorname{Im} \left[\frac{8\Delta^2}{\Omega_{\text{BS}(i)}^2} \frac{\bar{P}^2(\Omega_{\text{BS}(i)})}{\frac{1}{\lambda_{d(i)}} - \frac{1}{\lambda_s} - \eta_{(i)}\bar{P}(\Omega) - i\delta} \right] \\ &= \theta_{(i)} \frac{8\Delta^2 \bar{P}^2(\Omega_{\text{BS}(i)})}{\Omega_{\text{BS}(i)}^2} \int_{-\infty}^{\infty} d\Omega \frac{\delta}{\left[\frac{\partial\eta_{(i)}\bar{P}}{\partial\Omega}\Big|_{\Omega=\Omega_{\text{BS}(i)}}(\Omega - \Omega_{\text{BS}(i)}) \right]^2 + \delta^2} \quad (5.11) \\ &= \frac{\theta_{(i)}}{\eta_{(i)}} \frac{8\Delta^2 \bar{P}^2(\Omega_{\text{BS}(i)})\pi}{\Omega_{\text{BS}(i)}^2 \frac{\partial\bar{P}}{\partial\Omega}\Big|_{\Omega=\Omega_{\text{BS}(i)}}} \end{aligned}$$

with the phenomenological broadening δ and the momentum dependence of $g_{(i)}(\mathbf{k})$ and $\gamma^{B_{1g}}(\mathbf{k})$ as isolated by the factor

$$\theta'_{(i)} \equiv \frac{\theta_{(i)}}{\eta_{(i)}} = \left\langle \frac{g_{(i)}(\mathbf{k})}{\sqrt{\eta_{(i)}}} \gamma^{B_{1g}}(\mathbf{k}) \right\rangle^2 \equiv \langle g'_{(i)}(\mathbf{k}) \gamma^{B_{1g}}(\mathbf{k}) \rangle^2 \quad (5.12)$$

with the normalized form factor $g'_{(i)}(\mathbf{k})$. It is evident from Eq. 5.11 that the spectral weight can be formulated in a way that it only depends on $\Omega_{\text{BS}(i)}$ and 2Δ , or alternatively on $E_{\text{B}}^{(i)}/2\Delta$ if the absolute spectral weight is irrelevant. Hence the experimentally obtained spectral weights can be compared to the result of Eq. 5.11. It is obvious from this equation that $Z_{\text{BS}(i)}$ does not explicitly depend on λ_s and $\lambda_{d(i)}$. Fig. 5.17(c) compiles experiment and theory displaying the following results: (i) The experimentally obtained spectral weights of both modes ($Z_{\text{BS1}}^{\text{exp}}$ and $Z_{\text{BS2}}^{\text{exp}}$)

follow the trend predicted by Eq. 5.11. The experimentally obtained weight $Z_{\text{BS2}}^{\text{exp}}$ remains nearly constant whereas $Z_{\text{BS1}}^{\text{exp}}$ decreases with $E_{\text{B}}^{(i)}/2\Delta$. (ii) Z_{BS1} lies below Z_{BS2} .

This relative suppression can only be caused by the momentum dependence as incorporated in $\theta'_{(i)}$, i.e. $Z_{\text{BS1}}/Z_{\text{BS2}} = \theta'_{(1)}/\theta'_{(2)}$. As the Raman vertices are equal for both modes, the difference in relative spectral weight must result from $g'_{(1)}(\mathbf{k}) \neq g'_{(2)}(\mathbf{k})$. For competing interactions, a further requirement is orthogonality, i.e. $\langle g'_{(1)}(\mathbf{k})g'_{(2)}(\mathbf{k}) \rangle = 0$. As a first approximation, $g'_{(2)}(\mathbf{k})$ and $g'_{(1)}(\mathbf{k})$ are proposed to be of first and second order B_{1g} symmetry, which guarantees orthogonality [compare Fig. 4.2 of Chapter 4]. The first order B_{1g} eigenvector is nearly constant on the electron pockets, whereas the second order one has nodes which lead to cancellation effects in the FS average. Since the BS1 and BS2 modes are associated with the nodal second and, respectively, non-nodal first order eigenvector, Z_{BS1} is smaller than Z_{BS2} .

The pairing mechanism

The results of the previous analysis allow already some qualitative conclusions as to the pairing before a detailed theoretical analysis will be discussed in the next paragraph.

Whereas phonon-based mechanisms have been discarded early [113, 114, 213–215] AFM exchange is more likely to be a player. There are ARPES experiments that argue in favor of this interaction because of the observed gap structure [198, 216]. However, calculations show that the subdominant d -wave coupling strength within this framework rapidly decreases with increasing doping [88]. As exactly the opposite is observed in the Raman experiments, AFM interactions are unlikely to be at work in BKFA.

Hence a suitable interaction is searched for in the picture of fluctuation-mediated pairing, which still offers a huge variety of possibilities [15, 49, 58, 77, 116–118], as illustrated in Fig. 2.11.

The case for spin fluctuations is discussed first. Spin fluctuations provide for an inter-band interaction between hole and electron pockets. As this interaction is repulsive it generates a superconducting s^{\pm} state. A second interaction acts between two neighboring electron pockets, which is repulsive as well, yielding a d -wave pairing. Both interaction rely on a nesting condition [49]. As the matching of the sizes of electron and hole pockets diminishes with higher doping, λ_s will decrease but λ_d will be unaffected, resulting in a rise of λ_d/λ_s .

A similar effect arises for both charge and orbital fluctuations. The attractive inter-band charge or antiferro-orbital coupling channels can support an s^{++} ground state. Additionally, an attractive subdominant intra-band interaction with an interaction vector $Q \approx (0, 0)$ is acting. However, if this interaction acquires a B_{1g} -symmetric form factor, which is the case for intra-band charge and ferro-orbital interactions, it competes with the s^{++} ground state. This will result in a BS mode to appear. It is thus possible that the ground state coupling decreases more rapidly than the subdominant coupling, resulting in a doping dependence as observed.

In summary it is found that fluctuation mediated pairing is favored. The discussed proposals for spin, charge, and orbital fluctuations can independently generate a BS mode and a doping dependence as found in the experiment.

Comparison of experiment and theory

For a microscopic picture a functional renormalization-group (fRG) study [92, 188, 217–219] and an RPA-based analysis [49, 51, 77, 90, 183–185] will be discussed now. Motivated by the Raman experiment new fRG and RPA analyses were performed by Christian Platt based on Ref. [92], and respectively, by Thomas Maier according to Ref. [48].

Both techniques yield a hierarchy of pairing interactions. The leading interaction forms the superconducting ground state, the subleading ones are responsible for BS modes. The pairing interaction $V_{\mathbf{k}, \mathbf{k}'}$ is decomposed into form factors (eigenvectors) $g_l(\mathbf{k})$ and corresponding coupling parameters (eigenvalues) λ_l [77, 92]

$$-\sum_b \int_{\mathbf{k}' \in \text{FS}_b} \frac{d\mathbf{k}'}{(2\pi)^3} \frac{1}{v_F(\mathbf{k}')} V_{\mathbf{k}, \mathbf{k}'} g_l(\mathbf{k}') = \lambda_l g_l(\mathbf{k}). \quad (5.13)$$

The space group of the electronic system defines a basis for $g_l(\mathbf{k})$, containing irreducible representations in first and higher orders.

Both methods will yield an s^\pm -symmetric (A_{1g}) ground state and subdominant d -symmetric (B_{1g}) channels with the eigenvalues $\lambda_s > \lambda_{d(1)} > \lambda_{d(2)} > \dots$. As two BS modes were observed, the following analysis will be confined to the first two subdominant interactions $\lambda_{d(1)}$ and $\lambda_{d(2)}$. The theoretical calculations were applied to the $k_z = 0$ cut of the 1 Fe BZ as depicted in Fig. 4.10(d). To derive the pairing interactions, they are based on the same interaction Hamiltonian as introduced in Eq. 2.2.

The fRG and RPA analyses start from bare interactions [220] of Tab. 5.3. In an fRG analysis, the bare propagators and bare interactions are iteratively renormalized in

Table 5.3: The bare interaction parameters used as starting parameters of the fRG and RPA analyses are listed.

Parameter	fRG (eV)	RPA (eV)
U_{inter}	4.0	0.85
U_{intra}	2.0	0.43
J_{Hund}	0.7	0.21
J_{pair}	0.7	0.21

a self-consistent way [92]. As all renormalization processes are included, the fRG represents an unbiased method to gain the final, effective interaction $V_{\mathbf{k},\mathbf{k}'}$ [221]. The obtained eigenvectors and eigenvalues are illustrated in Fig. 5.18(a-c) and (d),

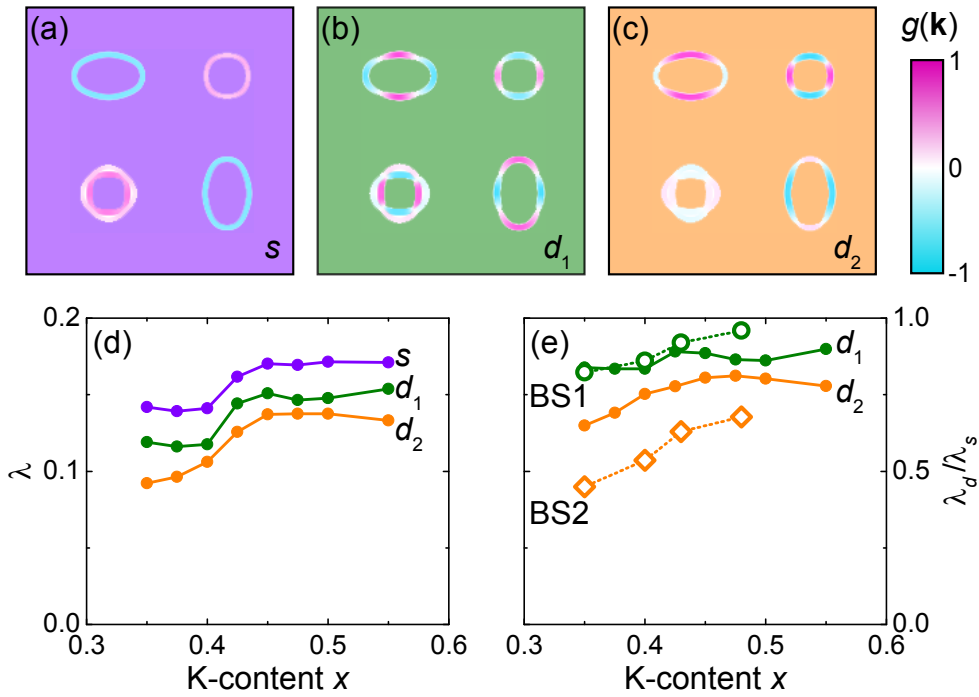


Figure 5.18: Comparison of the fRG results with the experiment. (a-c) depict the eigenvectors $g(\mathbf{k})$ at the Fermi surfaces of the first quadrant of the BZ. The panels correspond to the dominant s^\pm channel in (a) and the two subdominant channels d_1 and d_2 in (b) and (c), respectively. (d) shows the eigenvalues of these channels as a function of doping. (e) The ratios $\lambda_{d(i)}/\lambda_s$ as extracted from the BS modes BS1 and BS2 (open symbols) are compared with the fRG results.

respectively. A comparison of the relative coupling strengths $\lambda_{d(i)}/\lambda_s$ found in the experiment and in fRG is presented in Fig. 5.18(e). An agreement is found, not only the increasing ratios with doping but also the absolute magnitudes are reproduced

very well for both BS modes. In addition, the eigenvectors are compatible with the relative spectral weights of BS1 and BS2 [Fig. 5.17(c)] since the sign-changing nodal state d_1 has a smaller FS average $\langle g'(\mathbf{k})\gamma^{B1g}(\mathbf{k}) \rangle$ than the sign-preserving state d_2 . As the fRG treats spin, charge and orbital channels on an equal footing, the dominant interaction cannot be determined directly. Hence a comparison with the RPA based calculation is performed, which explicitly favors the spin-fluctuation channel. Whereas the starting parameters are being renormalized in the fRG flow, RPA uses renormalized parameters (see Tab. 5.3) from the start. Yet this approach still yields the same results if the spin channel is really dominating the system [222]. The results are shown in Fig. 5.19. The eigenvectors $g'_{(i)}(\mathbf{k})$ [Fig. 5.19(a-c)], the magnitudes [Fig. 5.19(d)], and the ratios $\lambda_{d(i)}/\lambda_s$ [Fig. 5.19(e)] agree qualitatively with the RPA

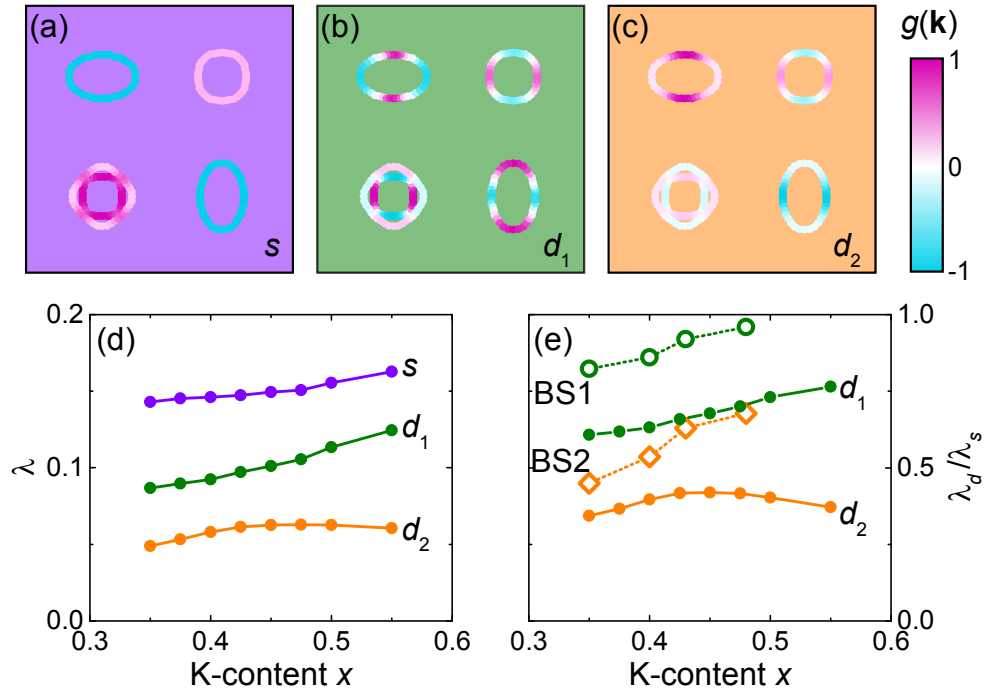


Figure 5.19: Comparison of the RPA results with the experiment. Similar to Fig. 5.18, (a-c) show the RPA eigenvectors, (d) shows the eigenvalues and (e) a comparison with the experiment.

results and with the experiment. This agreement suggests repulsive spin fluctuation to be the main driving force for the subdominant interactions and hence responsible for the emergence of the BS modes. According to the theoretical analysis, it is a small step to determine spin fluctuations as the most relevant interaction for the leading channel as well in the hole-doped iron pnictide $\text{Ba}_{1-x}\text{K}_x\text{Fe}_2\text{As}_2$. Following the theory, the detailed shape and size of the Fermi surface is an important prop-

erty, as the enhancement of spin fluctuations depends on the nesting. However, as opposed to the SDW where a single nesting vector dominates, the Lindhard susceptibility is large for a variety of Q vectors in the case of superconductors [50, 77, 223]. As small changes of the FS have a huge influence on the subdominant coupling strength, it is not surprising, that the spectra exhibit qualitative changes already above $x = 0.48$.

5.2.4 Development of the gap structure at high doping levels

To explain the new peaks and the changes at $x = 0.62$ and $x = 0.70$ the Fermi surface is considered first. In this range, the sizes of the Fermi surface sheets change considerably up to $x = 0.62$ and $x = 0.70$, however, there is no qualitative difference, i.e. the smooth evolution of the FS, starting at $x = 0.35$ continues up to $x = 0.70$ [198]. Hence it is possible that the qualitative change of the spectra is triggered by the strongly competing interactions discovered above, resulting in a qualitative change of the superconducting ground state at a critical doping level [109].

To determine if this is really the case, the spectra as compiled in Fig. 5.20 will be analyzed now. The changes are most pronounced in B_{1g} symmetry: (i) For $x = 0.48 \rightarrow 0.62$ the BS1 mode (green) disappears [Fig. 5.8(f1) and (g1)], (ii) the low-energy response in the superconducting state changes from displaying a true gap to a linear increase and (iii) a new peak pops up [Fig. 5.20(a) and (d)].

Fig. 5.20(a) displays that the intensity increases continuously with the Raman shift, starting from the first point measured at 7.5 cm^{-1} . The same linear rise is observed for $x = 0.70$ in (d). A linear increase is typical for a nodal gap at $T \ll T_c$, where the pair-breaking response is not vanishing even for the smallest energies as illustrated in Fig. 2.10(d). This is in contrast to a full gap, where no pair breaking occurs below a certain energy $2\Delta_{\min}$ [160]. This is a first indication of a changed superconducting ground state.

Going towards higher energies, a very narrow peak at 55 cm^{-1} is present for $x = 0.62$. This peak is closely followed by another peak at 70 cm^{-1} , as shown in Fig. 5.20(b), marked by a cyan open diamond and a black asterisk, respectively. Finally a broader maximum is observed, which is centered at about 110 cm^{-1} .

The first of the observed peaks (cyan) follows the BCS temperature dependence [4]. In combination with its narrow linewidth and the unique appearance in B_{1g} , an identification as a BS mode is very likely. The second peak at 70 cm^{-1} has not

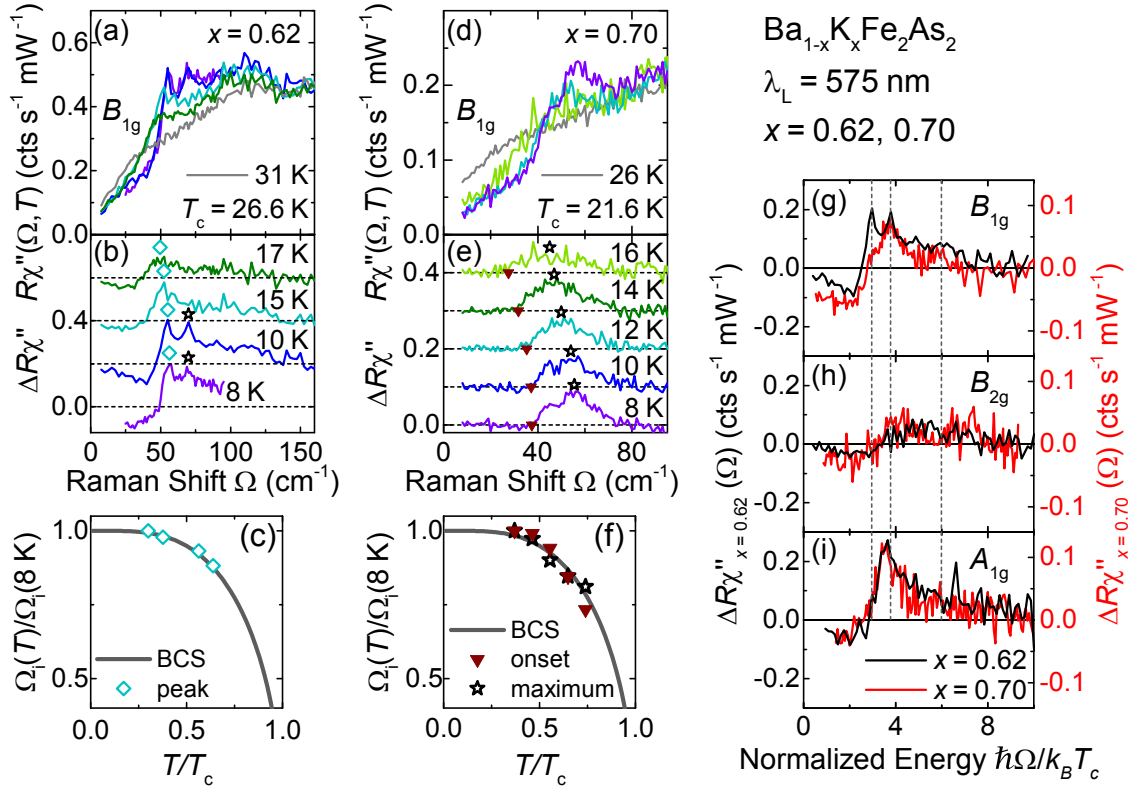


Figure 5.20: Raman response of $\text{Ba}_{1-x}\text{K}_x\text{Fe}_2\text{As}_2$ at $x = 0.62$ and $x = 0.70$. (a-c) are related to $x = 0.62$, (d-f) to $x = 0.70$. (a) and (d) show the raw data, (b) the difference spectra offset by 0.2 and in (e) by 0.1 counts $\text{mW}^{-1} \text{s}^{-1}$, here with a linear function subtracted. The temperature dependence of peaks in (b) as illustrated by open cyan diamonds is comprised in (c) along with the temperature dependence of the gap according to BCS theory (grey line). (e) and (f) show a similar analysis. Here the wine triangles indicate the onset frequency, the open black stars the peak frequency. (g-i) compare the difference spectra of the two samples in B_{1g} , B_{2g} , and A_{1g} symmetry, respectively, using an energy scale normalized to the respective T_c . Note the different intensity scales for the doping levels. The grey dashed lines indicate the positions of various features.

been observed so far. It appears for the two lowest temperatures, 8 and 10 K, but for higher temperatures, at 15 and 17 K it is no longer present. The special temperature dependence indicates clearly that this peak is a new feature emerging first at $x = 0.62$.

Since the broader maximum around 110 cm^{-1} has the same ratios $2\Delta/k_B T_c \approx 6$ for $x = 0.62$ and $x = 0.48$ it is tempting to interpret it in terms of pair-breaking similarly as for lower optimal doping levels, i.e. originating from pair-breaking processes on the electron pocket.

For $x = 0.70$ [Fig. 5.20(d-f)] the intensity of the first peak decreases dramatically. It appears as a shoulder at 8 K and as a small peak at 10 K, for higher temperatures it can not be resolved any further. However, it may still be a part of the total response though indistinguishable from the second peak right above, marked by the black asterisk. Thus the energies are extracted where the spectra first deviate from a linear energy dependence, as indicated by the wine triangles in Fig. 5.20(e) and (f) yielding approximately the onset of the first peak. The second peak (black asterisk), which was found to be new at high doping levels, is stronger in comparison to the other features and now persists up to the highest measured temperature of 16 K. Both peaks exhibit a BCS-like temperature dependence.

Finally the spectra are compared in all symmetries for $x = 0.62$ and $x = 0.70$. The feature assigned as pair-breaking peak for $x = 0.62$ is very weak for $x = 0.70$ if visible at all. A plot of all difference spectra in 5.20(g-i) on a normalized energy scale $\hbar\Omega/k_B T_c$ shows that this very small peak in B_{1g} symmetry is located at roughly 6 (marked with the rightmost dashed line). This may suggest the interpretation as a small remaining pair-breaking peak as for $x = 0.62$. Next to this feature, all the other ones in B_{1g} symmetry coincide in position for both doping levels but differ in intensity. It is evident that the first peak (leftmost dashed line) appears uniquely in B_{1g} symmetry as in the case of the BS mode. The new peak (middle dashed line) is close to the peak in A_{1g} , but not exactly at the same position. Hence this might also be attributed to a second mode.

With these findings, two ideas are presented to explain the changes that occur at $x = 0.62$ and $x = 0.70$. Since the Fermi surface is believed to develop smoothly up to $x = 0.70$ and the d -wave and s -wave coupling strengths approach each other a change of the symmetry of the superconducting state is proposed [50, 111, 112, 191, 224]. Either a combined $s + id$ state emerges, or the d -wave interaction even exceeds the s -wave interaction and forms a d -wave ground state.

One of the ideas is based on the work of Khodas and coworkers [155]. They ar-

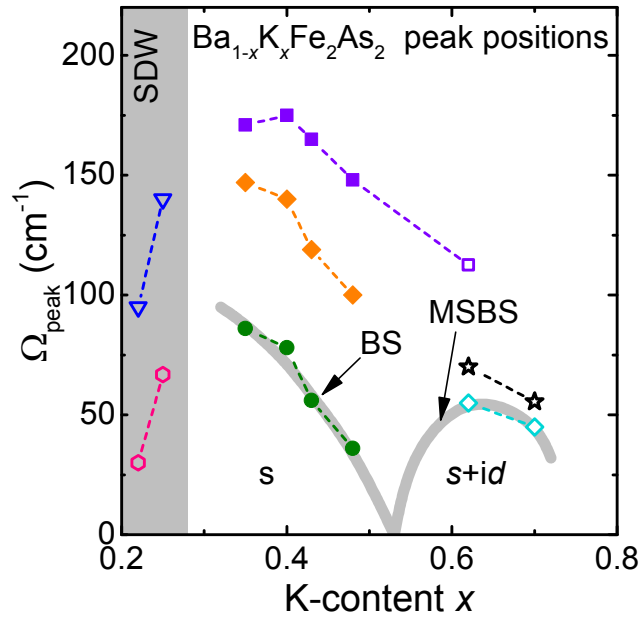


Figure 5.21: Expected doping dependence of a BS and MSBS mode [112]. The BS mode (grey) in the s -wave state around optimal doping turns into a MSBS mode in the $s + id$ state. Its frequency drops to zero at the transition, which is located at around $x = 0.53$.

gue, that, in general, two modes arise, one in the particle-particle and one in the particle-hole channel. Both channels are intertwined, if the momentum average of $\langle GF \rangle$ on the FS is large, resulting in only one mode below the gap edge. (G and F refer to the normal and anomalous Green's function as defined in Eqs. 4.7 and 4.8.) In the case of $\langle GF \rangle \approx 0$ they are disentangled and can separately be observed as two modes. F is linearly proportional to the gap Δ , but G only depends on the gap squared. Hence a simple approximation yields $\langle GF \rangle \rightarrow \langle \Delta(\mathbf{k}) \rangle$. For an isotropic gap only one mode is expected, whereas for a sign-changing gap two modes will appear in this framework. So the two peaks with lowest energies in B_{1g} symmetry could resemble these two modes, indicating a d -wave ground state.

Another idea was suggested by Maiti and Hirschfeld [112], who analyzed an $s + id$ ground state, where s - and d -wave states are mixed. The response of this state yields a full gap, as $|\Delta_s + i\Delta_d|^2 = \Delta_s^2 + \Delta_d^2$ never vanishes, even if the d -wave part itself is nodal at the Fermi surface. The Raman spectra are thus expected to show an anisotropic pair-breaking response as discussed in Section 5.1. Below the gap edge a BS mode exists with a special frequency dependence on doping as illustrated in Fig. 5.21. The frequency vanishes at the onset of the $s + id$ state and the mode reappears in the mixed phase as a so-called mixed-state BS (MSBS) mode. If a linear extrap-

olation is applied to the frequency dependence of the peaks in the optimally doped region, the BS1 peak (green) is the only candidate that reaches zero frequency below $x = 0.62$. The corresponding nodal d -wave state, combined with the original s -wave state yields the new $s + id$ state. To check this possibility a Raman experiment is suggested on a sample with a doping of $x = 0.55$, between $x = 0.48$ and $x = 0.62$. In summary it was demonstrated that the system may transform into a new state of superconductivity with a manifold of new effects. In spite of some open questions, a consistent picture of spin-fluctuation-mediated superconductivity could be presented. A detailed analysis of spin fluctuations will thus be studied in the next section. The unique opportunity arises to directly observe the fluctuations [73] and gain a microscopic understanding of them rather than to reverse engineer the pairing interaction from the investigation of the superconducting state, though this proved to be successful here as well.

5.3 Fluctuations in $\text{Ba}(\text{Fe}_{1-y}\text{Co}_y)_2\text{As}_2$ and $\text{Ba}_{0.78}\text{K}_{0.22}\text{Fe}_2\text{As}_2$

Fluctuations were observed by Raman scattering relatively early [214]. However, for an extended period of time the “quasi-elastic” response was interpreted in terms of orbital and charge fluctuations [163, 225, 226]. Spin fluctuations as an origin of the response was considered first theoretically [145, 227–229] and later experimentally [73]. However, the interrelation of fluctuations and superconductivity remains elusive.

To proceed here, the results on BFCAs on the electron doped side [73, 74, 124, 125] shall be augmented by studying $\text{Ba}(\text{Fe}_{0.949}\text{Co}_{0.051})_2\text{As}_2$, and extended to the hole doped $\text{Ba}_{0.78}\text{K}_{0.22}\text{Fe}_2\text{As}_2$.

The phase diagram of Fig. 5.22 compiles all measurements performed on these compounds, locating the doping and temperature for which spectra were obtained in

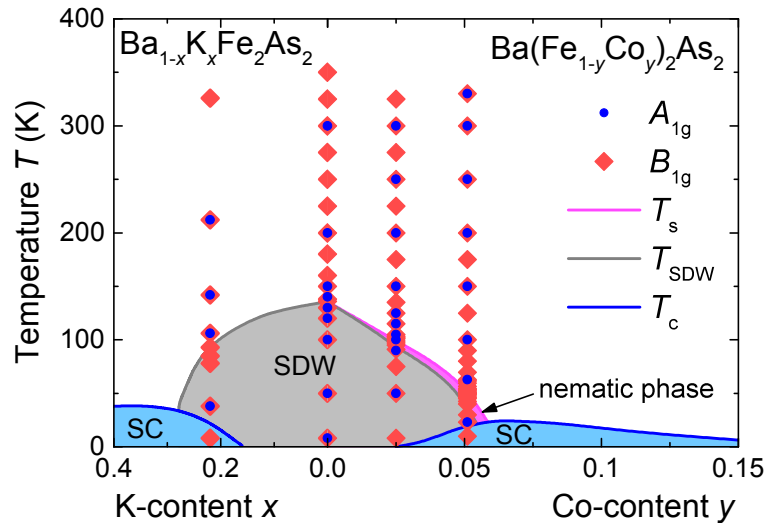


Figure 5.22: Sampling points in the phase diagram of K and Co doped BaFe_2As_2 . The K- and Co-doped sides are adopted from Ref. [70] and Ref. [60], respectively. Red diamonds show the doping and temperature, where B_{1g} spectra were obtained, blue dots depict the sampling points in A_{1g} symmetry. The narrow nematic phase (magenta) is of special interest.

B_{1g} and A_{1g} symmetry. The following study will concentrate on the new data and refer to Refs. [73, 124, 125] for details of the analysis.

The phase diagram exhibits certain peculiarities that motivated a study of the doping dependence of the fluctuations. The discussion will thus be based on three aspects: (i) The asymmetry of the hole- and electron-doped side [65, 230], especially

the splitting of the structural and magnetic transition for electron doping, (ii) the investigation of the correlation length and possibility for a QCP close to optimal doping [231–233], and (iii) the doping- and temperature-dependent strength of the fluctuations with an outlook to a possible relation with superconductivity [234, 235].

5.3.1 Experimental results and analysis

Before several doping levels are compared, the temperature and symmetry dependence of the spectra is analyzed in terms of fluctuations [71–74, 108, 124, 125, 134, 135, 158, 163, 236–239]. For this purpose the experimental results of the new sam-

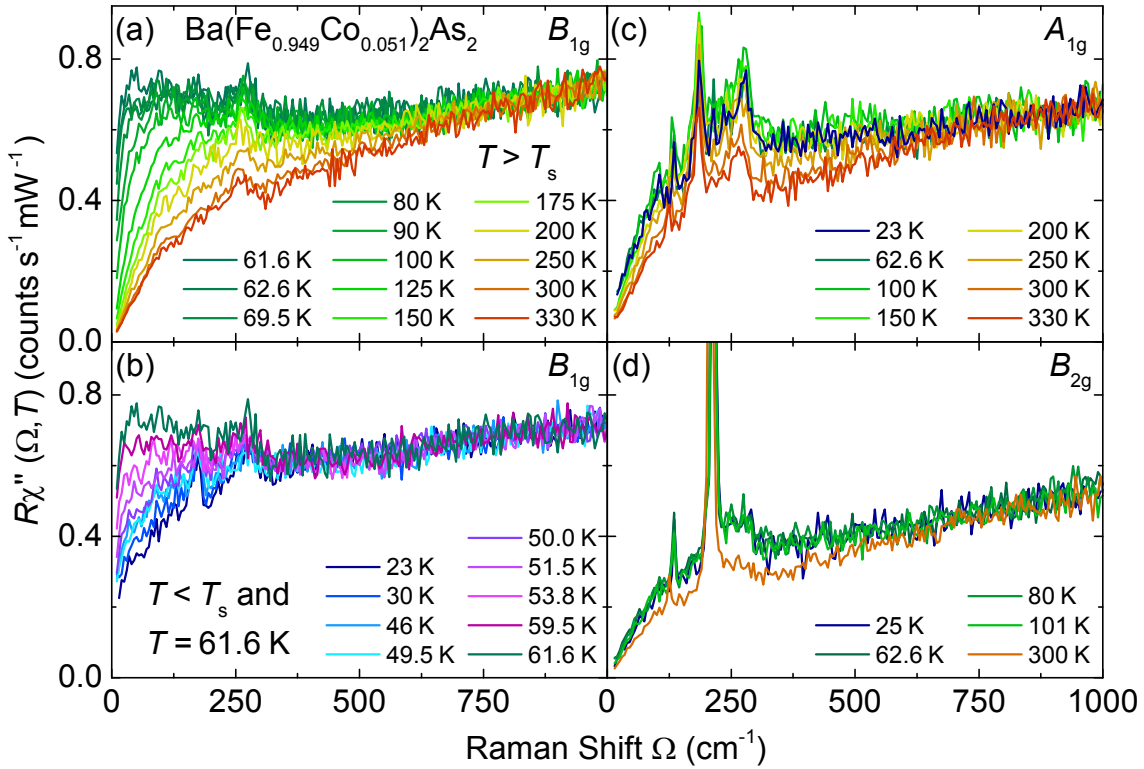


Figure 5.23: Raman spectra of $\text{Ba}(\text{Fe}_{0.975}\text{Co}_{0.025})_2\text{As}_2$ [73, 134]. (a) and (b) show spectra in B_{1g} symmetry. The colors represent different regions in the phase diagram: Red and yellow colors show the range where the electron-hole continuum dominates the response, green colors mark the region where fluctuations emerge, magenta stands for the nematic phase and blue for the SDW phase. (c) and (d) show spectra in A_{1g} and B_{2g} symmetry, respectively. The spectra from 100 K to 300 K in A_{1g} symmetry were adopted from Ref. [124].

ples ($y = 0.051$ and $x = 0.022$) are presented in combination with a method that enables the isolation of the bare contribution from the fluctuations.

To compare the temperature and doping dependent measurements the spectra were multiplied in a way that they merge at 1000 cm^{-1} for all temperatures and doping levels. They are normalized to the raw spectra of the undoped mother compound BaFe_2As_2 , separately for each symmetry. The normalization eliminates potential surface and overall scaling effects due to a doping-dependent Raman vertex, specifically the effect of resonances.

The normalized B_{1g} Raman spectra for $y = 0.051$ are shown in Fig. 5.23. They were obtained with an excitation wavelength of 514 nm and a spectral resolution of 7 cm^{-1} . Fig. 5.23(a) illustrates the temperature evolution above the structural tran-

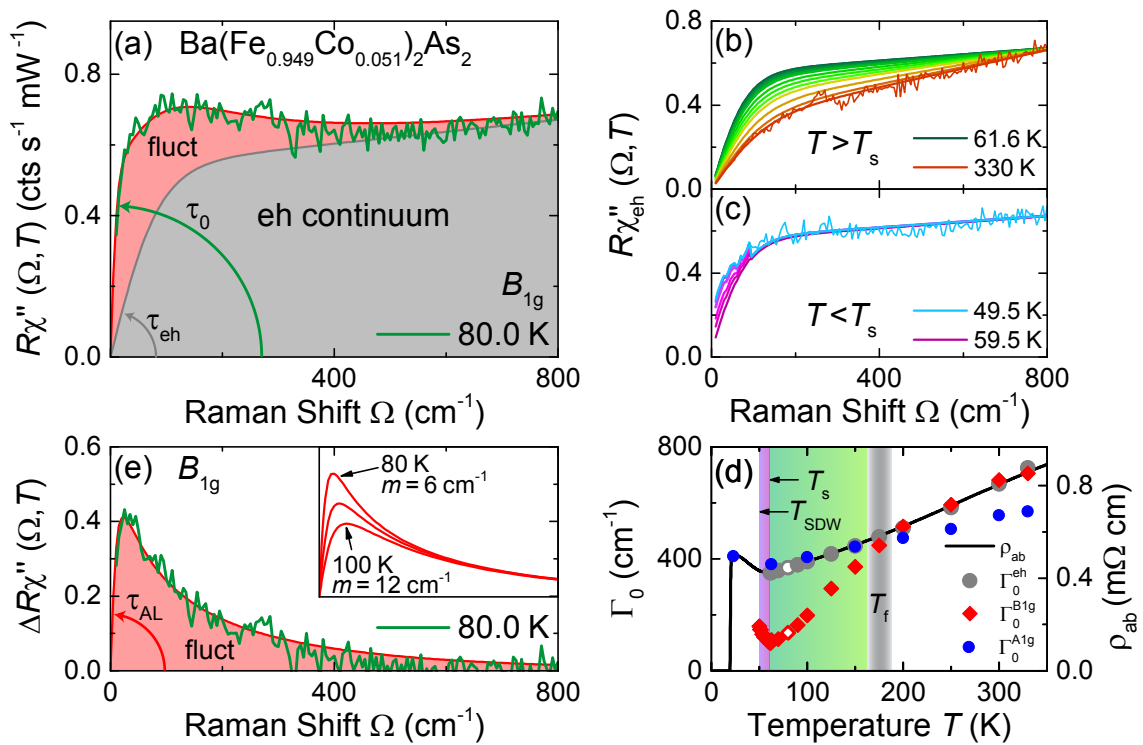


Figure 5.24: Analysis of the spectra in B_{1g} symmetry at a doping of $y = 0.051$ [73]. (a) shows the spectrum at 80 K as copied from Fig. 5.24. The contributions from fluctuation processes and electron-hole (eh) excitations are shaded in red and grey, respectively. The initial slopes of the total response τ_0 (green) and the electron-hole continuum τ_{eh} (grey) are illustrated by arrows. (b) and (c) show the model electron-hole continuum for all temperatures along with the spectra at 330 K and 49.5 K. (d) compares the static relaxation rates Γ_0 with the resistivity in ab plane [60]. Open symbols mark the results for 80 K. (e) Below T_f (green) and in the nematic phase (purple) fluctuations exist which can be described by AL processes. The inset demonstrates the enhancement of the AL fit with decreasing temperature for a constant electronic loop Λ_0^2 and decreasing mass m . Accordingly the initial slope τ_{AL} (red arrow) increases.

sition T_s and (b) shows the continuation in the nematic phase $T_{\text{SDW}} < T < T_s$ and below T_{SDW} . The nematic phase between T_{SDW} and T_s extends over a temperature range of 11.4 K here in comparison to 4.5 K for $y = 0.025$. As compiled in Table 3.2 the transition temperatures were determined to be $T_s = 60.9$ K and $T_{\text{SDW}} = 49.5$ K. Upon crossing these temperatures, the spectra exhibit qualitative changes. Starting from the spectrum at the highest temperature, 330 K, a continuous pile up of spectral weight towards T_s is observed. This enhancement progressively concentrates around smaller energies for lower temperatures. It is accompanied by the development of a new maximum below roughly 150 K, which accordingly moves towards lower energies with decreasing temperature. The maximal intensity is reached close to T_s . Below T_s , inside the nematic phase, the intensity quickly drops but the maximum stays nearly pinned at one energy [73]. The reduction of intensity continues even below T_{SDW} but the temperature dependence weakens. This is obvious from the spectra at 46 K and 49.5 K, which are nearly identical although they were recorded for temperatures differing already by 4.5 K. This evolution is identified with the continuous opening of the SDW gap, see App. 7.5.

In contrast to the strong temperature dependence in B_{1g} symmetry the spectra in A_{1g} symmetry, as presented in Fig. 5.23(c), exhibit a much weaker dependence. The spectra in B_{2g} symmetry of (d) show no change between T_s and 40 K above.

In analogy to the results in differently doped samples, the increase of the B_{1g} response on approaching T_s is attributed to a new scattering channel, projecting out fluctuations [72, 73, 124, 125]. This channel and the typical electron-hole continuum add up to the total spectrum in the range $T_{\text{SDW}} < T < T_f$, with T_f being the highest temperature where fluctuations can be observed by Raman scattering. For separating the two scattering channels a phenomenological model for the electron-hole continuum is subtracted from the total response. The remaining response can be compared to theoretical predictions for the response of fluctuations [108]. This strategy for the analysis was first used by Kretzschmar and coworkers [73].

For illustrating the analysis the spectrum at 80 K in B_{1g} symmetry is selected as shown in Fig. 5.24(a). First, the electron-hole continuum is modeled on the assumption that it smoothly evolves with temperature. The phenomenological function

$$R\chi''_{\text{eh}}(\Omega, T) = \alpha(T) \tanh\left(\frac{\Omega}{\gamma(T)}\right) + \beta(T)\Omega \quad (5.14)$$

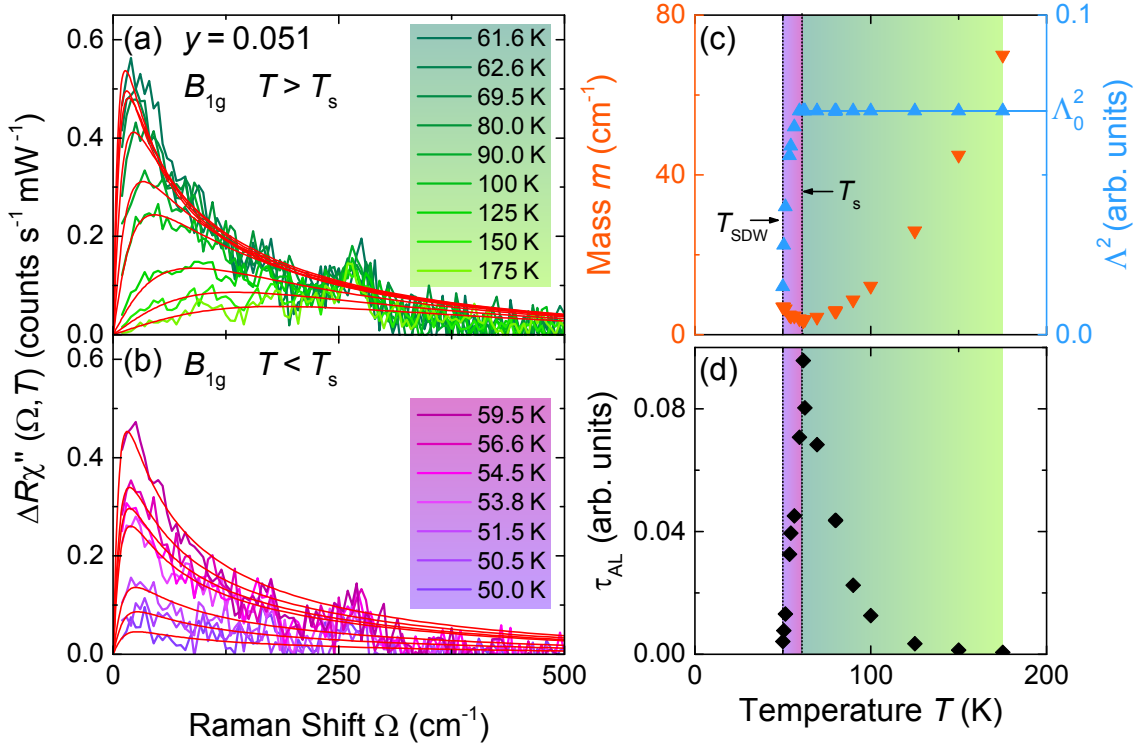


Figure 5.25: Fluctuation contribution for $y = 0.0051$ [73]. (a) and (b) show the fluctuation contribution along with fits by AL functions (red). (c) displays the two fitting parameters, mass m and the scaling factor Λ^2 . (d) presents the initial slopes of the AL fits.

is used for $T > T_s$ with $\alpha(T)$, $\beta(T)$ and $\gamma(T)$ depending linearly on temperature. For large Ω , this function converges to the linear approximation $\alpha(T) + \beta(T)\Omega$. As the contribution from fluctuations is expected to be small at large energies a linear function describes the continuum adequately. To determine the temperature dependence of $\alpha(T)$ and $\beta(T)$ the spectra at 330 K and 49.5 K are utilized as upper and lower bounds, respectively. The fluctuations are expected to be very weak at high temperatures and not present in the ordered SDW state below 49.5 K. The determination of $\gamma(T)$ is based on the resistivity measurements in the ab -plane [60]. The inverse initial slope τ_{eh}^{-1} of the electron-hole continuum is a measure for the resistivity [240],

$$\Gamma_0^{\text{eh}} \equiv \tilde{R}(T)\tau_{\text{eh}}^{-1}(T) \propto \rho_{ab}(T), \quad (5.15)$$

where $\tilde{R}(T) = R \int_0^\infty d\Omega \chi''(\Omega, T)/\Omega$ is a normalization factor which is only weakly temperature dependent in this case. To determine the temperature dependence of $\gamma(T)$, the static relaxation rates Γ_0 were extracted for the model continuum and for the total B_{1g} response. As the spectra cannot be obtained down to zero energy, it

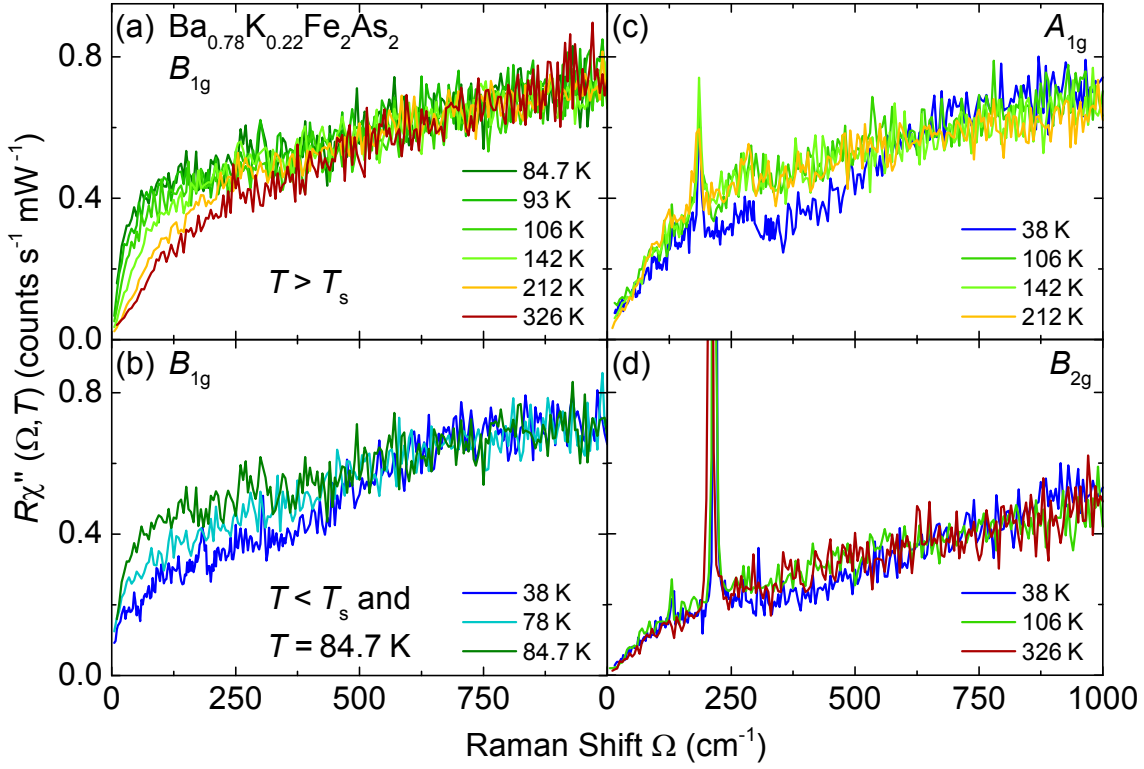


Figure 5.26: Raman spectra of $\text{Ba}_{0.78}\text{K}_{0.22}\text{Fe}_2\text{As}_2$ [74]. (a) and (b) show spectra in B_{1g} symmetry. (c) and (d) present the spectra in A_{1g} and B_{2g} symmetry, respectively.

is hard to directly extract the initial slope. Hence a more sophisticated approach was applied based on the memory-function method and a Kramers-Kronig transform [240, 241]. This method is described in Refs. [73, 124, 125, 134, 135, 240] and referred to in App. 7.6. Then $\gamma(T)$ is set in a way that $\Gamma_0^{\text{eh}}(T)$ matches the temperature evolution of the resistivity. If the same analysis is performed with the spectra in A_{1g} symmetry (after subtracting the phonons) it is found that $\Gamma_0^{A_{1g}}$ follows the resistivity. This shows that the A_{1g} spectra are dominated by the electron-hole continuum with a temperature dependence dictated by the change of the resistivity. The same is observed for B_{1g} above T_f . Below T_f the inverse initial slope of the entire spectra increasingly drops below Γ_0^{eh} [Fig. 5.24(d)].

Subtracting the continuum yields the contribution shown in Fig. 5.24(e). A fit with the function [108, 144]

$$\chi''_{\text{AL}}(\Omega) = \Lambda^2 \int_0^\infty dz [b(z - \Omega/2) - b(z + \Omega/2)] \frac{z_+ z_-}{z_+^2 - z_-^2} [F(z_-) - F(z_+)] \quad (5.16)$$

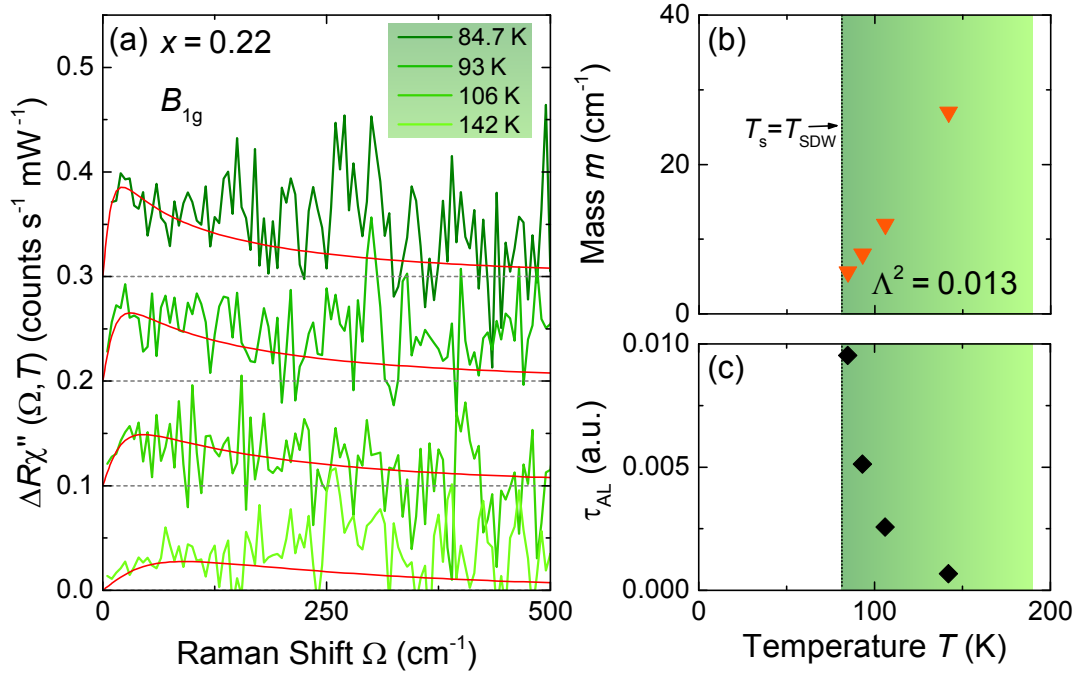


Figure 5.27: Fluctuation contribution and results for $\text{Ba}_{0.78}\text{K}_{0.22}\text{Fe}_2\text{As}_2$ [74]. (a) shows the fluctuation contribution along with fits by AL functions. (c) displays the two fitting parameters, mass m and scaling factor Λ^2 . (d) presents the initial slopes of the AL fits.

as derived from AL diagrams [108, 144] was performed, with the Bose function $b(z)$, $F(z) = [\arctan(\Omega_0/z) - \arctan(m/z)]/z$, and $z_{\pm} = (z \pm \Omega/2)[1 + (z \pm \Omega/2)^2/\Omega_0^2]$. Λ^2 is a scaling factor, m is the mass as defined in Eq. 2.5 and $\Omega_0 = 350 \text{ cm}^{-1}$ is a cutoff parameter given by a typical phonon frequency [108] and held constant for all doping levels. Eq. 5.16 describes the data very well in the whole temperature range $T_{\text{SDW}} < T < T_f$ as shown in Fig. 5.25. Minor deviations are observed only for temperatures close to T_s . The agreement supports the identification of the additional contribution with fluctuations.

From this analysis parameters such as the initial slope τ_{AL} [Fig. 5.24(d)], the mass m and Λ^2 [Fig. 5.25(c) and (d)] can be extracted. From Fig. 5.25(c) it is evident that a constant scaling factor Λ^2 reproduces the data above T_s . This constant value is labeled Λ_0^2 and quantifies the electronic loop (see Fig. 4.3). The only fitting parameter in this range is the mass m . It is observed that the mass decreases rapidly on approaching T_s and reaches a finite value at T_s . Inside the nematic phase the mass increases again. However, this increase is too weak to fully reproduce the reduction of intensity. The scaling factor Λ must account for this effect in the nematic phase. Note that the electronic loop Λ_0^2 is still expected to be constant. The analysis is

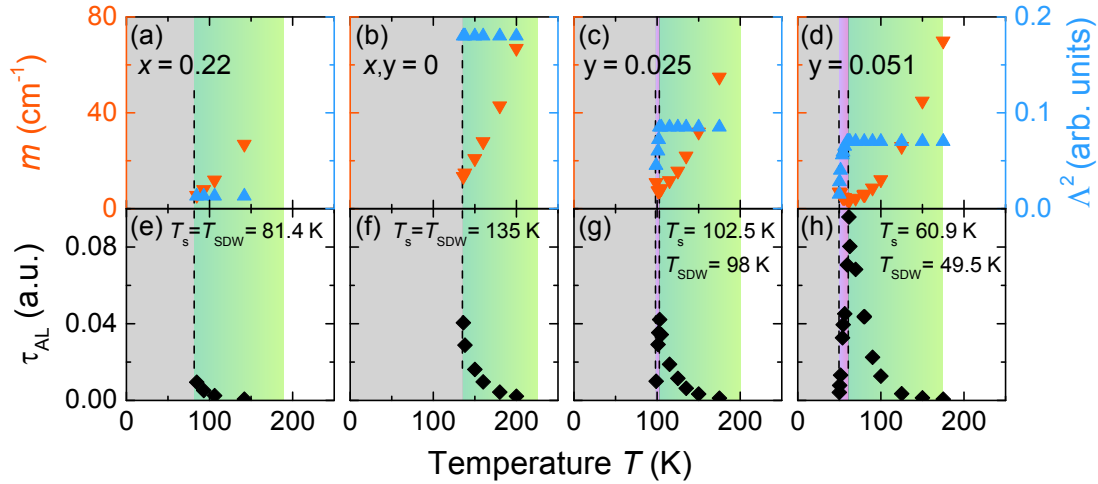


Figure 5.28: Temperature and doping dependence of the parameters extracted from the AL fitting functions [73, 74]. The results of the undoped ($x, y = 0$) and electron-doped ($y = 0.025$) samples are adopted from Refs. [73, 124, 125]. Vertical dashed lines indicate the structural (T_s) and SDW (T_{SDW}) transition temperatures. Grey, magenta and green shaded areas illustrate the SDW state, the nematic phase and the region where fluctuations are present, respectively. (a-d) Fluctuations are present above T_{SDW} characterized by the mass m (orange triangles, left scale) and the scaling factor Λ^2 (blue triangles, right scale). (e-h) presents the initial slopes τ_{AL} (black diamonds).

limited to the extraction of these values here, a physical interpretation will be given later when the data from different doping levels are collected.

A similar analysis is performed for the hole-doped $\text{Ba}_{0.78}\text{K}_{0.22}\text{Fe}_2\text{As}_2$. The spectra are compiled in Fig. 5.26 and normalized in the same way as those at $y = 0.051$. An excitation wavelength of 575 nm and a spectral resolution of 5 cm^{-1} was used. The structural transition temperature is $T_s = 81.4 \text{ K}$. On the hole-doped side no nematic phase is expected, according to neutron, x-ray diffraction, and magnetization measurements [66], hence $T_{\text{SDW}} = T_s$. In BKFA the sample surface degraded rapidly and data with sufficient counting statistics could be obtained only for a few temperatures. In spite of these complications the existence of fluctuations in the hole-doped case could be demonstrated.

The analysis of the fluctuations yields the results of Fig. 5.27. The contribution from the fluctuations is shown in (a). A reduction of the intensity by a factor of 5 with respect to $y = 0.051$ is observed. The fluctuations appear below $T_f = 190 \text{ K}$. The fitting procedure according to Eq. 5.16 was applied to collect values for m , Λ^2 , and the initial slopes τ_{AL} as a function of temperature, Fig. 5.27(b) and (c), respectively.

The investigation of the new samples confirmed the interpretation of the additional Raman response in B_{1g} symmetry in terms of fluctuations. This is in accordance to the results found for $x = y = 0$ and $y = 0.025$ [73, 124, 125]. Fig. 5.28 compiles the extracted parameters in the doping range from $x = 0.22$ to $y = 0.051$.

Based on these results, the following discussion will address new aspects of the fluctuations, going beyond the analysis performed in the PhD theses by B. Muschler [124] in the year 2012 and F. Kretzschmar [125] in 2015. They both advanced the analysis of fluctuations in terms of AL processes and analyzed the relaxation rates in detail. The thesis by F. Kretzschmar [125] additionally provides evidence for spin fluctuations and concentrates on the analysis of the nematic susceptibility. In this thesis, the spin fluctuation picture will be scrutinized taking into account the work by Gallais *et al.* [72] of 2016. They claim the fluctuations to be of charge origin. Furthermore, the increased temperature range of the nematic phase in the sample with $y = 0.051$ enabled a study of the temperature-evolution of the nematic order parameter which was not achieved so far. The analysis of the hole-doped sample with $x = 0.22$ made it possible to distinguish between intrinsic and doping-dependent properties of the fluctuations. Finally, the strength of the fluctuations is discussed as a function of doping and temperature.

5.3.2 Evidence for spin fluctuations

In the light of the findings in the superconducting state (Section 5.1 and 5.2), a discussion of spin-, charge-, and orbital-driven scenarios above T_{SDW} [100] is presented with a special focus on spin fluctuations. The following considerations are based on two aspects: The fact that fluctuations still appear inside the nematic phase, and the difference between scattering processes involving intra- and inter-band fluctuations (see Fig. 4.3), possessing small and large momenta, respectively. In this context, special attention is paid to the selection rules.

First, the interrelation between charge fluctuations and orbital fluctuations must be clarified [72]. The discussion is limited to ferro-orbital fluctuations here, antiferro-orbital fluctuations are addressed later. Furthermore, only fluctuations appearing in B_{1g} symmetry are considered. Hence these fluctuations are described by a B_{1g} form factor. To avoid confusion it is noted that some authors include Pomeranchuk [242] and quadrupolar [119, 163] fluctuations into their analysis. Both of them describe a B_{1g} -symmetric deformation of the band structure, similar to ferro-orbital fluctuations. For the present discussion they behave in analogy to ferro-orbital fluctuations and will thus not be addressed separately. Fig. 5.29 illustrates a ferro-orbital band

deformation along with the corresponding charge transfer. It is evident, that charge and ferro-orbital fluctuations in B_{1g} symmetry are interdependent and appear simultaneously [72, 243]. Hence they are referred to as “charge/orbital” fluctuations in the following.

To investigate the nature of the fluctuations, the Raman scattering processes are considered up to second order, as shown in Fig. 4.3. Analyzing these diagrams in terms of charge/orbital and spin fluctuations yields the following results: The first order diagram is limited to fluctuations with small momentum, thus charge/orbital fluctuations are possible, spin fluctuations with finite \mathbf{q} do not contribute. Another requirement is that the Raman vertex must have a sufficient overlap with the form factor of the fluctuations in terms of FS average. In the case of B_{1g} -symmetric charge/orbital fluctuations, the selection rules allow a finite response. In contrast to that, the selection rules in the AL diagrams do not depend on the symmetry of the fluctuations but on their wave vector, incorporated in the electronic loops (Eq. 4.6). For fluctuations with small momenta, the AL response is approximately determined by the FS average of the Raman vertex $\langle\gamma(\mathbf{k})\rangle$ entailing cancellation in all symmetries including A_{1g} symmetry due to its s^\pm form factor [162]. Hence, charge/orbital fluctuations with $\mathbf{q} \approx (0, 0)$ do not contribute. Spin fluctuations with finite momenta $\mathbf{q}_c \in \{(\pm\pi, 0), (0, \pm\pi)\}$ are possible. A detailed discussion of the selection rules can be found in App. 7.1 based on Refs. [73, 125, 145]. It was pointed out, that the second-order AL diagrams contribute, if spin fluctuations are present, whereas the first order diagrams project out charge/orbital fluctuations. A quantitative comparison would be necessary but is beyond the scope of this thesis.

One step towards that quantitative analysis is made by Gallais and Paul [72]. They found that the first-order diagram does not contribute unless a finite impurity-

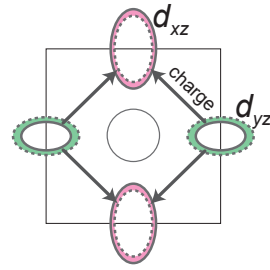


Figure 5.29: Relation between ferro-orbital and charge fluctuations. The figure shows the intertwining of charge and ferro-orbital order. For simplicity the whole electron pocket is of d_{xz}/d_{yz} character. Pink shows a pocket that lowers its energy and thus gathers electrons from the pocket that increases its energy (green). This causes, or is induced by a charge transfer from green to pink. The change of band energies constitutes ferro-orbital order. The transfer of charges is referred to as charge order. It is evident that these two ordering phenomena cannot occur separately.

scattering rate is introduced. Hence the required rate of impurity scattering is estimated in the case of the first-order diagram describing charge/orbital fluctuations. Gallais and Paul calculated the peak frequency of the fluctuations to be at [72]

$$\Gamma_{\text{charge/orbital}}^{\text{peak}} = \frac{r_0}{(r_0 + c_3)\tau_i} \quad (5.17)$$

with $r_0 = a/\xi$ depending on the lattice constant a and the correlation length ξ and $c_3 \propto g_0$ the fluctuation-electron coupling. At high temperatures the bare impurity scattering rate $\Gamma_i = \tau_i^{-1}$ can be obtained directly from the peak frequency of the fluctuations: At $T \lesssim T_f$, ξ approaches its smallest value $\xi \rightarrow a$ and thus $r_0 \rightarrow 1$. Furthermore c_3 is expected to be small as g_0 decays like $1/T^4$ [99]. Thus $\Gamma_{\text{charge/orbital}}^{\text{peak}} \approx \Gamma_i$ for $T \lesssim T_f$. The experiment locates the peak at about $100\text{--}150\text{ cm}^{-1}$ for $y = 0.051$. This lies by a factor of roughly 3 above the superconducting pair-breaking peak 2Δ . Such a high impurity scattering rate would quench the pair-breaking response completely [148, 149, 244–246]. However, a pair-breaking peak is clearly observed in the experiment which argues against charge/orbital fluctuations and in favor of spin fluctuations to dominate the Raman response. It is noted that Ref. [72] explicitly includes scattering caused by impurities. However, they further state that τ_i only provides a finite lifetime for the electronic excitations. Hence strong interactions could also be included in τ_i . Yet a thorough investigation goes beyond the scope of this thesis.

The second argument against charge/orbital fluctuations is based on the fact, that ARPES measurements show orbital order to be nearly fully established below T_s for a twinned crystal of doping $y = 0.025$ [82]. The fact that fluctuations are expected to appear only above an ordered state but are clearly observed below T_s in our experiment provides another argument against the scenario where charge/orbital fluctuations dominate.

The possibility for antiferro-orbital fluctuations with $\mathbf{q}_c \in \{(\pm\pi, 0), (0, \pm\pi)\}$ is also excluded to be the dominant part in the AL diagrams as there is no antiferro-orbital ordered state found in the IBSs. The observation of ferro-orbital order [82] argues against the existence of antiferro-orbital order as both orders are orthogonal and thus cannot coexist. Hence, antiferro-orbital fluctuations are very unlikely to exist. Although the presented Raman study is no “smoking-gun” experiment, two pieces of evidence against charge/orbital fluctuations were presented and a conclusive description in the case of spin fluctuations was given. Hence, the analysis of the data will be continued on this premise.

5.3.3 Discussion

The parameters extracted via the AL fits will now be discussed as a function of doping and temperature. From these parameters, a nematic order parameter can be defined. Furthermore, the correlation length will be analyzed and finally the strength of the fluctuations will be examined.

In this context physical questions are addressed as to the order of the phase transitions, the possibility of a QCP and the asymmetry between the electron- and hole-doped sides in terms of fluctuations.

Nematic order

To investigate how nematic order is established below T_s , a nematic order parameter φ_{exp} will be defined from the experiment and compared to the theoretically obtained order parameter φ_{th} from Ref. [100]. For this goal the temperature dependence of

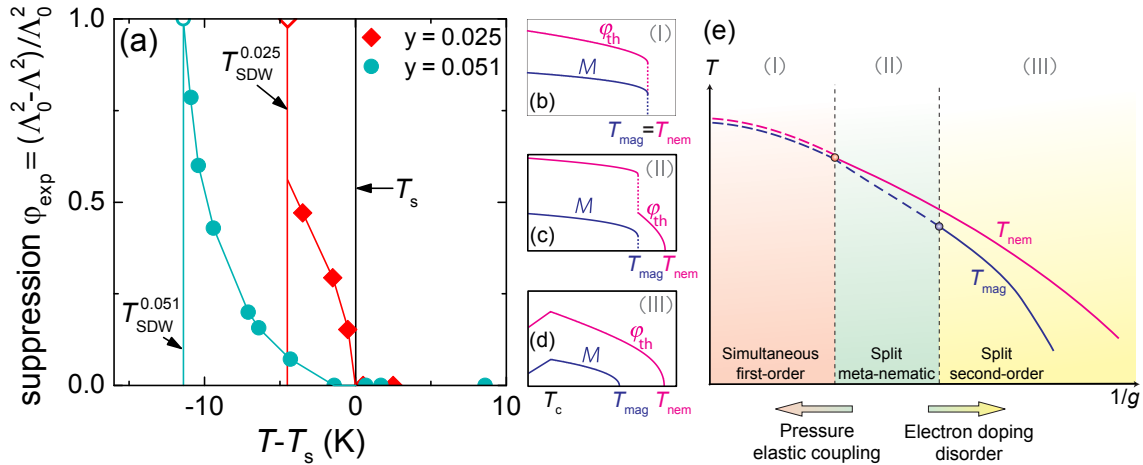


Figure 5.30: Suppression of the fluctuation contribution inside the nematic phase. (a) shows the suppression φ_{exp} for the Co-doping levels $y = 0.025$ and $y = 0.051$. The respective transitions are indicated by vertical lines. Open symbols illustrate full suppression at T_{SDW} . Solid lines are guides to the eye. (b-d) compile the theoretically obtained nematic (φ_{th}) and magnetic (M) order parameters for three different regions defined in (e). The theoretical results are adopted from Ref. [100]. T_{mag} and T_{nem} have to be identified with our T_{SDW} and T_s , respectively. The dashed and solid lines mark first- and second-order phase transitions.

the fluctuations is utilized.

The observed fluctuations reach their maximal spectral weight at T_s and continuously weaken upon decreasing the temperature until they vanish at T_{SDW} . As

nematic fluctuations cannot exist in a fully nematically ordered state, the suppression of the fluctuations in the range $T_{\text{SDW}} < T < T_s$ measures the degree of nematic order. The SDW state implies full nematic order [Fig. 2.8(c3)] and thus no fluctuations are present below T_{SDW} . As the nematic order parameter is associated with the suppression of the fluctuations it can be quantified by $\varphi_{\text{exp}}(T) \equiv (\Lambda_0^2 - \Lambda^2(T))/\Lambda_0^2$. This parameter is 0 (no suppression) above T_s , it increases in the nematic phase and stays at 1 (full suppression) in the SDW state.

With this definition the phase transitions at T_s and T_{SDW} can be described by their order. $\varphi_{\text{exp}}(T)$ is shown in Fig. 5.30(a) for $y = 0.025$ and $y = 0.051$, where the structural transition is separated from the SDW transition. $\varphi_{\text{exp}}(T)$ exhibits a discontinuity only for $y = 0.025$ at T_s . Here, a first order phase transition is present, the other transitions in Fig. 5.30(a) are of lower order. In the case of $x = 0.22$ and $x = y = 0$, where both transitions coincide a discontinuous increase of φ_{exp} from 0 to 1 and hence a first order transition appears at $T_s = T_{\text{SDW}}$.

Further insight is gained from the comparison with the theory of Fernandes and coworkers [100], where the order of the nematic and magnetic phase transition is studied as a function of elasto-magnetic coupling, doping and disorder. The theory is based on a spin-driven scenario, where the fluctuations interact with each other via electrons. The indirect fluctuation-fluctuation interaction g is responsible for the separation of T_s and T_{SDW} and the appearance of a nematic phase. The magnetic and structural phase transitions can be separated into three regions, as shown in Fig. 5.30(b-d) with a compilation in (e). In region (I), where electron doping is small, the transition temperatures merge $T_s = T_{\text{SDW}}$, and the transition is first order. Both φ_{th} and the SDW order parameter M change discontinuously. With increasing electron doping, region (II) is reached: A moderate split is present here and the nematic transition turns into a second-order transition (no discontinuity), whereas the SDW transition stays first order. In region (III) both transitions are second order and none of the corresponding order parameters has a discontinuity.

The comparison of $\varphi_{\text{exp}}(T)$ and $\varphi_{\text{th}}(T)$ shows that $x = 0.22$ and $x = y = 0$ are located in region (I). A simultaneous first order transition is present here. For $y = 0.025$ it is observed that $\varphi_{\text{exp}}(T)$ is strikingly similar to $\varphi_{\text{th}}(T)$ of region (II). The results of $y = 0.051$ are best described by region (III). Although the order parameters differ between theory and experiment, the largely split second order transitions describe the experimentally obtained results adequately.

In summary it was found that (i) a nematic order parameter can be extracted from the fluctuations, (ii) the nematic order is not established abruptly at T_s but increases

smoothly towards T_{SDW} , and (iii) a spin-driven scenario [100] is in agreement with the experimental results. Here, the scaling factor Λ^2 was used to investigate the nematic phase. Above T_s , where $\varphi_{\text{exp}} = 0$ the mass gives valuable information about the fluctuations.

Deviations from mean-field theory

In mean-field theory all temperature-dependent quantities such as the correlation length ξ or, equivalently, the mass $m \propto \xi^{-2}$ are predicted to obey characteristic power laws close to the transition. For instance the correlation length varies as $\xi(T) \propto (T - T_0)^{-\nu}$ with the critical exponent $\nu = 1/2$ and a transition at T_0 [74, 108, 247]. The values $m(T)$ for four different doping levels are plotted in Fig.

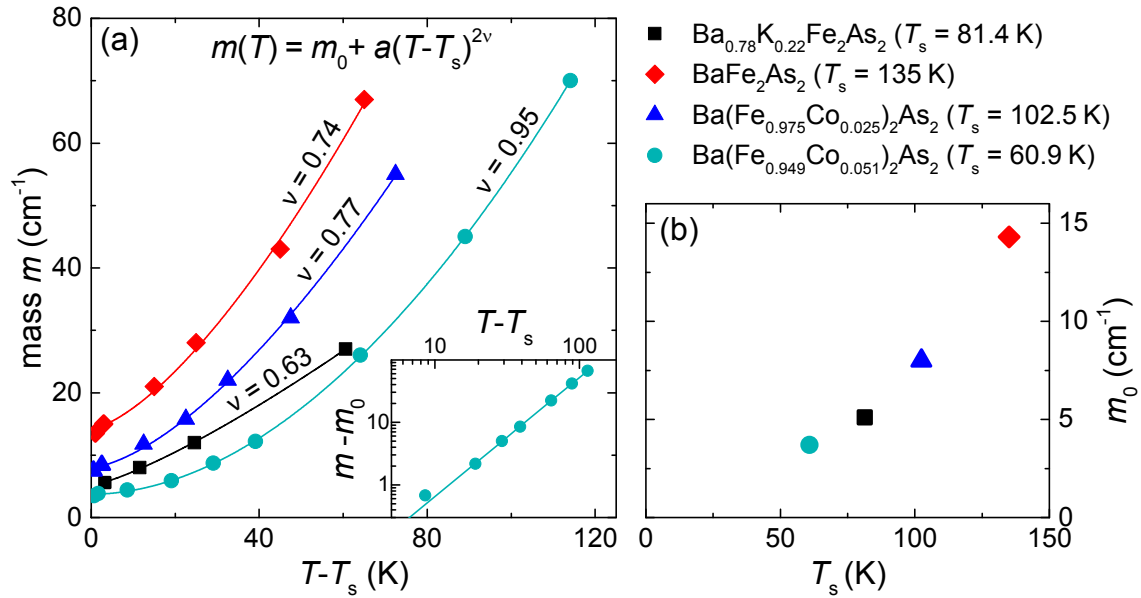


Figure 5.31: Dependence of the mass on doping and temperature. (a) compiles all the masses obtained from the AL fits. Their temperature dependence follows Eq. 5.18. The inset shows the data of $y = 0.051$ with double-logarithmic scales. The first point is at 8.6 K above T_s as the error bars of the mass difference $m(T) - m_0$ below that temperature are too large. (b) shows the offset m_0 which is monotonically related with T_s .

5.31 along with the function

$$m(z, T) = m_0(z) + a(z)(T - T_s(z))^{2\nu(z)} \quad (5.18)$$

used to describe the temperature dependence. Eq. 5.18 facilitates the extraction of the mass offset at T_s , $m_0(z)$, and the critical exponent $\nu(z)$ as a function of doping z .

Fig. 5.31(a) shows that ν depends monotonically on doping. For hole doping a value of $\nu = 0.63$ is obtained, for electron doping ν varies between 0.74 and 0.95. Hence the mean-field expectation is nearly reached for hole doping, whereas a substantial deviation by a factor of 2 is observed for electron doping. This asymmetry between electron and hole doping is unexpected and remains as an open question for further studies.

Another unexpected observation is the offset m_0 of the mass. When approaching a transition from higher temperatures, the correlation length is expected to diverge. Hence the mass should decrease down to zero instead of saturating at m_0 . However, a finite m_0 is observed for all doping levels, which monotonically depends on T_s as illustrated in Fig. 5.31(b). Due to the dependence on T_s , this aspect is considered to be an intrinsic property of the spin fluctuations.

To explain the offset m_0 the Ornstein-Zernike propagator of Eq. 2.5 is analyzed. In the spirit of Dyson's equation, the propagator can be renormalized by a self-energy correction, which effectively yields the mass renormalization $m \rightarrow m + m_0$. Hinojosa and coworkers [156] showed that $m_0 = g\Pi$ with the electron-fluctuation coupling g and the electron-hole bubble Π . Calculating an electron-hole bubble yields the Lindhard susceptibility, a measure for the nesting condition. In this case the nesting vector for the SDW state is \mathbf{q}_c . Within this framework, the experiment shows that the nesting condition, which is quantified by m_0 , improves with rising T_s , as expected.

The question arises, how m_0 develops for $T_s \rightarrow 0$. Fig. 5.31(b) shows that m_0 extrapolates approximately to zero. $m_0 \rightarrow 0$ corresponds to a diverging correlation length and defines a QCP [74]. The dependence of m_0 on T_s suggests, that this QCP appears both in the electron- and hole-doped case, whenever $T_s = 0$. If this is true, quantum spin fluctuations above this QCP could mediate superconductivity and lead to a superconducting dome around the QCP.

Quantification of the fluctuations

Inspired by this possibility the strength of the fluctuations will now be quantified and studied as a function of doping and temperature. Here, we use the initial slope [73, 73, 74, 145] of the fluctuations τ_{AL} [Fig.5.28(e-h)] to measure their strength. In addition, proper normalization procedures must be applied to isolate intrinsic effects of the fluctuations and eliminate side effects such as the doping dependence of the (Raman-specific) electronic loop Λ_0^2 and different surface qualities. The B_{1g} spectra of different doping levels were already normalized to the respective BFA

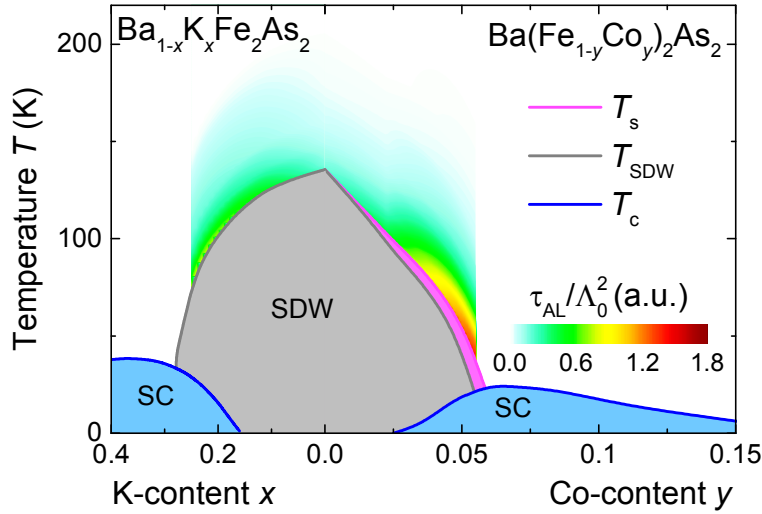


Figure 5.32: Magnitude of the bare fluctuations. The initial slopes from the AL-fits, normalized by the electronic loop Λ_0^2 are depicted as a color scale above the SDW and nematic phase. An interpolation procedure within the doping range from $x = 0.22$ to $y = 0.051$ is used.

spectra. However, this normalization is insufficient to describe all side effects. It is obvious from Fig. 5.28(a-d) that the electronic loops Λ_0^2 are still dependent on doping. Khodas and Levchenko [229] found a relation between Λ_0^2 and the doping dependence of the FS. In coincidence with their results Λ_0^2 is largest for $z = 0$ and decreases for both electron and hole doping. Hence the adequate measure for the strength of the fluctuations is $\kappa(z, T) \equiv \tau_{\text{AL}}(z, T)/\Lambda_0^2(z)$.

The results are presented in Fig. 5.32. $\kappa(T = T_s)$ is smallest for $z = 0$ and increases with increasing electron and hole-doping. The question arises if the asymmetry between electron and hole doping is reflected by the doping dependence of the fluctuations. To answer this question the dependence of the fluctuations will be presented as a function of T_s rather than z . For this purpose, Fig. 5.33(a) shows κ as a function of $T - T_s$. It turns out, that the temperature dependencies $\kappa(z, T - T_s)$ only differ by a single factor per doping. This factor normalized to $\kappa(z = 0, T - T_s)$ is called the enhancement $\eta(z) \equiv \kappa(z, T - T_s)/\kappa(z = 0, T - T_s)$. $\eta(z)$ expressed as a function of $T_s(z)$ is plotted in Fig. 5.33(b). The figure shows a monotonic, nearly linear dependence of η on T_s . This monotonic dependence of the results from both hole- and electron-doped samples argues against an asymmetry between electron and hole doping in terms of fluctuations.

To complete the doping-dependent analysis of the fluctuations, the onset temper-

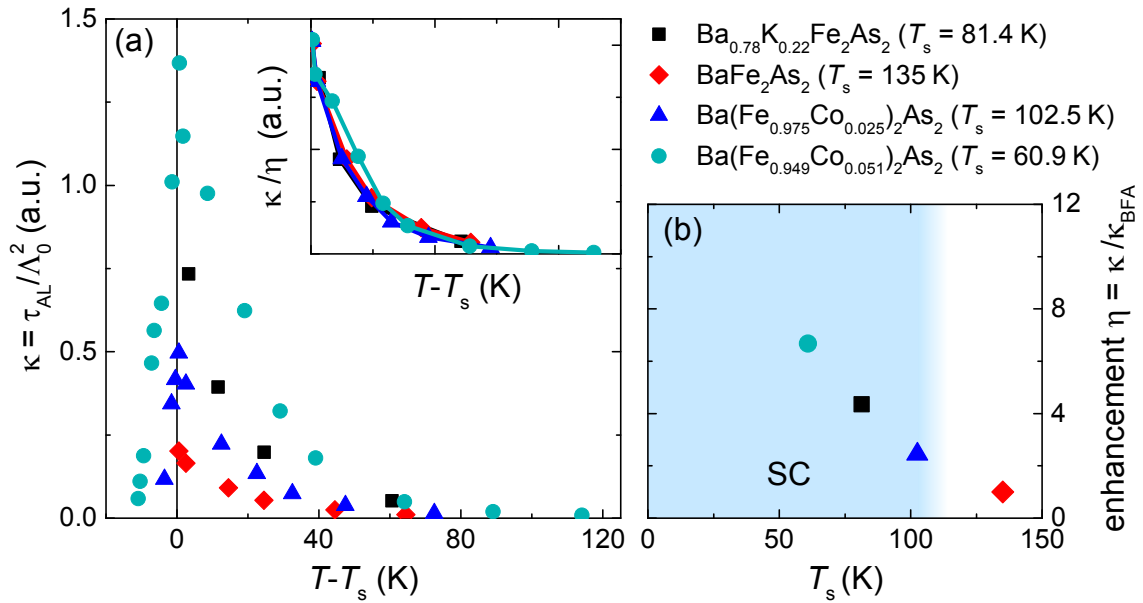


Figure 5.33: Enhancement of the fluctuations. (a) shows the normalized initial slopes. The inset demonstrates that the normalized initial slopes can be scaled onto each other by a single factor per doping. (b) compiles these factors. The superconducting region is shaded in blue. The enhancement of the undoped compound is set to 1.

ature $T_f(z)$ is shown in Fig. 5.34. Here the data obtained by B. Muschler for $y = 0.055$, $y = 0.061$ and $y = 0.085$ [124] are included. Extrapolating $T_f(z)$ along z determines a roof-shaped area below which the existence of fluctuations might be expected. For the Co-doped side this roof area covers the whole superconducting region, for K-doping a similar result is obtained, however, more measurements are required here to make a profound statement.

In summary, fluctuations were found in the hole- and electron-doped region below a doping-dependent temperature T_f . The strength of the fluctuations increases with decreasing T_s with the strongest enhancement occurring at $T_s = 0$, i.e. at the putative QCPs of both the hole- and electron-doped sides.

In the spirit of these results, one could end up with the following speculations: Either the fluctuations are the only reason for pairing [248] or at least boost T_c close to the QCP [249]. In the first scenario superconductivity in BKFA and BFCA is mediated by the exchange of repulsive quantum spin fluctuations which are strongest right above the QCPs, defining optimal doping. The fluctuations decay for higher doping where superconductivity vanishes more or less with the fluctuations. In the second scenario a yet unidentified interaction leads to a moderate T_c in a wide range of doping and the fluctuations above the QCP enhance T_c around optimal doping.

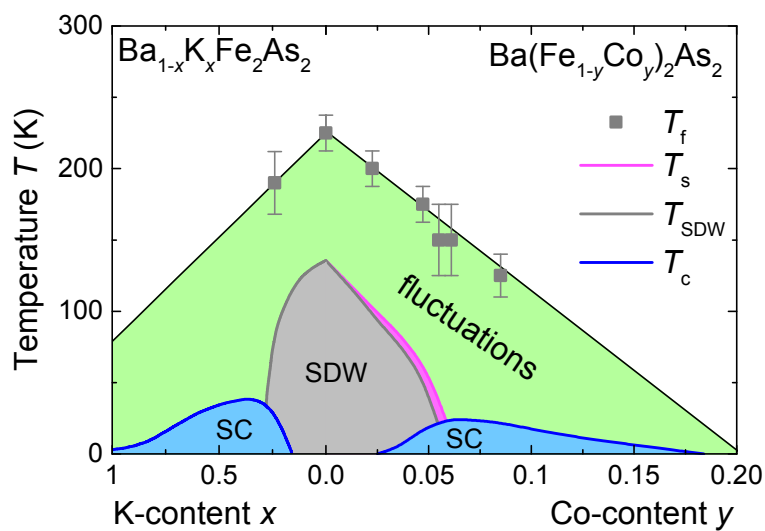


Figure 5.34: Extended region of fluctuations. The linear extrapolation of T_f toward high doping, separately performed in the hole- and electron-doped parts of the phase diagram yield large areas (light green) below a roof-shaped boundary, below which the fluctuations occur. Note that this roof area completely covers both superconducting regions.

5.4 Phonon anomaly in the vicinity of a quantum critical point

A completely different way of probing interactions in the vicinity of a QCP, e.g. quantum fluctuations, may be provided by optical phonon modes [250, 251].

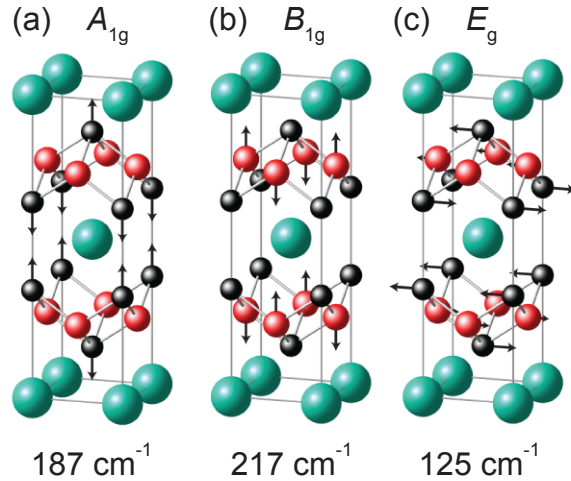


Figure 5.35: Eigenvectors of the optical phonon modes. The eigenvectors are illustrated by black arrows according to Ref. [166].

The corresponding eigenvectors are depicted in Fig. 5.35(a-c).

The B_{1g} mode is close to 217 cm^{-1} for low temperatures. This mode is described by an oscillation of the Fe atoms along the c -axis [166]. The oscillation of the As atoms along the c -axis corresponds to the phonon in A_{1g} symmetry close to 187 cm^{-1} . The frequency of this phonon is doping independent. Furthermore, one of the two in-plane E_g shear modes was observed in a range from 120 cm^{-1} to 134 cm^{-1} .

The evolutions of the frequency and line width (FWHM) of the B_{1g} phonon as a function of doping are presented in Fig. 5.36(b-c). The frequency and FWHM were extracted by applying a Voigt function to the spectra in a narrow range around the phonon (see App. 7.7). Both the position and the width vary nonmonotonically. The slight hardening and the decrease of the width with increasing doping inside the SDW state is in agreement with other Raman experiments where the SDW state was investigated in detail [202, 252]. For higher doping levels the peak position of the

The phonon modes were measured in the normal and superconducting state of BKFA in the doping range $0.22 \leq x \leq 0.70$, see Fig. 5.8. In contrast to the previous sections, where the 1Fe unit cell was used throughout, the adequate cell to describe the phonon modes is the crystallographic unit cell. Hence, the out-of-phase vibration of the Fe atoms appears now in the proper B_{1g} symmetry as opposed to B_{2g} symmetry in the 1Fe unit cell used for electronic excitations. Three optical phonon modes of A_{1g} ,

phonon shifts towards lower energies and arrives at a minimum for $x = 0.40$ [253]. The maximal softening is observed at optimal doping ($x = 0.40$) and visible already

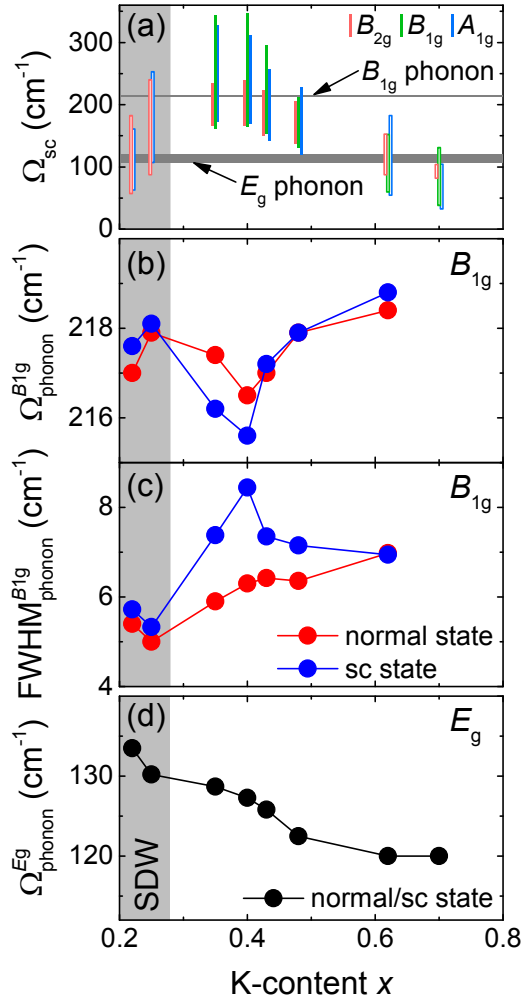


Figure 5.36: Doping dependence of the optical phonon modes. The data of (a) are a copy of Fig. 5.9 with B_{1g} and B_{2g} flipped since the crystallographic unit cell is used here. (b) and (c) show the peak positions and FWHM of the B_{1g} phonon, respectively. (d) displays the peak positions of the E_g phonon as a function of doping. Due to the low intensity of the E_g phonon the difference in position between superconducting and normal state is below the resolution of about 1 cm^{-1} . Thus they are not plotted separately.

in the normal state [Fig. 5.36(b)]. In the superconducting state the renormalization becomes stronger. The FWHM shows a continuous increase with doping in the normal state with a weak hump around optimal doping [Fig. 5.36(c)]. In the superconducting state the FWHM increases substantially in the range $0.35 \leq x \leq 0.48$ and the maximum is reached again at optimal doping.

This broadening can be explained if one considers the pair-breaking peak in the B_{1g}

symmetry (with respect to the crystallographic unit cell) as illustrated by vertical green bars in Fig. 5.36(a). For doping levels in the magnetic phase the B_{1g} spectra do not show a pair-breaking peak. On the other hand, for $x = 0.62$ and $x = 0.70$ the energy region of pair breaking is too far below the phonon energy of 217 cm^{-1} . The energies of phonon and gap are similar just around optimal doping. New scattering channels open up due to the continuum above 2Δ resulting in the observed linewidth broadening [254–258]. Consequently, this broadening decreases when the pair-breaking peak moves away from the phonon energy.

The frequency shift in the superconducting state with respect to that in normal state can be explained as well. Calculations show, that in terms of frequency, the phonon is repelled by the pair-breaking peak [255, 256, 259]. Hence for $\Omega_{\text{phonon}} < \Omega_{\text{PB}}$ the phonon frequency is pushed down, whereas for $\Omega_{\text{phonon}} > \Omega_{\text{PB}}$, its frequency increases. In fact, this effect is observed in the whole doping range with Ω_{PB} being defined by the pair-breaking peak in B_{1g} symmetry. Yet this effect is weak as the maximal softening lies below 0.5%.

A doping-dependent softening already appears above the superconducting transition. As the dip is centered at optimal doping, it is tempting to assume that this effect originates from an interaction, which is closely related to superconductivity, already existing above T_c . Yet a quantitative statement requires a calculation that describes the renormalization of the phonon energy in the presence of various interactions [260]. A renormalization of this kind must obey B_{1g} symmetry in the limit of small momenta q . In terms of Fe $3d$ orbitals, there are only two possible transitions which are not orthogonal to the B_{1g} symmetry and thus can couple to B_{1g} phonons: This is (i) the transition from d_{xz} to d_{yz} with a symmetry obeying the functional form xyz^2 , and (ii) from $d_{3z^2-r^2}$ to d_{xy} and vice versa. Note that both transitions have the common form factor xy which reflects B_{2g} symmetry in the 1 Fe unit cell and B_{1g} symmetry in the crystallographic one. Both transitions contain Fe orbitals with a z -component, oriented out of the Fe-As plane. These orbitals experience a strong influence from the Fe oscillation. They are alternately stretched and compressed, whereas the in-plane orbitals are modulated only quadratically with the Fe displacement.

Another doping dependence is observed for the shear mode in E_g symmetry. This mode softens monotonically with increasing doping as plotted in Fig. 5.35(c) by as much as 14 cm^{-1} (10%). In addition, a small hump around optimal doping is observed which hints towards an additional impact of the QCP. The large softening could be related to the doping dependence of the lattice parameters and bond

angles. With increasing hole doping, a (and concomitantly the Fe-Fe distance) decreases whereas c increases. Accordingly, the As-Fe-As bond angle decreases from approximately 110° to 108° [261]. In the tetrahedral structure of the FeAs layers, the antiparallel in-plane eigenvectors of the Fe and As oscillations [Fig. 5.35(c)] can be projected into directions along and perpendicular to the Fe-As bonds. With decreasing bond angles the perpendicular projection increases and the parallel one decreases. As the orbitals are modulated linearly with a parallel and quadratically with a perpendicular displacement, the change of bond angles could result in the softening of the E_g mode with doping.

In summary, this analysis demonstrated the existence of a phonon anomaly around optimal doping, predominantly observed for the B_{1g} phonon, which appears already in the normal state and becomes more pronounced in the superconducting state. It was shown that a few interactions can induce the renormalization close to optimal doping. This may open a window towards probing interactions above a QCP which may be related to superconductivity but are not limited to temperatures below T_c .

Chapter 6

Summary

This thesis covers the study of competing pairing channels in iron-based superconductors and the investigation of critical fluctuations above the spin-density-wave phase. The experimental study was performed by electronic Raman scattering on hole- and electron-doped samples derived from the mother compound BaFe_2As_2 . The theoretical analysis is based on a phenomenological model and a comparison between experiments and the results from a functional renormalization group (fRG) study and a spin-fluctuation model as obtained on the basis of a random-phase approximation (RPA).

In optimally doped $\text{Ba}_{0.6}\text{K}_{0.4}\text{Fe}_2\text{As}_2$ Bardasis-Schrieffer (BS) excitons were studied in the superconducting state along with gap excitations using symmetry-resolved Raman scattering. The experiments demonstrated the existence of a weakly momentum-dependent gap on the electron bands and the $d_{x^2-y^2}$ -wave character of the BS mode. An analysis of the temperature-dependence of the response identified the pair-breaking peak of the superconducting ground state and the subdominant d -wave interaction at the origin of the BS mode. The experiments provided evidence for competing pairing interactions of similar strength. A phenomenological calculation of the response was found to be in agreement with the experiment. This enabled the extraction of the momentum-resolved structure of the subdominant interaction, providing indications for an orbital-dependent inter-band nesting scenario.

These results motivated a systematic, doping-dependent study of the superconducting state in $\text{Ba}_{1-x}\text{K}_x\text{Fe}_2\text{As}_2$ in the range $0.22 \leq x \leq 0.70$. BS modes were clearly identified in a range close to optimal doping, $0.35 \leq x \leq 0.48$. Samples of several doping concentrations showed, that two subdominant d -wave interactions are present. As a function of increasing doping a continuous increase of the subdominant coupling strengths with respect to the leading s -wave strength was observed,

reaching up to 90%. Both results agree well with an fRG analysis which includes all interactions on equal footing. RPA yields similar results even though only the spin channel is dominant in this model. The agreement of experiment, fRG and RPA led to the conclusion that spin fluctuations dominate the pairing.

Inspired by this result, critical fluctuations above the spin-density wave phase were investigated in $\text{Ba}_{0.78}\text{K}_{0.22}\text{Fe}_2\text{As}_2$ and $\text{Ba}(\text{Fe}_{1-y}\text{Co}_y)_2\text{As}_2$. The selection rules, the spectral shape and the persistence of the fluctuations in the nematic phase argue for spin rather than orbital or charge fluctuations. The comparison of the experimental results with a theoretical model description based on higher-order fluctuation-exchange processes enabled the extraction of the temperature and doping dependence of the nematic order parameter, the correlation length and the spectral weight of the fluctuations. The order of the transitions into the spin-density-wave and the nematic phase could be determined. It was found that nematic order is established continuously and not abruptly below the structural transition temperature. The investigation of the correlation length indicated the existence of a quantum critical point. The analysis of the strength of the fluctuations did not reflect the asymmetry between hole and electron doping. Rather a universal dependence on the structural transition temperature was found irrespective of hole and electron doping. If the structural transition temperature was decreased as a function of doping an increase of the strength of the fluctuations was detected inferring the existence of a quantum critical point close to the doping level with the highest superconducting transition temperature T_c .

Along with the electronic properties the doping dependence of optical phonons was investigated. The in-plane shear mode of the Fe and As atoms with E_g symmetry decreases monotonically upon doping roughly reflecting the change of the lattice parameters and bond angles. The out-of-plane Fe phonon with B_{1g} symmetry depends non-monotonically on doping, and the energy and the width have a minimum and, respectively, maximum at optimal doping. The anomaly is clearly observable already in the normal state and becomes stronger below T_c indicating that interactions intertwined with Cooper pairing couple to the phonons.

Chapter 7

Appendix

7.1 Selection rules in the case of spin fluctuations

The Raman selection rules for AL processes as described in Eq. 4.6 will be applied to spin fluctuations with the critical vectors $\mathbf{q}_c \in \{(\pm\pi, 0), (0, \pm\pi)\}$ [73, 108, 125, 145]. A finite response can only be expected in symmetries μ where $\sum_{\mathbf{k}_0} \gamma_\mu(\mathbf{k}_0)$ is finite with $\gamma_\mu(\mathbf{k}_0)$ being the Raman vertex at the hot spot \mathbf{k}_0 .

The case for $\mathbf{q}_c = (\pi, 0)$ is illustrated in Fig. 7.1. Four hot spots are highlighted in

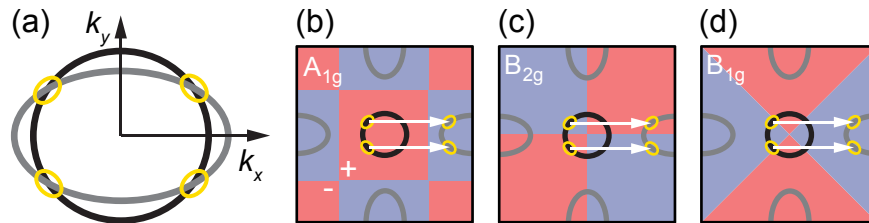


Figure 7.1: Selection rules of AL processes adopted from Refs. [73, 125]. (a) The critical vector $\mathbf{q}_c = (\pi, 0)$ defines the hot spots at \mathbf{k}_0 on the FS. For illustration, the electron pocket (black) is shifted on top of the hole pocket (grey) by $(-\pi, 0)$. The intersections (yellow ellipses) mark the hot spots. (b) illustrates the signs of the s^\pm Raman vertex in A_{1g} symmetry with positive (red) and negative (blue) areas. Fig. 5.3 shows that the s^\pm symmetry is preferred here. (c,d) Signs of the first order B_{2g} and B_{1g} Raman vertices. A selection of hot spots (which is sufficient for the analysis) at \mathbf{k}_0 is shown along with the connecting vectors \mathbf{q}_c .

each symmetry A_{1g} , B_{2g} , and B_{1g} . The summation as in Eq. 4.6 yields a cancellation in A_{1g} and B_{2g} symmetries as the Raman vertex changes sign at different hot spots. The sign is preserved only in B_{1g} . Hence, in the case of spin fluctuations, a response from AL processes can only be expected in B_{1g} symmetry.

7.2 Resonances in $\text{Ba}_{0.6}\text{K}_{0.4}\text{Fe}_2\text{As}_2$

The effective mass approximation as used in Eqs. 5.1, 5.3, and 5.2 is only valid if resonances do not play a significant role. Resonances are likely to occur in iron-based superconductors having a bandwidth of about 3 eV [98, 201] (visible light is ranging from 1.8 eV to 3.2 eV). To study the influence of resonances for the Raman spectra of $\text{Ba}_{0.6}\text{K}_{0.4}\text{Fe}_2\text{As}_2$ measurements with different excitation wavelength were

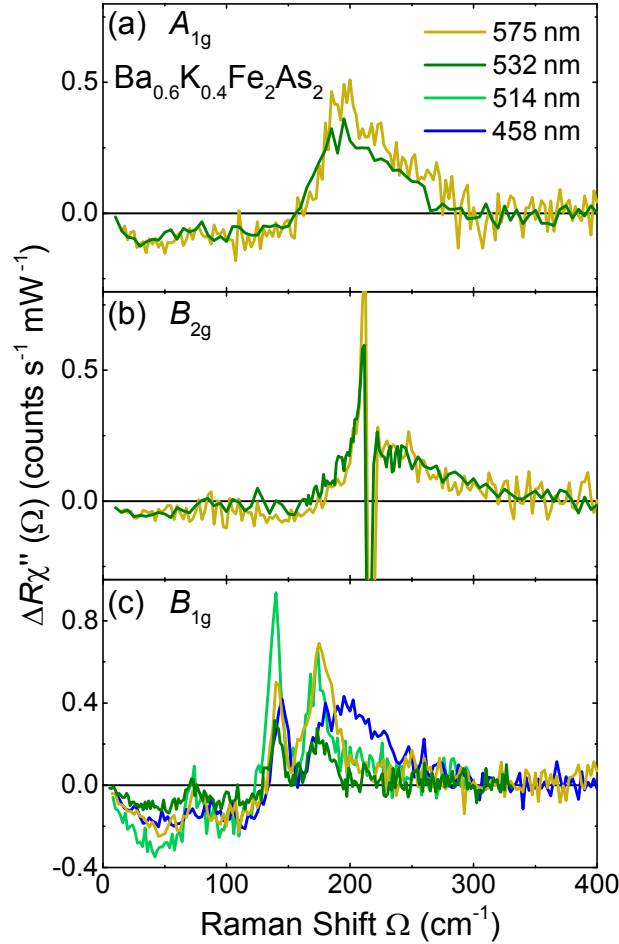


Figure 7.2: Difference spectra obtained with various excitation energies. Excitation wavelengths of 458 nm, 514 nm, 532 nm [47], and 575 nm were used. The colors approximately refer to those of the incident light.

performed.

Fig. 7.2 shows difference spectra in all symmetries for incident photons with a wavelength of 575 nm (yellow) and 532 nm (green) [47]. Spectra measured with 514 nm (green) and 458 nm (blue) were recorded just for B_{1g} symmetry. The A_{1g} and B_{2g} spectra are nearly identical, the B_{1g} spectra vary as a function of excitation wave-

length. Three peaks are visible in B_{1g} for all excitation energies. Whereas the intensities of the peaks change considerably the line shape and position remain similar for green and yellow photons. The largest change is observed for blue photons. Here the pair-breaking peak and the peak at 80 cm^{-1} are much broader.

This leads to the conclusion that resonances may play a role for blue photons but are insignificant for excitation energies lower than 2.4 eV (514 nm). Hence the effective mass approximation is valid for green and yellow photons. Excitation energies other than 514 nm and 575 nm were not used in this work.

7.3 Symmetry analysis in $\text{Ba}_{1-x}\text{K}_x\text{Fe}_2\text{As}_2$ ($0.35 \leq x \leq 0.70$)

Setting the polarizations of the incident (\mathbf{e}_i) and scattered (\mathbf{e}_s) light parallel to the ab plane always yields two of the even symmetries A_{1g} , A_{2g} , B_{1g} , and B_{2g} . Despite of the rapid aging of the sample surface in the case of $\text{Ba}_{1-x}\text{K}_x\text{Fe}_2\text{As}_2$, satisfactory statistics and a complete symmetry analysis could be achieved by measurements in the polarization configurations $(\mathbf{e}_i\mathbf{e}_s) \in \{xx, x'y', RL, RR\}$ [55].

The resulting spectra of the bare symmetries, as obtained from linear combinations of the measured spectra, are shown in Fig. 7.3. The response in A_{2g} symmetry in Fig. 7.3(c4-h4) is smaller than in the other symmetries, independent of temperature, and structureless. The temperature independence justifies the identification of the difference spectra $\Delta R\chi''(\Omega) = R\chi''(\Omega, T \ll T_c) - R\chi''(\Omega, T \gtrsim T_c)$, for which the pure symmetries were not derived, with the bare symmetries. No signatures of chiral excitations, as isolated by the A_{2g} symmetry, are observed in the examined energy range [55, 262].

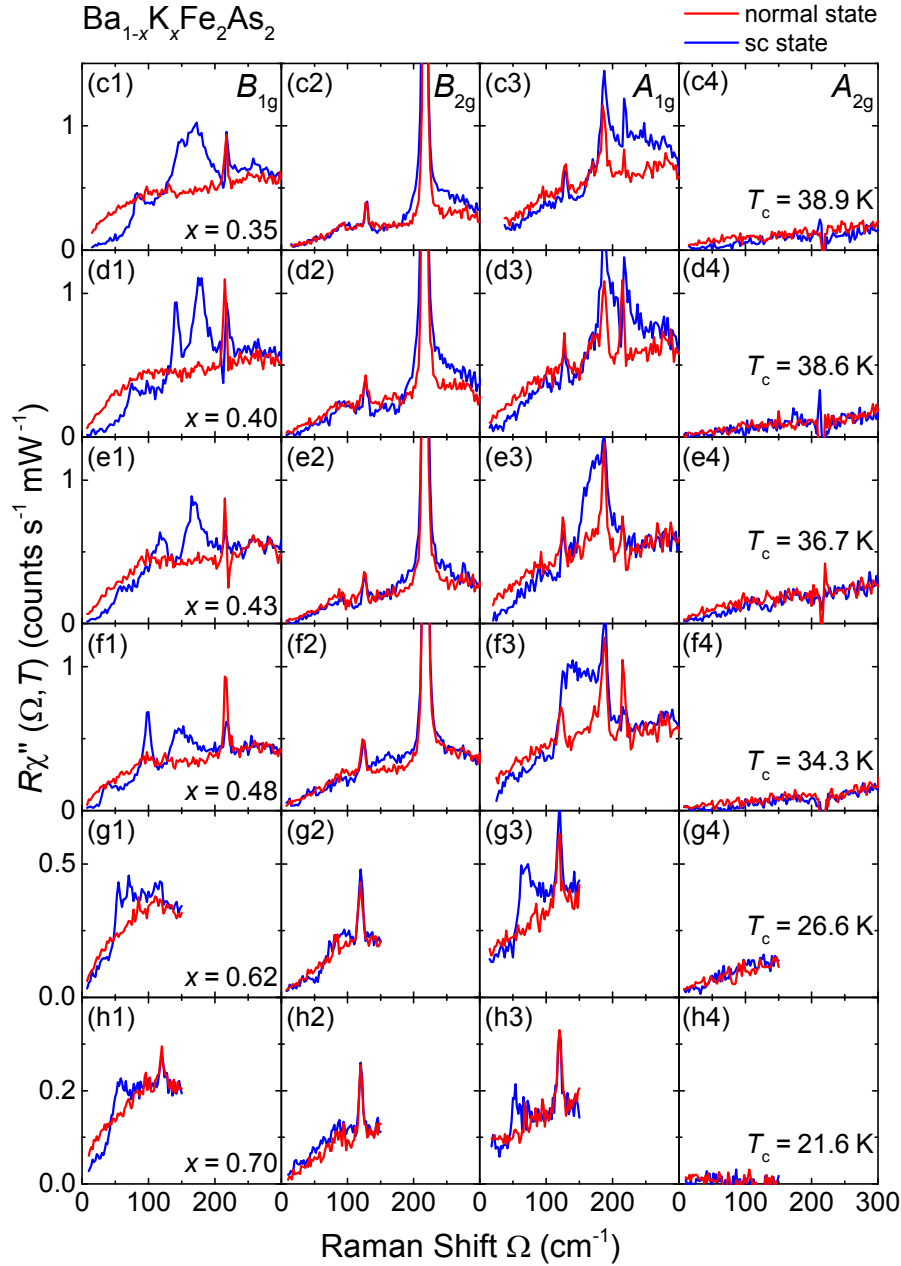


Figure 7.3: Symmetry analysis of the spectra obtained from $\text{Ba}_{1-x}\text{K}_x\text{Fe}_2\text{As}_2$. The bare symmetries B_{1g} (c1-h1), B_{2g} (c2-h2), A_{1g} (c3-h3), and A_{2g} (c4-h4) are shown in the doping range $0.35 \leq x \leq 0.70$. The applied subtraction procedure yielding these symmetries generates an artifact at 210 cm^{-1} , which results from the large intensity of the Fe B_{1g} phonon (appearing in B_{2g} symmetry as the 1 Fe unit cell is used here).

7.4 Relative strength of competing interactions

In $\text{Ba}_{1-x}\text{K}_x\text{Fe}_2\text{As}_2$ around optimal doping three peaks appear in the B_{1g} Raman spectra in the superconducting state, two BS modes and a pair-breaking peak. The following discussion will explain, how the ratios $\lambda_{d(i)}/\lambda_s$ for the corresponding subdominant channels ($i = 1, 2$) are determined.

It will be shown, that $\lambda_{d(i)}/\lambda_s$ is mainly determined by the pairing in the particle-particle (Cooper) channel. The changes induced by the inclusion of the particle-hole (zero-sound) interaction will also be studied as a function of the dominant pairing interaction λ_s . Furthermore, the validity of the approximation [47, 162]

$$\frac{E_B^{(i)}}{2\Delta} = 1 - \frac{\Omega_{\text{BS}(i)}}{2\Delta} \approx \left(\frac{\lambda_{d(i)}}{\lambda_s}\right)^2 \quad (7.1)$$

will be scrutinized.

In general, Eq. 5.10 determines the ratio $\lambda_{d(i)}/\lambda_s$ for a given λ_s . Hence for a vanishing zero-sound coupling $\lambda_z^{(i)} = 0$ and the simplification $\eta_{(i)} \equiv \langle g_{(i)}^2(\mathbf{k}) \rangle = 1$ the equation [46]

$$\frac{\Omega_{\text{BS}(i)}}{\sqrt{(2\Delta)^2 - \Omega_{\text{BS}(i)}^2}} \sin^{-1}\left(\frac{\Omega_{\text{BS}(i)}}{2\Delta}\right) = \frac{1}{\lambda_{d(i)}} - \frac{1}{\lambda_s} \quad (7.2)$$

holds.

This changes to [45]

$$\frac{\Omega_{\text{BS}(i)}}{\sqrt{(2\Delta)^2 - \Omega_{\text{BS}(i)}^2}} \sin^{-1}\left(\frac{\Omega_{\text{BS}(i)}}{2\Delta}\right) = \left[-\frac{\lambda_{d(i)}}{\Omega_{\text{BS}(i)}^2} (2\Delta)^2 + \frac{1}{\frac{1}{\lambda_{d(i)}} - \frac{1}{\lambda_s}} \right]^{-1} \quad (7.3)$$

if the zero-sound channel is included according to BCS approximation, $\lambda_z^{(i)} = -\lambda_{d(i)}$ [45].

The relation between $\Omega_{\text{BS}(i)}/2\Delta$ and $\lambda_{d(i)}/\lambda_s$ is shown in Fig. 7.4 for values of λ_s ranging from 0.14 to 1.0 using the three equations above. The range $0.14 \leq \lambda_s \leq 1$ is used since 0.14 is the result of the weak-coupling microscopic theories and 1 is expected from the T_c values [49, 51]. It is obvious, that only Eq. 7.1 is independent of λ_s . This approximation matches the result from Eq. 7.2 very well for small $\lambda_{d(i)}/\lambda_s$ and values of λ_s close to 1. For decreasing λ_s , the results increasingly deviate from one other.

Fig. 7.4 shows that Eq. 7.2 and 7.3 yield similar results for small λ_s and different yet comparable results for increasing λ_s . This justifies neglecting $\lambda_z^{(i)}$.

For the current analysis, $\lambda_s = 0.7$ is chosen to determine λ_d/λ_s from the experiment as shown in Fig. 7.4(b). Both fRG and RPA yield smaller values of λ_s close to 0.14, see Fig. 7.4(a). But even with $\lambda_s = 0.14$ the qualitative results obtained in Section 5.2 remain valid. The discrepancy comes from the tendency of fRG and RPA to underestimate the absolute coupling parameters $\lambda_{s/d(i)}$ and T_c .

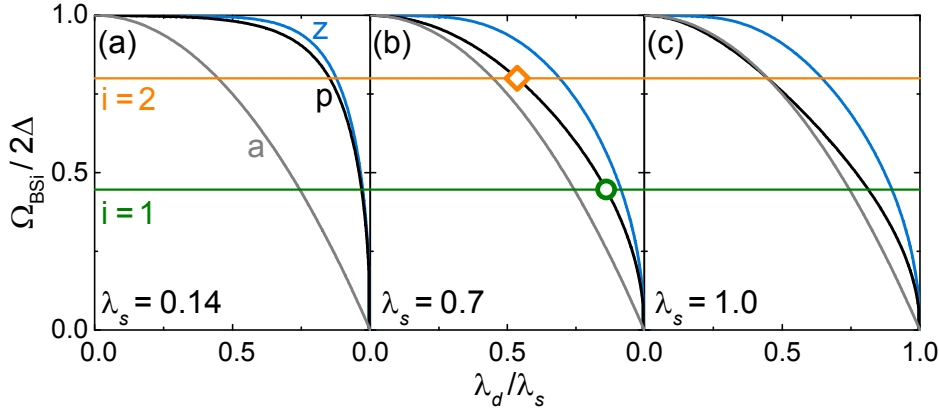


Figure 7.4: Determination of the relative pairing interaction $\lambda_{d(i)}/\lambda_s$. The BS modes at Ω_{BS1} and Ω_{BS2} are indicated by the green and orange lines, respectively. The pair-breaking peak defines 2Δ . This example is applied to the peak positions of $\text{Ba}_{0.6}\text{K}_{0.4}\text{Fe}_2\text{As}_2$ in B_{1g} symmetry. The relation between $\Omega_{BS(i)}/2\Delta$ and $\lambda_{d(i)}/\lambda_s$ is defined by Eq. 7.1, 7.2, and 7.3 yielding the approximation “a”, the result for a vanishing zero-sound coupling “p”, and “z” in the BCS case $\lambda_z^{(i)} = -\lambda_{d(i)}$. For the choice of $\lambda_s = 0.7$ with the relation “p”, the ratio $\lambda_{d(i)}/\lambda_s$ is defined by the open symbols in (b), corresponding to BS1 (green) and BS2 (orange).

7.5 Determination of T_{SDW} in $\text{Ba}(\text{Fe}_{0.949}\text{Co}_{0.051})_2\text{As}_2$

In $\text{Ba}(\text{Fe}_{0.949}\text{Co}_{0.051})_2\text{As}_2$, the structural transition temperature $T_s = 60.9\text{K}$ was determined by the appearance of stripes below T_s . The SDW transition temperature T_{SDW} can be extracted from the development of the Raman spectra in the temperature range $23\text{K} \leq T \leq 61.6\text{K}$. The Raman spectra of B_{1g} symmetry in this temperature range are presented in Fig. 7.5. It is observed that the intensity of the Raman spectra continuously decreases in the range up to about 250cm^{-1} upon lowering temperature. This is the case for all the spectra in the examined temperature range and makes it difficult to pin down T_{SDW} .

Therefore several experimental parameters were analyzed quantitatively. First the decrease of continuum intensity was quantified by an integral in the range from 15cm^{-1} to 130cm^{-1} . Instead of integrating up to 250cm^{-1} , a smaller energy range

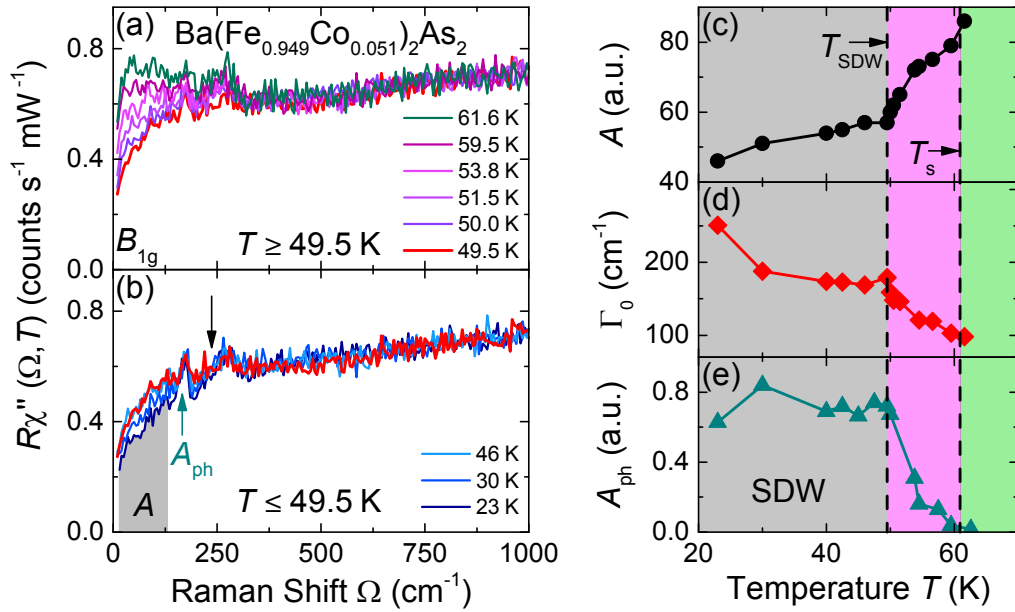


Figure 7.5: Determination of T_{SDW} . (a) and (b) show the Raman spectra in B_{1g} symmetry above and below 49.5 K, respectively. (c) compiles the development of the area $A(T)$ below the spectra as a function of temperature. As an example, $A(23 \text{ K})$ is illustrated in (b) by the grey area. (d) shows the static relaxation rate $\Gamma_0(T)$. (e) displays the spectral weight of the As phonon at 175 cm^{-1} as indicated by the dark cyan arrow in (b). The results are adopted from Ref. [134]. The transition temperature $T_{\text{SDW}} = 49.5 \text{ K}$ and $T_s = 60.9 \text{ K}$ are illustrated by dashed black lines, separating the SDW region (grey) from the nematic region (magenta) and the region with fluctuations (green) as in Fig. 2.1.

was chosen, as the intensity of the phonon appearing above 130 cm^{-1} exhibits an opposite temperature dependence. The integral yields a temperature dependent area $A(T)$ as shown in Fig. 7.5(c). The decrease of $A(T)$ with lowering temperature shows a clear kink at 49.5 K. The slope dA/dt above 49.5 K is larger than below. Without going into detail, the fast decrease above 49.5 K is associated with the reduction of fluctuations, whereas the slow decrease below 49.5 K is assigned to the opening of the SDW gap. When a gap Δ_{SDW} opens, the intensity below $2\Delta_{\text{SDW}}$ is suppressed, whereas the intensity above is enhanced, as a minimum energy of $2\Delta_{\text{SDW}}$ must be supplied to lift an electron above the gap. Such scattering processes are just possible for energies greater than $2\Delta_{\text{SDW}}$. In fact, a slight but visible increase of intensity in the energy range above the black arrow in Fig. 7.5(b) is observed. This happens for the spectra below 49.5 K with respect to the spectrum at 49.5 K. This is not the case above 49.5 K. Both observations hint towards $T_{\text{SDW}} = 49.5 \text{ K}$. This is supported by the anomaly in the static relaxation rate (see App. 7.6) as shown in Fig. 7.5(d). A discontinuity is observed close to 49.5 K.

Similarly as the continuum and the initial slope the change of the spectral weight (integrated intensity) of the As A_{1g} phonon develops discontinuously at T_{SDW} as shown in Fig. 7.5(e). The spectral weight itself has a kink at 49.5 K as described in detail in Ref. [134].

In summary, the SDW transition temperature at 49.5 K manifests itself in three independent anomalies. Whereas the first anomaly can be explained in terms of the SDW gap, the detailed description of the other two other is missing.

7.6 Relaxation rates

Relaxation rates $\Gamma(\Omega)$ are extracted from the Raman spectra and serve two purposes in the current analysis: (i) The temperature T_f , below which fluctuations emerge, is determined, and (ii) a comparison with the in-plane resistivity helps to disentangle the contribution from fluctuations and electron-hole excitations in the B_{1g} Raman spectra. In both cases only the static relaxation rate $\Gamma_0 \equiv \Gamma(\Omega \rightarrow 0)$ is of interest. The memory function approach yields [240, 241]

$$\Gamma(\Omega) = \frac{\bar{\chi}''(\Omega)}{[\bar{\chi}''(\Omega)]^2 + [\Omega K(\Omega)]^2} \quad (7.4)$$

with $\bar{\chi}''(\Omega) \equiv \chi''(\Omega)/\Omega$ and the Kramers-Krönig transform $K(\Omega)$ of $\bar{\chi}''(\Omega)$. The resulting frequency-dependent relaxation rate is fitted by the function

$$\Gamma(\Omega) \approx a \frac{b + c\Omega^2}{a + b + c\Omega^2} \quad (7.5)$$

with the fitting parameters a , b and c , yielding $\Gamma_0 = ab/(a+b)$. A detailed description and analysis is given in Refs. [73, 74, 124, 125, 134, 135, 240, 241].

The results are compiled in Fig. 7.6. In a Drude model, the resistivity in the ab -plane $\rho_{ab}(T)$ is related to $\Gamma_0(T)$ by [240]

$$\Gamma_0(T) = 1.08 \omega_{\text{pl}}^2 \rho_{ab}(T) \quad (7.6)$$

with the plasma frequency ω_{pl} in eV and ρ_{ab} in $\mu\Omega\text{cm}$. It is observed that $\Gamma_0(T)$ as extracted from the spectra in A_{1g} symmetry follows by and large the resistivity $\rho_{ab}(T)$. The same holds for B_{1g} symmetry above T_f . Below T_f the emergence of a new scattering channel causes $\Gamma_0(T)$ of B_{1g} to decrease faster than $\Gamma_0(T)$ of A_{1g} and $\rho_{ab}(T)$. This determines the onset of fluctuations.

To explain the resistivity above T_f the Raman vertices are scrutinized. The momentum-

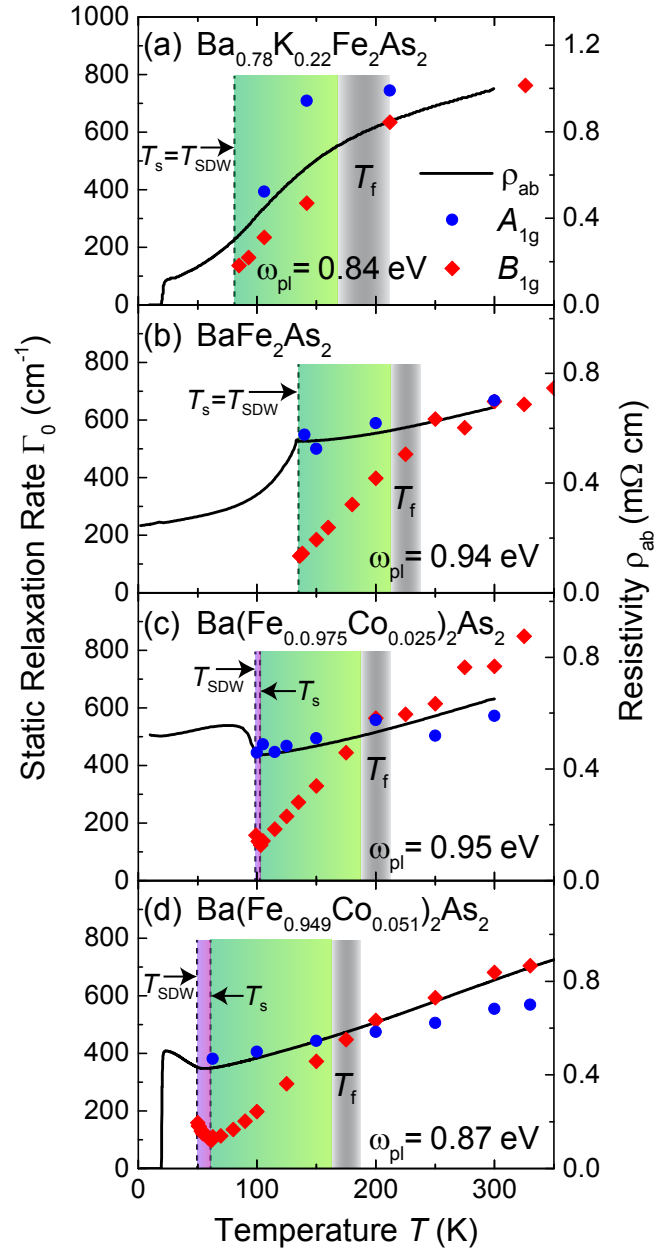


Figure 7.6: Static relaxation rates $\Gamma_0(T)$ for K-doped (a), undoped (b) and Co-doped (c,d) BaFe_2As_2 samples. $\Gamma_0(T)$, as extracted from the A_{1g} (blue dots) and B_{1g} (red diamonds) spectra is shown for temperatures above T_{SDW} . For high temperatures the static relaxation rates in A_{1g} and B_{1g} symmetry coincide with the in-plane resistivity ρ_{ab} (from Refs. [60, 263]) within the statistical errors. The onset of fluctuations is marked by a grey shaded area around T_f , indicating the split off of the static relaxation rate in B_{1g} symmetry. The temperature range where fluctuations are present is indicated in green. The temperature range of the nematic phase ($T_{SDW} < T < T_s$) is illustrated by the magenta shaded areas.

dependence of the Raman vertices in A_{1g} and B_{1g} symmetry (see Fig. 5.3) shows that only the electron pockets are highlighted in B_{1g} symmetry, whereas both hole and electron pockets contribute in A_{1g} symmetry. Hence the coincidence of $\Gamma_0(T)$ in A_{1g} and B_{1g} symmetry suggest that the resistivity is mainly related to the electron pockets. The influence from the hole pockets is small.

7.7 Analysis of the phonon anomaly

In addition to the electronic response the frequencies and line widths (FWHM) were derived from the spectra of $\text{Ba}_{1-x}\text{K}_x\text{Fe}_2\text{As}_2$. To extract these values, a Voigt fit was applied to the response in B_{1g} symmetry (here with respect to the crystallographic unit cell). Fig. 7.7 presents the spectra as data points in the range from 200 cm^{-1} to 235 cm^{-1} . In this range, the Voigt fit according to the function

$$V(\Omega) = (L * G)(\Omega) \quad (7.7)$$

with the Lorentzian function $L(\Omega)$ and the Gaussian function $G(\Omega)$ was applied to the phonon. The Voigt function is a convolution of a Gaussian for the resolution of the instrument and a Lorentzian for the phonon. Contributions from the electronic continuum were approximated by a linear function. According to the resolution of the spectrometer, the Gaussian width of the Voigt fit was set to 5 cm^{-1} . The agreement of the fit with the data shows, that the phonons are symmetrically centered around their peak frequencies. The simple superposition of phonon contribution and electronic continuum indicates a weak electron-phonon coupling. Otherwise an asymmetric shape described by a Fano function would be observable [264–266]. This phonon can hence be considered as a probe of certain effects as elucidated in Section 5.4.

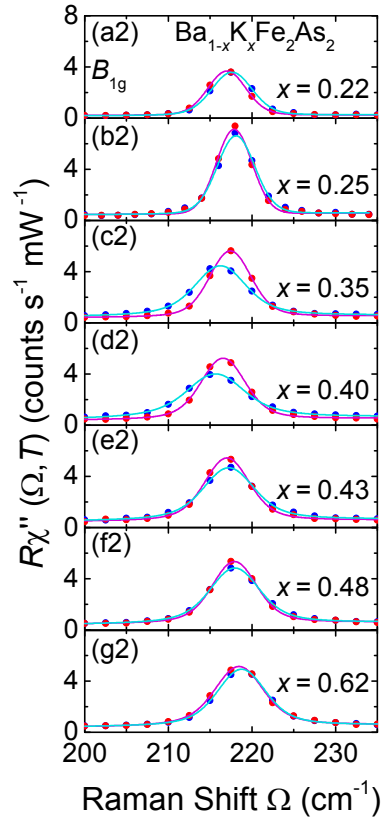


Figure 7.7: Voigt fits to the phonons in $\text{Ba}_{1-x}\text{K}_x\text{Fe}_2\text{As}_2$. Data points and fits are shown in the superconducting (blue) and normal (red) state.

Bibliography

- [1] R. P. Feynman, [Reviews of Modern Physics](#) **29**, 205 (1957).
- [2] H. Kamerlingh-Onnes, *Comm. Leiden* **120b** (1911).
- [3] W. Meissner and R. Ochsenfeld, [Naturwissenschaften](#) **21**, 787 (1933).
- [4] J. Bardeen, L. N. Cooper, and J. R. Schrieffer, [Physical Review](#) **108**, 1175 (1957).
- [5] M. A. Biondi, A. T. Forrester, M. P. Garfunkel, and C. B. Satterthwaite, [Reviews of Modern Physics](#) **30**, 1109 (1958).
- [6] C. P. Bean, [Reviews of Modern Physics](#) **36**, 31 (1964).
- [7] P. W. Anderson and Y. B. Kim, [Reviews of Modern Physics](#) **36**, 39 (1964).
- [8] B. S. Deaver and W. M. Fairbank, [Physical Review Letters](#) **7**, 43 (1961).
- [9] L. R. Testardi, [Reviews of Modern Physics](#) **47**, 637 (1975).
- [10] D. Jérôme, A. Mazaud, M. Ribault, and K. Bechgaard, [Journal de Physique Lettres](#) **41**, 95 (1980).
- [11] G. R. Stewart, [Reviews of Modern Physics](#) **56**, 755 (1984).
- [12] J. G. Bednorz and K. A. Müller, [Zeitschrift für Physik B Condensed Matter](#) **64**, 189 (1986).
- [13] O. Gunnarsson, [Reviews of Modern Physics](#) **69**, 575 (1997).
- [14] R. Joynt and L. Taillefer, [Reviews of Modern Physics](#) **74**, 235 (2002).
- [15] H. Hosono and K. Kuroki, [Physica C](#) **514**, 399 (2015).
- [16] L. N. Cooper, [Physical Review](#) **104**, 1189 (1956).

-
- [17] H. Frohlich, *Proceedings of the Royal Society of London A: Mathematical, Physical and Engineering Sciences* **215**, 291 (1952).
- [18] E. Maxwell, *Physical Review* **78**, 477 (1950).
- [19] C. A. Reynolds, B. Serin, W. H. Wright, and L. B. Nesbitt, *Physical Review* **78**, 487 (1950).
- [20] J. Eisenstein, *Reviews of Modern Physics* **26**, 277 (1954).
- [21] H. Kamerlingh-Onnes and W. Tuyn, *Comm. Leiden* **160b** (1922).
- [22] J. Nagamatsu, N. Nakagawa, T. Muranaka, Y. Zenitani, and J. Akimitsu, *Nature* **410**, 63 (2001).
- [23] A. P. Drozdov, M. I. Eremets, I. A. Troyan, V. Ksenofontov, and S. I. Shylin, *Nature* **525**, 73 (2015).
- [24] A. Schilling, M. Cantoni, J. D. Guo, and H. R. Ott, *Nature* **363**, 56 (1993).
- [25] D. Vaknin, S. K. Sinha, D. E. Moncton, D. C. Johnston, J. M. Newsam, C. R. Safinya, and H. E. King, *Physical Review Letters* **58**, 2802 (1987).
- [26] G. Shirane, Y. Endoh, R. J. Birgeneau, M. A. Kastner, Y. Hidaka, M. Oda, M. Suzuki, and T. Murakami, *Physical Review Letters* **59**, 1613 (1987).
- [27] R. J. Birgeneau, C. Y. Chen, D. R. Gabbe, H. P. Jenssen, M. A. Kastner, C. J. Peters, P. J. Picone, T. Thio, T. R. Thurston, H. L. Tuller, J. D. Axe, P. Böni, and G. Shirane, *Physical Review Letters* **59**, 1329 (1987).
- [28] A. Sokol and D. Pines, *Physical Review Letters* **71**, 2813 (1993).
- [29] C. C. Tsuei, J. R. Kirtley, C. C. Chi, L. S. Yu-Jahnes, A. Gupta, T. Shaw, J. Z. Sun, and M. B. Ketchen, *Physical Review Letters* **73**, 593 (1994).
- [30] C. C. Tsuei and J. R. Kirtley, *Reviews of Modern Physics* **72**, 969 (2000).
- [31] Y. Kamihara, H. Hiramatsu, M. Hirano, R. Kawamura, H. Yanagi, T. Kamiya, and H. Hosono, *Journal of the American Chemical Society* **128**, 10012 (2006).
- [32] Y. Kamihara, T. Watanabe, M. Hirano, and H. Hosono, *Journal of the American Chemical Society* **130**, 3296 (2008).

- [33] X. C. Wang, Q. Q. Liu, Y. X. Lv, W. B. Gao, L. X. Yang, R. C. Yu, F. Y. Li, and C. Q. Jin, [Solid State Communications](#) **148**, 538 (2008).
- [34] M. Rotter, M. Tegel, and D. Johrendt, [Physical Review Letters](#) **101**, 107006 (2008).
- [35] C. Ren, Z.-S. Wang, H.-Q. Luo, H. Yang, L. Shan, and H.-H. Wen, [Physical Review Letters](#) **101**, 257006 (2008).
- [36] Y. Mizuguchi, F. Tomioka, S. Tsuda, T. Yamaguchi, and Y. Takano, [Applied Physics Letters](#) **93**, 152505 (2008).
- [37] Q.-Y. Wang, Z. Li, W.-H. Zhang, Z.-C. Zhang, J.-S. Zhang, W. Li, H. Ding, Y.-B. Ou, D. Peng, K. Chang, J. Wen, C.-L. Song, K. He, J.-F. Jia, S.-H. Ji, Y.-Y. Wang, L.-L. Wang, X. Chen, X.-C. Ma, and Q.-K. Xue, [Chinese Physics Letters](#) **29**, 037402 (2012).
- [38] S. Tan, Y. Zhang, M. Xia, Z. Ye, F. Chen, X. Xie, R. Peng, D. Xu, Q. Fan, H. Xu, J. Jiang, T. Zhang, X. Lai, T. Xiang, J. Hu, B. Xie, and D. Feng, [Nature Materials](#) **12**, 634 (2013).
- [39] J.-F. Ge, Z.-L. Liu, C. Liu, C.-L. Gao, D. Qian, Q.-K. Xue, Y. Liu, and J.-F. Jia, [Nature Materials](#) **14**, 285 (2015).
- [40] J. J. Lee, F. T. Schmitt, R. G. Moore, S. Johnston, Y.-T. Cui, W. Li, M. Yi, Z. K. Liu, M. Hashimoto, Y. Zhang, D. H. Lu, T. P. Devereaux, D.-H. Lee, and Z.-X. Shen, [Nature](#) **515**, 245 (2014).
- [41] P. Monthoux, D. Pines, and G. G. Lonzarich, [Nature](#) **450**, 1177 (2007).
- [42] D. Einzel, “Private communication,” (2015).
- [43] A. Bardasis and J. R. Schrieffer, [Phys. Rev.](#) **121**, 1050 (1961).
- [44] A. Zawadowski, J. Ruvalds, and J. Solana, [Phys. Rev. A](#) **5**, 399 (1972).
- [45] H. Monien and A. Zawadowski, [Phys. Rev. B](#) **41**, 8798 (1990).
- [46] D. J. Scalapino and T. P. Devereaux, [Phys. Rev. B](#) **80**, 140512 (2009).
- [47] F. Kretschmar, B. Muschler, T. Böhm, A. Baum, R. Hackl, H.-H. Wen, V. Tsurkan, J. Deisenhofer, and A. Loidl, [Physical Review Letters](#) **110**, 187002 (2013).

-
- [48] S. Graser, A. F. Kemper, T. A. Maier, H.-P. Cheng, P. J. Hirschfeld, and D. J. Scalapino, [Phys. Rev. B **81**, 214503 \(2010\)](#).
- [49] K. Kuroki, H. Usui, S. Onari, R. Arita, and H. Aoki, [Physical Review B **79**, 224511 \(2009\)](#).
- [50] R. Thomale, C. Platt, W. Hanke, J. Hu, and B. A. Bernevig, [Physical Review Letters **107**, 117001 \(2011\)](#).
- [51] H. Ikeda, R. Arita, and J. Kuneš, [Physical Review B **81**, 054502 \(2010\)](#).
- [52] A. Damascelli, Z. Hussain, and Z.-X. Shen, [Reviews of Modern Physics **75**, 473 \(2003\)](#).
- [53] H. Ding, M. R. Norman, J. C. Campuzano, M. Randeria, A. F. Bellman, T. Yokoya, T. Takahashi, T. Mochiku, and K. Kadowaki, [Physical Review B **54**, R9678 \(1996\)](#).
- [54] D. N. Basov and T. Timusk, [Reviews of Modern Physics **77**, 721 \(2005\)](#).
- [55] T. P. Devereaux and R. Hackl, [Reviews of Modern Physics **79**, 175 \(2007\)](#).
- [56] D. N. Basov and A. V. Chubukov, [Nature Physics **7**, 272 \(2011\)](#).
- [57] T. Shibauchi, A. Carrington, and Y. Matsuda, [Annual Review of Condensed Matter Physics **5**, 113 \(2014\)](#).
- [58] I. I. Mazin, D. J. Singh, M. D. Johannes, and M. H. Du, [Physical Review Letters **101**, 057003 \(2008\)](#).
- [59] E. Fradkin, S. A. Kivelson, and J. M. Tranquada, [Reviews of Modern Physics **87**, 457 \(2015\)](#).
- [60] J.-H. Chu, J. G. Analytis, C. Kucharczyk, and I. R. Fisher, [Physical Review B **79**, 014506 \(2009\)](#).
- [61] G. S. Boebinger, Y. Ando, A. Passner, T. Kimura, M. Okuya, J. Shimoyama, K. Kishio, K. Tamasaku, N. Ichikawa, and S. Uchida, [Physical Review Letters **77**, 5417 \(1996\)](#).
- [62] W. Z. Hu, J. Dong, G. Li, Z. Li, P. Zheng, G. F. Chen, J. L. Luo, and N. L. Wang, [Physical Review Letters **101**, 257005 \(2008\)](#).

- [63] M. A. Ordal, R. J. Bell, R. W. Alexander, L. L. Long, and M. R. Querry, *Applied Optics* **24**, 4493 (1985).
- [64] I. R. Shein and A. L. Ivanovskii, *JETP Letters* **88**, 107 (2009).
- [65] A. E. Böhmer, P. Burger, F. Hardy, T. Wolf, P. Schweiss, R. Fromknecht, M. Reinecker, W. Schranz, and C. Meingast, *Physical Review Letters* **112**, 047001 (2014).
- [66] S. Avcı, O. Chmaissem, D. Y. Chung, S. Rosenkranz, E. A. Goremychkin, J. P. Castellan, I. S. Todorov, J. A. Schlueter, H. Claus, A. Daoud-Aladine, D. D. Khalyavin, M. G. Kanatzidis, and R. Osborn, *Physical Review B* **85**, 184507 (2012).
- [67] H. Wadati, I. Elfimov, and G. A. Sawatzky, *Physical Review Letters* **105**, 157004 (2010).
- [68] Q. Huang, Y. Qiu, W. Bao, M. A. Green, J. W. Lynn, Y. C. Gasparovic, T. Wu, G. Wu, and X. H. Chen, *Physical Review Letters* **101**, 257003 (2008).
- [69] M. Rotter, M. Tegel, D. Johrendt, I. Schellenberg, W. Hermes, and R. Pöttgen, *Physical Review B* **78**, 020503 (2008).
- [70] A. E. Böhmer, F. Hardy, L. Wang, T. Wolf, P. Schweiss, and C. Meingast, *Nature Communications* **6**, 7911 (2015).
- [71] L. Chauvière, Y. Gallais, M. Cazayous, M. A. Méasson, A. Sacuto, D. Colson, and A. Forget, *Physical Review B* **82**, 180521 (2010).
- [72] Y. Gallais and I. Paul, *Comptes Rendus Physique* **17**, 113 (2016).
- [73] F. Kretzschmar, T. Böhm, U. Karahasanović, B. Muschler, A. Baum, D. Jost, J. Schmalian, S. Caprara, M. Grilli, C. Di Castro, J. G. Analytis, J.-H. Chu, I. R. Fisher, and R. Hackl, *Nature Physics* **12**, 560 (2016).
- [74] T. Böhm, R. Hosseinian Ahanharnejhad, D. Jost, A. Baum, B. Muschler, F. Kretzschmar, P. Adelman, T. Wolf, H.-H. Wen, J.-H. Chu, I. R. Fisher, and R. Hackl, *physica status solidi (b)* **254**, 1600308 (2017).
- [75] K. Nakayama, T. Sato, P. Richard, Y.-M. Xu, Y. Sekiba, S. Souma, G. F. Chen, J. L. Luo, N. L. Wang, H. Ding, and T. Takahashi, *EPL (Europhysics Letters)* **85**, 67002 (2009).

- [76] D. V. Evtushinsky, D. S. Inosov, V. B. Zabolotnyy, A. Koitzsch, M. Knupfer, B. Büchner, M. S. Viazovska, G. L. Sun, V. Hinkov, A. V. Boris, C. T. Lin, B. Keimer, A. Varykhalov, A. A. Kordyuk, and S. V. Borisenko, [Physical Review B](#) **79**, 054517 (2009).
- [77] S. Graser, T. A. Maier, P. J. Hirschfeld, and D. J. Scalapino, [New Journal of Physics](#) **11**, 025016 (2009).
- [78] A. F. Kemper, T. A. Maier, S. Graser, H.-P. Cheng, P. J. Hirschfeld, and D. J. Scalapino, [New Journal of Physics](#) **12**, 073030 (2010).
- [79] T. Sato, K. Nakayama, Y. Sekiba, P. Richard, Y.-M. Xu, S. Souma, T. Takahashi, G. F. Chen, J. L. Luo, N. L. Wang, and H. Ding, [Physical Review Letters](#) **103**, 047002 (2009).
- [80] N. Xu, P. Richard, X. Shi, A. van Roekeghem, T. Qian, E. Razzoli, E. Rienks, G.-F. Chen, E. Ieki, K. Nakayama, T. Sato, T. Takahashi, M. Shi, and H. Ding, [Physical Review B](#) **88**, 220508 (2013).
- [81] H. Ding, K. Nakayama, P. Richard, S. Souma, T. Sato, T. Takahashi, M. Neupane, Y.-M. Xu, Z.-H. Pan, A. V. Fedorov, Z. Wang, X. Dai, Z. Fang, G. F. Chen, J. L. Luo, and N. L. Wang, [Journal of Physics: Condensed Matter](#) **23**, 135701 (2011).
- [82] M. Yi, D. Lu, J.-H. Chu, J. G. Analytis, A. P. Sorini, A. F. Kemper, B. Moritz, S.-K. Mo, R. G. Moore, M. Hashimoto, W.-S. Lee, Z. Hussain, T. P. Devereaux, I. R. Fisher, and Z.-X. Shen, [Proceedings of the National Academy of Sciences](#) **108**, 6878 (2011).
- [83] K. Terashima, Y. Sekiba, J. H. Bowen, K. Nakayama, T. Kawahara, T. Sato, P. Richard, Y.-M. Xu, L. J. Li, G. H. Cao, Z.-A. Xu, H. Ding, and T. Takahashi, [Proceedings of the National Academy of Sciences](#) **106**, 7330 (2009).
- [84] Y. Sekiba, T. Sato, K. Nakayama, K. Terashima, P. Richard, J. H. Bowen, H. Ding, Y.-M. Xu, L. J. Li, G. H. Cao, Z.-A. Xu, and T. Takahashi, [New Journal of Physics](#) **11**, 025020 (2009).
- [85] V. B. Zabolotnyy, D. S. Inosov, D. V. Evtushinsky, A. Koitzsch, A. A. Kordyuk, G. L. Sun, J. T. Park, D. Haug, V. Hinkov, A. V. Boris, C. T. Lin, M. Knupfer, A. N. Yaresko, B. Büchner, A. Varykhalov, R. Follath, and S. V. Borisenko, [Nature](#) **457**, 569 (2009).

-
- [86] Q. Si and E. Abrahams, *Physical Review Letters* **101**, 076401 (2008).
- [87] K. Seo, B. A. Bernevig, and J. Hu, *Physical Review Letters* **101**, 206404 (2008).
- [88] R. Yu and A. H. Nevidomskyy, *Journal of Physics: Condensed Matter* **28**, 495702 (2016).
- [89] P. Goswami, P. Nikolic, and Q. Si, *EPL (Europhysics Letters)* **91**, 37006 (2010).
- [90] N. E. Bickers, D. J. Scalapino, and S. R. White, *Physical Review Letters* **62**, 961 (1989).
- [91] N. Qureshi, P. Steffens, S. Wurmehl, S. Aswartham, B. Büchner, and M. Braden, *Physical Review B* **86**, 060410 (2012).
- [92] C. Platt, W. Hanke, and R. Thomale, *Advances in Physics* **62**, 453 (2013).
- [93] A. M. Oleś, *Physical Review B* **28**, 327 (1983).
- [94] T. Takimoto, T. Hotta, and K. Ueda, *Physical Review B* **69**, 104504 (2004).
- [95] K. Kubo, *Physical Review B* **75**, 224509 (2007).
- [96] J. Dong, H. J. Zhang, G. Xu, Z. Li, G. Li, W. Z. Hu, D. Wu, G. F. Chen, X. Dai, J. L. Luo, Z. Fang, and N. L. Wang, *EPL (Europhysics Letters)* **83**, 27006 (2008).
- [97] G. Wu, H. Chen, T. Wu, Y. L. Xie, Y. J. Yan, R. H. Liu, X. F. Wang, J. J. Ying, and X. H. Chen, *Journal of Physics: Condensed Matter* **20**, 422201 (2008).
- [98] M. Yi, D. H. Lu, J. G. Analytis, J.-H. Chu, S.-K. Mo, R.-H. He, R. G. Moore, X. J. Zhou, G. F. Chen, J. L. Luo, N. L. Wang, Z. Hussain, D. J. Singh, I. R. Fisher, and Z.-X. Shen, *Physical Review B* **80**, 024515 (2009).
- [99] R. M. Fernandes, A. V. Chubukov, J. Knolle, I. Eremin, and J. Schmalian, *Physical Review B* **85**, 024534 (2012).
- [100] R. M. Fernandes, A. V. Chubukov, and J. Schmalian, *Nature Physics* **10**, 97 (2014).

-
- [101] D. J. Singh, *Physica C: Superconductivity* **469**, 418 (2009).
- [102] R. A. Ewings, T. G. Perring, J. Gillett, S. D. Das, S. E. Sebastian, A. E. Taylor, T. Guidi, and A. T. Boothroyd, *Physical Review B* **83**, 214519 (2011).
- [103] D. K. Pratt, M. G. Kim, A. Kreyssig, Y. B. Lee, G. S. Tucker, A. Thaler, W. Tian, J. L. Zarestky, S. L. Bud'ko, P. C. Canfield, B. N. Harmon, A. I. Goldman, and R. J. McQueeney, *Physical Review Letters* **106**, 257001 (2011).
- [104] P. Dai, J. Hu, and E. Dagotto, *Nature Physics* **8**, 709 (2012).
- [105] K. Matan, R. Morinaga, K. Iida, and T. J. Sato, *Physical Review B* **79**, 054526 (2009).
- [106] M. Yi, Y. Zhang, Z.-K. Liu, X. Ding, J.-H. Chu, A. Kemper, N. Plonka, B. Moritz, M. Hashimoto, S.-K. Mo, Z. Hussain, T. Devereaux, I. Fisher, H. Wen, Z.-X. Shen, and D. Lu, *Nature Communications* **5**, 3711 (2014).
- [107] R. Kubo, *Reports on Progress in Physics* **29**, 255 (1966).
- [108] S. Caprara, C. Di Castro, M. Grilli, and D. Suppa, *Physical Review Letters* **95**, 117004 (2005).
- [109] P. J. Hirschfeld, M. M. Korshunov, and I. I. Mazin, *Reports on Progress in Physics* **74**, 124508 (2011).
- [110] M. Yashima, H. Nishimura, H. Mukuda, Y. Kitaoka, K. Miyazawa, P. M. Shirage, K. Kihou, H. Kito, H. Eisaki, and A. Iyo, *Journal of the Physical Society of Japan* **78**, 103702 (2009).
- [111] C. Platt, R. Thomale, C. Honerkamp, S.-C. Zhang, and W. Hanke, *Physical Review B* **85**, 180502 (2012).
- [112] S. Maiti and P. J. Hirschfeld, *Physical Review B* **92**, 094506 (2015).
- [113] L. Boeri, O. V. Dolgov, and A. A. Golubov, *Physical Review Letters* **101**, 026403 (2008).
- [114] L. Boeri, M. Calandra, I. I. Mazin, O. V. Dolgov, and F. Mauri, *Physical Review B* **82**, 020506 (2010).

- [115] Y. Nomura, K. Nakamura, and R. Arita, *Physical Review Letters* **112**, 027002 (2014).
- [116] S. Zhou, G. Kotliar, and Z. Wang, *Physical Review B* **84**, 140505 (2011).
- [117] H. Kontani and S. Onari, *Physical Review Letters* **104**, 157001 (2010).
- [118] T. Yamada, J. Ishizuka, and Y. Ōno, *Journal of the Physical Society of Japan* **83**, 043704 (2014).
- [119] H. Kontani, T. Saito, and S. Onari, *Physical Review B* **84**, 024528 (2011).
- [120] S. Onari and H. Kontani, *Physical Review Letters* **109**, 137001 (2012).
- [121] H. Kontani, Y. Inoue, T. Saito, Y. Yamakawa, and S. Onari, *Solid State Communications Special Issue on Iron-based Superconductors*, **152**, 718 (2012).
- [122] P. J. Hirschfeld, *Comptes Rendus Physique Iron-based superconductors*, **17**, 197 (2016).
- [123] M. V. Klein and S. B. Dierker, *Phys. Rev. B* **29**, 4976 (1984).
- [124] B. Muschler, *Carrier dynamics of Ba(Fe_{1-x}Co_x)₂As₂*, Ph.D. thesis, Technische Universität München (2012).
- [125] F. Kretzschmar, *Nematic Fluctuations, Fermiology and the Pairing Potential in Iron-Based Superconductors*, Ph.D. thesis, Technische Universität München (2015).
- [126] F. Hardy, P. Adelman, T. Wolf, H. v. Löhneysen, and C. Meingast, *Physical Review Letters* **102**, 187004 (2009).
- [127] F. Hardy, T. Wolf, R. A. Fisher, R. Eder, P. Schweiss, P. Adelman, H. v. Löhneysen, and C. Meingast, *Physical Review B* **81**, 060501 (2010).
- [128] H. K. Mak, P. Burger, L. Cevey, T. Wolf, C. Meingast, and R. Lortz, *Physical Review B* **87**, 214523 (2013).
- [129] J. Hou, P. Burger, H. K. Mak, F. Hardy, T. Wolf, C. Meingast, and R. Lortz, *Physical Review B* **92**, 064502 (2015).
- [130] H. Luo, Z. Wang, H. Yang, P. Cheng, X. Zhu, and H.-H. Wen, *Superconductor Science and Technology* **21**, 125014 (2008).

- [131] F. Venturini, *Raman Scattering Study of Electronic Correlations in Cuprates: Observation of an Unconventional Metal-Insulator Transition*, Dissertation, Technische Universität München (2003).
- [132] S. Shatz, A. Shaulov, and Y. Yeshurun, *Phys. Rev. B* **48**, 13871 (1993).
- [133] M. A. Tanatar, A. Kreyssig, S. Nandi, N. Ni, S. L. Bud'ko, P. C. Canfield, A. I. Goldman, and R. Prozorov, *Physical Review B* **79**, 180508 (2009).
- [134] D. Jost, *Spin Fluctuations and Superconductivity in Doped BaFe₂As₂*, Master thesis, Technische Universität München (2016).
- [135] R. Hossenian Ahangharnejhad, *Fluctuations and Superconductivity in Ba_{0.78}K_{0.22}Fe₂As₂*, Master thesis, Technische Universität München (2016).
- [136] A. Baum, *Untersuchung des Spindichtewellen-Übergangs in BaFe₂As₂*, Diplomarbeit, Technische Universität München (2012).
- [137] R. Hackl, *Inelastische Lichtstreuung an A15-Verbindungen*, Dissertation, Technische Universität München (1987).
- [138] A. A. Abrikosov and L. A. Fal'kovskii, *Zh. Eksp. Teor. Fiz.* **40**, 262 (1961).
- [139] W. Prestel, *Study of the Interaction Processes in Cuprate Superconductors by a Quantitative Comparison of Spectroscopic Experiments*, Dissertation, Technische Universität München (2012).
- [140] W. Spengler, R. Kaiser, and H. Bilz, *Solid State Communications* **17**, 19 (1975).
- [141] R. Sooryakumar and M. V. Klein, *Physical Review Letters* **45**, 660 (1980).
- [142] R. Hackl, R. Kaiser, and S. Schicktanz, *Journal of Physics C: Solid State Physics* **16**, 1729 (1983).
- [143] G. R. Boyd, T. P. Devereaux, P. J. Hirschfeld, V. Mishra, and D. J. Scalapino, *Physical Review B* **79**, 174521 (2009).
- [144] L. Aslamasov and A. Larkin, *Phys. Rev. A* **26**, 238 (1968).
- [145] U. Karahasanović, F. Kretzschmar, T. Böhm, R. Hackl, I. Paul, Y. Gallais, and J. Schmalian, *Physical Review B* **92**, 075134 (2015).

- [146] R. Kubo, *Journal of the Physical Society of Japan* **12**, 570 (1957).
- [147] T. P. Devereaux and D. Einzel, *Physical Review B* **51**, 16336 (1995).
- [148] T. P. Devereaux, *Physical Review B* **45**, 12965 (1992).
- [149] T. P. Devereaux, *Physical Review B* **47**, 5230 (1993).
- [150] R. Sooryakumar and M. V. Klein, *Physical Review B* **23**, 3213 (1981).
- [151] T. P. Devereaux and A. P. Kampf, *International Journal of Modern Physics B* **11**, 2093 (1997).
- [152] W. Hayes and R. Loudon, *Scattering of Light by Crystals* (Dover Publications, Mineola, N.Y., 2004).
- [153] B. S. Shastry and B. I. Shraiman, *Phys. Rev. Lett.* **65**, 1068 (1990).
- [154] P. B. Allen, *Phys. Rev. B* **13**, 1416 (1976).
- [155] M. Khodas, A. V. Chubukov, and G. Blumberg, *Physical Review B* **89**, 245134 (2014).
- [156] A. Hinojosa, J. Cai, and A. V. Chubukov, *Physical Review B* **93**, 075106 (2016).
- [157] S. Takada and E. Sakai, *Progress of Theoretical Physics* **59**, 1802 (1978).
- [158] M. Grilli, S. Caprara, C. Di Castro, T. Enss, R. Hackl, B. Muschler, and W. Prestel, *Physica B: Condensed Matter Proceedings of the International Conference on Strongly Correlated Electron Systems*, **404**, 3070 (2009).
- [159] G. D. Mahan, *Many Particle Physics*, 3rd ed. (Springer, New York, 2007).
- [160] T. P. Devereaux, A. Virosztek, and A. Zawadowski, *Physical Review B* **54**, 12523 (1996).
- [161] A. V. Chubukov, I. Eremin, and M. M. Korshunov, *Phys. Rev. B* **79**, 220501 (2009).
- [162] T. Böhm, A. F. Kemper, B. Moritz, F. Kretschmar, B. Muschler, H.-M. Eiter, R. Hackl, T. P. Devereaux, D. J. Scalapino, and H.-H. Wen, *Physical Review X* **4**, 041046 (2014).

-
- [163] V. K. Thorsmølle, M. Khodas, Z. P. Yin, C. Zhang, S. V. Carr, P. Dai, and G. Blumberg, [Physical Review B](#) **93**, 054515 (2016).
- [164] V. Brouet, M. F. Jensen, P.-H. Lin, A. Taleb-Ibrahimi, P. Le Fèvre, F. Bertran, C.-H. Lin, W. Ku, A. Forget, and D. Colson, [Physical Review B](#) **86**, 075123 (2012).
- [165] S. Maiti, T. A. Maier, T. Böhm, R. Hackl, and P. J. Hirschfeld, [Physical Review Letters](#) **117**, 257001 (2016).
- [166] A. P. Litvinchuk, V. G. Hadjiev, M. N. Iliev, B. Lv, A. M. Guloy, and C. W. Chu, [Physical Review B](#) **78**, 060503 (2008).
- [167] W. S. Corak, B. B. Goodman, C. B. Satterthwaite, and A. Wexler, [Physical Review](#) **102**, 656 (1956).
- [168] M. A. Biondi, M. P. Garfunkel, and A. O. McCoubrey, [Physical Review](#) **101**, 1427 (1956).
- [169] H. Ding, P. Richard, K. Nakayama, K. Sugawara, T. Arakane, Y. Sekiba, A. Takayama, S. Souma, T. Sato, T. Takahashi, Z. Wang, X. Dai, Z. Fang, G. F. Chen, J. L. Luo, and N. L. Wang, [EPL \(Europhysics Letters\)](#) **83**, 47001 (2008).
- [170] A. D. Christianson, E. A. Goremychkin, R. Osborn, S. Rosenkranz, M. D. Lumsden, C. D. Malliakas, I. S. Todorov, H. Claus, D. Y. Chung, M. G. Kanatzidis, R. I. Bewley, and T. Guidi, [Nature](#) **456**, 930 (2008).
- [171] M. Hiraishi, R. Kadono, S. Takeshita, M. Miyazaki, A. Koda, H. Okabe, and J. Akimitsu, [Journal of the Physical Society of Japan](#) **78**, 023710 (2009).
- [172] G. Li, W. Z. Hu, J. Dong, Z. Li, P. Zheng, G. F. Chen, J. L. Luo, and N. L. Wang, [Physical Review Letters](#) **101**, 107004 (2008).
- [173] L. Shan, Y.-L. Wang, J. Gong, B. Shen, Y. Huang, H. Yang, C. Ren, and H.-H. Wen, [Physical Review B](#) **83**, 060510 (2011).
- [174] G. Mu, H. Luo, Z. Wang, L. Shan, C. Ren, and H.-H. Wen, [Physical Review B](#) **79**, 174501 (2009).
- [175] R. Sooryakumar, M. V. Klein, and R. F. Frindt, [Physical Review B](#) **23**, 3222 (1981).

- [176] P. M. Platzman, [Physical Review](#) **139**, A379 (1965).
- [177] A. Zawadowski and M. Cardona, [Physical Review B](#) **42**, 10732 (1990).
- [178] G. A. Ummarino, M. Tortello, D. Daghero, and R. S. Gonnelli, [Physical Review B](#) **80**, 172503 (2009).
- [179] R. Hackl, P. Müller, D. Einzel, and W. Gläser, [Physica C: Superconductivity](#) **162**, 1241 (1989).
- [180] W. Prestel, F. Venturini, B. Muschler, I. Tütto, R. Hackl, M. Lambacher, A. Erb, S. Komiya, S. Ono, Y. Ando, D. Inosov, V. B. Zabolotnyy, and S. V. Borisenko, [The European Physical Journal Special Topics](#) **188**, 163 (2010).
- [181] D. Manske, *Theory of Unconventional Superconductors: Cooper-Pairing Mediated by Spin Excitations*, 1st ed. (Springer Berlin Heidelberg, 2010).
- [182] T. Tsuneto, [Physical Review](#) **118**, 1029 (1960).
- [183] D. Bohm and D. Pines, [Physical Review](#) **82**, 625 (1951).
- [184] D. Pines and D. Bohm, [Physical Review](#) **85**, 338 (1952).
- [185] D. Bohm and D. Pines, [Physical Review](#) **92**, 609 (1953).
- [186] Y. Zhang, L. X. Yang, F. Chen, B. Zhou, X. F. Wang, X. H. Chen, M. Arita, K. Shimada, H. Namatame, M. Taniguchi, J. P. Hu, B. P. Xie, and D. L. Feng, [Physical Review Letters](#) **105**, 117003 (2010).
- [187] A. J. Leggett, [Progress of Theoretical Physics](#) **36**, 901 (1966).
- [188] A. V. Chubukov, D. V. Efremov, and I. Eremin, [Physical Review B](#) **78**, 134512 (2008).
- [189] T. Cea and L. Benfatto, [Physical Review B](#) **94**, 064512 (2016).
- [190] G. Blumberg, A. Mialitsin, B. S. Dennis, M. V. Klein, N. D. Zhigadlo, and J. Karpinski, [Physical Review Letters](#) **99**, 227002 (2007).
- [191] M. Marciani, L. Fanfarillo, C. Castellani, and L. Benfatto, [Physical Review B](#) **88**, 214508 (2013).
- [192] S.-Z. Lin and X. Hu, [Physical Review Letters](#) **108**, 177005 (2012).

- [193] N. Bittner, *Response und kollektive Anregungen in Zweiband-Supraleitern*, Diplomarbeit, Technische Universität München (2012).
- [194] S. Maiti and A. V. Chubukov, [Physical Review B](#) **82**, 214515 (2010).
- [195] T. Yoshida, S.-i. Ideta, I. Nishi, A. Fujimori, M. Yi, R. Moore, S.-K. Mo, D. Lu, Z.-X. Shen, Z. Hussain, K. Kihou, C. H. Lee, A. Iyo, H. Eisaki, and H. Harima, [Condensed Matter Physics](#) **2**, 17 (2014).
- [196] M. Rehm, *Untersuchung der Dotierungsabhängigkeit der Wechselwirkungspotentiale von $\text{Ba}_{1-x}\text{K}_x\text{Fe}_2\text{As}_2$ / Analysis of the doping dependence of the interaction potentials of $\text{Ba}_{1-x}\text{K}_x\text{Fe}_2\text{As}_2$* , Master thesis, Technische Universität München (2015).
- [197] S.-F. Wu, P. Richard, H. Ding, H.-H. Wen, G. Tan, M. Wang, C. Zhang, P. Dai, and G. Blumberg, [arXiv:1608.06064 \[cond-mat\]](#) (2016), [arXiv:1608.06064 \[cond-mat\]](#) .
- [198] K. Nakayama, T. Sato, P. Richard, Y.-M. Xu, T. Kawahara, K. Umezawa, T. Qian, M. Neupane, G. F. Chen, H. Ding, and T. Takahashi, [Physical Review B](#) **83**, 020501 (2011).
- [199] D. V. Evtushinsky, D. S. Inosov, V. B. Zabolotnyy, M. S. Viazovska, R. Khasanov, A. Amato, H.-H. Klauss, H. Luetkens, Ch Niedermayer, G. L. Sun, V. Hinkov, C. T. Lin, A. Varykhalov, A. Koitzsch, M. Knupfer, B. Büchner, A. A. Kordyuk, and S. V. Borisenko, [New Journal of Physics](#) **11**, 055069 (2009).
- [200] Z. Lin, L. Hai-Yun, Z. Wen-Tao, M. Jian-Qiao, J. Xiao-Wen, L. Guo-Dong, D. Xiao-Li, Chen Gen-Fu, L. Jian-Lin, W. Nan-Lin, L. Wei, W. Gui-Ling, Z. Yong, Z. Yong, W. Xiao-Yang, Xu Zu-Yan, C. Chuang-Tian, and Z. Xing-Jiang, [Chinese Physics Letters](#) **25**, 4402 (2008).
- [201] L. Wray, D. Qian, D. Hsieh, Y. Xia, L. Li, J. G. Checkelsky, A. Pasupathy, K. K. Gomes, C. V. Parker, A. V. Fedorov, G. F. Chen, J. L. Luo, A. Yazdani, N. P. Ong, N. L. Wang, and M. Z. Hasan, [Physical Review B](#) **78**, 184508 (2008).
- [202] M. Rahlenbeck, G. L. Sun, D. L. Sun, C. T. Lin, B. Keimer, and C. Ulrich, [Physical Review B](#) **80**, 064509 (2009).

- [203] H. Chen, Y. Ren, Y. Qiu, W. Bao, R. H. Liu, G. Wu, T. Wu, Y. L. Xie, X. F. Wang, Q. Huang, and X. H. Chen, [EPL \(Europhysics Letters\) **85**, 17006 \(2009\)](#).
- [204] M.-H. Julien, H. Mayaffre, M. Horvatić, C. Berthier, X. D. Zhang, W. Wu, G. F. Chen, N. L. Wang, and J. L. Luo, [EPL \(Europhysics Letters\) **87**, 37001 \(2009\)](#).
- [205] D. Parker, M. G. Vavilov, A. V. Chubukov, and I. I. Mazin, [Physical Review B **80**, 100508 \(2009\)](#).
- [206] S. Maiti, R. M. Fernandes, and A. V. Chubukov, [Physical Review B **85**, 144527 \(2012\)](#).
- [207] J. G. Analytis, R. D. McDonald, J.-H. Chu, S. C. Riggs, A. F. Bangura, C. Kucharczyk, M. Johannes, and I. R. Fisher, [Physical Review B **80**, 064507 \(2009\)](#).
- [208] J.-P. Reid, M. A. Tanatar, X. G. Luo, H. Shakeripour, S. R. de Cotret, A. Juneau-Fecteau, J. Chang, B. Shen, H.-H. Wen, H. Kim, R. Prozorov, N. Doiron-Leyraud, and L. Taillefer, [Physical Review B **93**, 214519 \(2016\)](#).
- [209] E. Wiesenmayer, H. Luetkens, G. Pascua, R. Khasanov, A. Amato, H. Potts, B. Banusch, H.-H. Klauss, and D. Johrendt, [Physical Review Letters **107**, 237001 \(2011\)](#).
- [210] A. B. Vorontsov, M. G. Vavilov, and A. V. Chubukov, [Physical Review B **81**, 174538 \(2010\)](#).
- [211] C. Kant, J. Deisenhofer, A. Günther, F. Schrettle, A. Loidl, M. Rotter, and D. Johrendt, [Physical Review B **81**, 014529 \(2010\)](#).
- [212] F. Hardy, A. E. Böhmer, L. de' Medici, M. Capone, G. Giovannetti, R. Eder, L. Wang, M. He, T. Wolf, P. Schweiss, R. Heid, A. Herbig, P. Adelman, R. A. Fisher, and C. Meingast, [Physical Review B **94**, 205113 \(2016\)](#).
- [213] B. Mansart, D. Boschetto, A. Savoia, F. Rullier-Albenque, F. Bouquet, E. Papalazarou, A. Forget, D. Colson, A. Rousse, and M. Marsi, [Physical Review B **82**, 024513 \(2010\)](#).
- [214] K.-Y. Choi, P. Lemmens, I. Eremin, G. Zwicknagl, H. Berger, G. L. Sun, D. L. Sun, and C. T. Lin, [Journal of Physics: Condensed Matter **22**, 115802 \(2010\)](#).

- [215] P. M. Shirage, K. Kihou, K. Miyazawa, C.-H. Lee, H. Kito, H. Eisaki, T. Yanagisawa, Y. Tanaka, and A. Iyo, [Physical Review Letters](#) **103**, 257003 (2009).
- [216] Y.-M. Xu, Y.-B. Huang, X.-Y. Cui, E. Razzoli, M. Radovic, M. Shi, G.-F. Chen, P. Zheng, N.-L. Wang, C.-L. Zhang, P.-C. Dai, J.-P. Hu, Z. Wang, and H. Ding, [Nature Physics](#) **7**, 198 (2011).
- [217] R. Thomale, C. Platt, J. Hu, C. Honerkamp, and B. A. Bernevig, [Physical Review B](#) **80**, 180505 (2009).
- [218] R. Shankar, [Reviews of Modern Physics](#) **66**, 129 (1994).
- [219] E. Stueckelberg and A. Petermann, *Helvetica Physica Acta* **26**, 499 (1953).
- [220] T. Miyake, K. Nakamura, R. Arita, and M. Imada, [Journal of the Physical Society of Japan](#) **79**, 044705 (2010).
- [221] J. Wang, A. Eberlein, and W. Metzner, [Physical Review B](#) **89**, 121116 (2014).
- [222] T. A. Maier, “Private communication,” (2016).
- [223] P. D. Johnson, G. Xu, and W.-G. Yin, eds., *Iron-Based Superconductivity*, 2015th ed. (Springer, New York, NY, 2015).
- [224] W.-C. Lee, S.-C. Zhang, and C. Wu, [Physical Review Letters](#) **102**, 217002 (2009).
- [225] Y. Gallais, R. M. Fernandes, I. Paul, L. Chauvière, Y.-X. Yang, M.-A. Méasson, M. Cazayous, A. Sacuto, D. Colson, and A. Forget, [Physical Review Letters](#) **111**, 267001 (2013).
- [226] H. Yamase and R. Zeyher, [Physical Review B](#) **88**, 125120 (2013).
- [227] R. M. Fernandes and J. Schmalian, [Superconductor Science and Technology](#) **25**, 084005 (2012).
- [228] H. Yamase and R. Zeyher, [New Journal of Physics](#) **17**, 073030 (2015).
- [229] M. Khodas and A. Levchenko, [Physical Review B](#) **91**, 235119 (2015).
- [230] M. Neupane, P. Richard, Y.-M. Xu, K. Nakayama, T. Sato, T. Takahashi, A. V. Federov, G. Xu, X. Dai, Z. Fang, Z. Wang, G.-F. Chen, N.-L. Wang, H.-H. Wen, and H. Ding, [Physical Review B](#) **83**, 094522 (2011).

- [231] H.-H. Kuo, J.-H. Chu, J. C. Palmstrom, S. A. Kivelson, and I. R. Fisher, *Science* **352**, 958 (2016).
- [232] A. Charnukha, *Journal of Physics: Condensed Matter* **26**, 253203 (2014).
- [233] F. Ning, K. Ahilan, T. Imai, A. S. Sefat, R. Jin, M. A. McGuire, B. C. Sales, and D. Mandrus, *Journal of the Physical Society of Japan* **78**, 013711 (2009).
- [234] I. I. Mazin, *Nature* **464**, 183 (2010).
- [235] Y. Nakai, T. Iye, S. Kitagawa, K. Ishida, H. Ikeda, S. Kasahara, H. Shishido, T. Shibauchi, Y. Matsuda, and T. Terashima, *Physical Review Letters* **105**, 107003 (2010).
- [236] L. Tassini, W. Prestel, A. Erb, M. Lambacher, and R. Hackl, *Physical Review B* **78**, 020511 (2008).
- [237] L. Tassini, F. Venturini, Q.-M. Zhang, R. Hackl, N. Kikugawa, and T. Fujita, *Phys. Rev. Lett.* **95**, 117002 (2005).
- [238] L. Tassini, *Charge ordering phenomena and superconductivity in underdoped cuprates*, Ph.D. thesis, Technische Universität München (2008).
- [239] T. Böhm, *Raman-Streuung an unkonventionellen Supraleitern*, Diploma thesis, Technische Universität München (2012).
- [240] M. Opel, R. Nemetschek, C. Hoffmann, R. Philipp, P. F. Müller, R. Hackl, I. Tüttö, A. Erb, B. Revaz, E. Walker, H. Berger, and L. Forró, *Physical Review B* **61**, 9752 (2000).
- [241] W. Götze and P. Wölfle, *Physical Review B* **6**, 1226 (1972).
- [242] H. Yamase and R. Zeyher, *Physical Review B* **83**, 115116 (2011).
- [243] Y. Yanagi, Y. Yamakawa, N. Adachi, and Y. Ōno, *Physical Review B* **82**, 064518 (2010).
- [244] G. R. Boyd, P. J. Hirschfeld, and T. P. Devereaux, *Physical Review B* **82**, 134506 (2010).
- [245] V. Mishra, G. Boyd, S. Graser, T. Maier, P. J. Hirschfeld, and D. J. Scalapino, *Physical Review B* **79**, 094512 (2009).

- [246] B. Muschler, W. Prestel, R. Hackl, T. P. Devereaux, J. G. Analytis, J.-H. Chu, and I. R. Fisher, [Physical Review B](#) **80**, 180510 (2009).
- [247] C. Xu, M. Müller, and S. Sachdev, [Physical Review B](#) **78**, 020501 (2008).
- [248] D. J. Scalapino, [Reviews of Modern Physics](#) **84**, 1383 (2012).
- [249] S. Lederer, Y. Schattner, E. Berg, and S. A. Kivelson, [Physical Review Letters](#) **114**, 097001 (2015).
- [250] P. Lemmens, K. Y. Choi, G. Caimi, L. Degiorgi, N. N. Kovaleva, A. Seidel, and F. C. Chou, [Physical Review B](#) **70**, 134429 (2004).
- [251] Y. J. Um, A. Subedi, P. Toulemonde, A. Y. Ganin, L. Boeri, M. Rahlenbeck, Y. Liu, C. T. Lin, S. J. E. Carlsson, A. Sulpice, M. J. Rosseinsky, B. Keimer, and M. Le Tacon, [Physical Review B](#) **85**, 064519 (2012).
- [252] M. Rahlenbeck, *Raman light scattering study on phonon anomalies in unconventional superconductors*, Dissertation, Universität Tübingen (2010).
- [253] B. Xu, Y. M. Dai, B. Shen, H. Xiao, Z. R. Ye, A. Forget, D. Colson, D. L. Feng, H. H. Wen, C. C. Homes, X. G. Qiu, and R. P. S. M. Lobo, [Physical Review B](#) **91**, 104510 (2015).
- [254] S. Johnston, A. P. Sorini, B. Moritz, T. P. Devereaux, and D. J. Scalapino, [Physical Review B](#) **84**, 174523 (2011).
- [255] E. J. Nicol, C. Jiang, and J. P. Carbotte, [Physical Review B](#) **47**, 8131 (1993).
- [256] T. P. Devereaux, [Physical Review B](#) **50**, 10287 (1994).
- [257] P. Aynajian, T. Keller, L. Boeri, S. M. Shapiro, K. Habicht, and B. Keimer, [Science](#) **319**, 1509 (2008).
- [258] P. B. Allen and M. L. Cohen, [Physical Review Letters](#) **29**, 1593 (1972).
- [259] R. Zeyher and G. Zwicknagl, [Physica C: Superconductivity](#) **162**, 1709 (1989).
- [260] T. P. Devereaux, A. Virosztek, and A. Zawadowski, [Physical Review B](#) **51**, 505 (1995).
- [261] D. Johrendt and R. Pöttgen, [Physica C: Superconductivity](#) **469**, 332 (2009).

-
- [262] B. S. Shastry and B. I. Shraiman, [International Journal of Modern Physics B](#) **05**, 365 (1991).
- [263] B. Shen, H. Yang, Z.-S. Wang, F. Han, B. Zeng, L. Shan, C. Ren, and H.-H. Wen, [Physical Review B](#) **84**, 184512 (2011).
- [264] M. Opel, R. Hackl, T. P. Devereaux, A. Virosztek, A. Zawadowski, A. Erb, E. Walker, H. Berger, and L. Forró, [Physical Review B](#) **60**, 9836 (1999).
- [265] L. Chauvière, Y. Gallais, M. Cazayous, M. A. Méasson, A. Sacuto, D. Colson, and A. Forget, [Physical Review B](#) **84**, 104508 (2011).
- [266] U. Fano, [Physical Review](#) **124**, 1866 (1961).

List of Publications

1. F. Kretzschmar, B. Muschler, **T. Böhm**, A. Baum, R. Hackl, Hai-Hu Wen, V. Tsurkan, J. Deisenhofer, and A. Loidl.
Raman-Scattering Detection of Nearly Degenerate s -Wave and d -Wave Pairing Channels in Iron-Based $\text{Ba}_{0.6}\text{K}_{0.4}\text{Fe}_2\text{As}_2$ and $\text{Rb}_{0.8}\text{Fe}_{1.6}\text{Se}_2$ Superconductors.
Phys. Rev. Lett. **110**, 187002 (2013).
2. **T. Böhm**, A. F. Kemper, B. Moritz, F. Kretzschmar, B. Muschler, H.-M. Eiter, R. Hackl, T. P. Devereaux, D. J. Scalapino, and Hai-Hu Wen.
Balancing Act: Evidence for a Strong Subdominant d -Wave Pairing Channel in $\text{Ba}_{0.6}\text{K}_{0.4}\text{Fe}_2\text{As}_2$.
Phys. Rev. X **4**, 041046 (2014).
3. U. Karahasanović, F. Kretzschmar, **T. Böhm**, R. Hackl, I. Paul, Y. Gallais, and J. Schmalian.
Manifestation of nematic degrees of freedom in the Raman response function of iron pnictides.
Phys. Rev. B **92**, 075134 (2015).
4. F. Kretzschmar, **T. Böhm**, U. Karahasanović, B. Muschler, A. Baum, D. Jost, J. Schmalian, S. Caprara, M. Grilli, C. Di Castro, J. G. Analytis, J.-H. Chu, I. R. Fisher, and R. Hackl.
Critical spin fluctuations and the origin of nematic order in $\text{Ba}(\text{Fe}_{1-x}\text{Co}_x)_2\text{As}_2$.
Nat. Phys. **12**, 560-563 (2016).
5. S. Maiti, T. A. Maier, **T. Böhm**, R. Hackl, and P. J. Hirschfeld.
Probing the Pairing Interaction and Multiple Bardasis-Schrieffer Modes Using Raman Spectroscopy.
Phys. Rev. Lett. **117**, 257001 (2016).

6. **T. Böhm**, R. Hosseinian Ahanharnejhad, D. Jost, A. Baum, B. Muschler, F. Kretschmar, P. Adelman, T. Wolf, Hai-Hu Wen, I. R. Fisher, and R. Hackl. Superconductivity and fluctuations in $\text{Ba}_{1-p}\text{K}_p\text{Fe}_2\text{As}_2$ and $\text{Ba}(\text{Fe}_{1-n}\text{Co}_n)_2\text{As}_2$. *physica status solidi (b)* **254**, 1600308 (2017).

Acknowledgement

I want to thank all the people who contributed to this thesis and supported me during the last four years, especially

- Prof. Dr. Rudolf Gross for giving me the opportunity to work at the Walther Meissner Institute and for the productive atmosphere.
- Dr. Rudi Hackl for his imaginative ideas to solve physical problems, his tremendous amount of experience in the field of Raman spectroscopy and high-temperature superconductivity, for initiating fruitful international collaborations, his continuous support during writing this thesis and for providing the necessary freedom for my experimental studies.
- Prof. Dr. Dietrich Einzel for providing lots of exciting insights into the world of theory and his ability to explain complicated subjects
- Dr. Bernhard Muschler, Dr. Florian Kretzschmar, Dr. Hans-Martin Eiter, Andreas Baum, Nitin Chelwani, Michael Rehm, Daniel Jost, Ramez Hosseini Ahangharnejhad, Andreas Walter, David Hoch, Henrik Gabold, Reinhard Rossner, Ali Özkü, Maria Theodoridou, Georg Haunschild, and Roland Richter for making a perfect team, for various interesting discussions not only about physics, and for their immense support
- Prof. Dr. Thomas Devereaux, Dr. Brian Moritz, Dr. Lex Kemper, Dr. Yvonne Kung, Dr. Chunjing Jia, Dr. Beth Nowadnick and all members of Tom's group for their hospitality, the great atmosphere and for introducing me to theoretical physics. I especially want to thank Corinna Peng for helping me out of various bureaucratic issues
- Prof. Dr. Hai-Hu Wen, Prof. Dr. Ian Fisher, and Dr. Thomas Wolf for providing me with high-quality crystals

- Dr. Christian Platt and Dr. Thomas Maier for their continuous efforts on advancing the theory presented in this thesis
- Prof. Dr. Douglas Scalapino, Prof. Dr. Werner Hanke, Prof. Dr. Ronny Thomale, Prof. Dr. Peter Hirschfeld, Prof. Dr. Lara Benfatto, Prof. Dr. Marco Grilli, Prof. Dr. Jörg Schmalian, Dr. Una Karahasanović, and Dr. Saurabh Maiti for fruitful discussions and their enormous efforts for the theoretical support of this work
- Prof. Dr. Zoran Popović and Dr. Nenad Lazarević for their hospitality and for inspiring discussions
- Emel Dönertas and Ludwig Ossiander for helping me with any kind of organisational problems
- my fellow students and the scientists at the Walther Meissner Institute for the good atmosphere and for coming up with activities beyond physics.
- the technical staff of the Walther Meissner Institute who constantly made it possible to keep the experiments running
- my family for providing a place to recharge my batteries